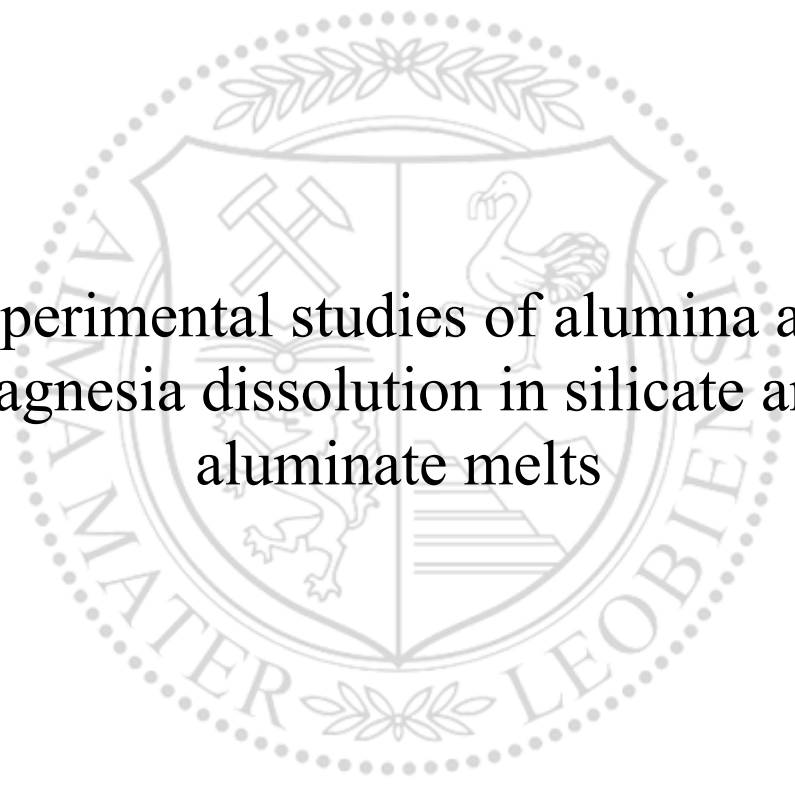




Chair of Ceramics

Doctoral Thesis



Experimental studies of alumina and  
magnesia dissolution in silicate and  
aluminate melts

Burhanuddin Burhanuddin

May 2022



**AFFIDAVIT**

I declare on oath that I wrote this thesis independently, did not use other than the specified sources and aids, and did not otherwise use any unauthorized aids.

I declare that I have read, understood, and complied with the guidelines of the senate of the Montanuniversität Leoben for "Good Scientific Practice".

Furthermore, I declare that the electronic and printed version of the submitted thesis are identical, both, formally and with regard to content.

Date 02.05.2022

*Burhanuddin*

---

Signature Author  
Burhanuddin Burhanuddin

## **ACKNOWLEDGEMENT**

The present work was produced through my research activities at the Chair of Ceramics, Montanuniversitaet Leoben. I would like to thank from my deep heart to the head of this chair and my supervisor, O.Univ.-Prof. Dipl.-Ing. Dr.mont. Harald Harmuth for the technical support and for the ongoing contribution of ideas, which were an indispensable contribution to the successful completion of this dissertation.

My very special thanks go to project leaders Dipl.-Ing. Dr.mont. Volkmar Kircher and Dipl.-Ing. Dr.mont. Sandra Vollmann for their technical support, arrangement of materials for the experiments and valuable discussion to extract required scientific information out of our experiments.

I would like to thank Mr. Christian Schober and Mr. Robert Caks for their support in laboratory during experiments. I would also like to thank Mr. Jerónimo Guarco for his simulation work on dissolution which gave us a chance to compare the simulation results with experimental results and to conclude in a better way.

I would also like to thank all my colleagues at the Chair of Ceramics and the Chair for Ferrous Metallurgy for the good cooperation and the friendly working atmosphere. Many thanks also to my mentor assoz.Prof. Dipl.-Ing. Dr.mont. Ernst Gamsjäger for the constructive technical discussions and support.

I gratefully acknowledge the financial support under the scope of the COMET program within the K2 Center “Integrated Computational Material, Process and Product Engineering (IC-MPPE)” (Project No 859480). This program is supported by the Austrian Federal Ministries for Transport, Innovation and Technology (BMVIT) and for Digital and Economic Affairs (BMDW), represented by the Austrian research funding association (FFG), and the federal states of Styria, Upper Austria, and Tyrol.

My final thanks go to all those who were there for me while this work was being carried out, especially my family for their support in all phases of this work and my friend, who had to forego a lot of time together over the past few months.

## LIST OF ABBREVIATIONS

HT-CLSM	High temperature confocal laser scanning microscope
CWTD	Continuous wear testing device
WDXRF	Wavelength dispersive X-ray fluorescence
CFD	Computational fluid dynamics
SCM	Shrinking core model
LBM	Lattice Boltzmann model
Wt%	Weight percentage
CAS	CaO-Al <sub>2</sub> O <sub>3</sub> -SiO <sub>2</sub>
CASM	CaO-Al <sub>2</sub> O <sub>3</sub> -SiO <sub>2</sub> -MgO
CASNB	CaO-Al <sub>2</sub> O <sub>3</sub> -SiO <sub>2</sub> -Na <sub>2</sub> O-B <sub>2</sub> O <sub>3</sub>
XRD	X-ray Diffraction
SEM-EDS	Scanning Electron Microscopy – Energy Dispersive X-ray Spectroscopy
Pt-Rh10	Platinum-10% Rhodium

---

## TABLE OF CONTENTS

1. Problem Definition .....	1
2. State of art.....	2
2.1. Fundamentals of refractory dissolution in melts .....	2
2.2. Experimental setups for dissolution studies .....	9
2.2.1. Static corrosion test.....	9
2.2.2. Dynamic corrosion test.....	11
2.3. Evaluation techniques for dissolution index .....	13
2.3.1. Dissolution rate in terms of change in dimension.....	13
2.3.2. Relative remaining volume .....	14
2.3.3. Reaction area.....	14
2.3.4. Change of dissolving refractory species concentration in the slag .....	14
3. Experiment.....	16
3.1. Experimental setup.....	16
3.1.1. High temperature confocal laser scanning microscope (HT-CLSM).....	16
3.1.2. Continuous wear testing device (CWTD).....	24
3.2. Experimental procedure .....	30
3.2.1. Experimental procedure of HT-CLSM measurements .....	30
3.2.2. Experimental procedure of CWTD.....	32
3.3. Evaluation methods.....	34
3.3.1. Evaluation methods for HT-CLSM experiments.....	34
3.3.2. Evaluation methods for CWTD experiments.....	37
4. Materials .....	49
4.1. Slags.....	49
4.2. Refractory materials .....	52
5. Results and discussion.....	53
5.1. HT-CLSM studies for alumina dissolution.....	53
5.1.1. Dissolution curves .....	53
5.1.2. Dissolution rate .....	54
5.1.3. Diffusivity.....	55
5.2. HT-CLSM studies for magnesia dissolution .....	60
5.2.1. Dissolution curves .....	60
5.2.2. Dissolution rate .....	61
5.2.3. Diffusivity.....	62
5.3. Dissolution studies of alumina fine ceramics in CWTD .....	64
5.3.1. CW curves for alumina dissolution .....	65
5.3.2. Dissolution parameters.....	70

5.3.3. Diffusivity.....	75
5.4. Dissolution studies of magnesia fine ceramics in CWTD.....	79
5.4.1. CW curves for magnesia dissolution.....	80
5.4.2. Dissolution parameters.....	83
5.4.3. Diffusivity.....	85
5.5. Comparison of diffusivities.....	88
6. Conclusion.....	89
7. References.....	R 1

## ABSTRACT

Dissolution experiments of alumina and magnesia in silicate and aluminate melts were conducted at 1450, 1500 and 1550 °C in high temperature confocal laser scanning microscope (HT-CLSM) and continuous wear testing device (CWTD) to determine diffusivities. CLSM studies were performed with spherical sapphire and fused magnesia particles in three silicate and one calcium aluminate slags, whereas finger test of alumina and magnesia fine ceramics in CWTD were carried out in two silicate slags. Effect of rotational speed was also examined for alumina dissolution at 1550 °C in both slags. Laser measurement of CWTD includes the wear profile of whole sample surface with high resolution, as a result, the dissolution parameters calculated from these, are expected to be more accurate than the manual measurements of the post-mortem analysis. Three models were applied to determine diffusivity from CLSM studies. Shrinking core models with (M2) and without (M1) convective part of mass flux suffer from the fact they cannot represent the dissolution curve shape well, as their assumption regarding the effective diffusive boundary layer thickness proves to be not accurate enough. Whereas the third model (M3) is more scientifically sound for quasi-steady state dissolution which incorporate the Stefan condition correctly, moving boundary condition and effect of bath movement. Dissolution time of the particle in CLSM increases with decreasing temperature, due to lower diffusivity. For the dynamic experiments of alumina fine ceramics with 200 rpm, Reynolds numbers were sufficiently high to suppress the Marangoni convection; however, this was not the case for magnesia dissolution. In these experiments, diffusivity was determined using Sherwood relations and simulation from dynamic corrosion experiments and the diffusivities show good agreement. Furthermore, these results are very similar to diffusivities of M3 from CLSM studies.

## 1. Problem Definition

Refractory wear may largely impact process feasibility due to extreme processing conditions and elevated temperatures. Two important mechanisms of continuous wear are dissolution in slags and melts (also known as corrosion) and erosion by the action of shear stresses caused by fluid flow on the slag/refractory interface. In this thesis, focus will be on the corrosion. The dissolution kinetics of refractory components and quantification of the mechanisms of wear in the corresponding slags is of essential importance for the refractory industry as well as for the ferrous and non-ferrous industries. Necessary low dissolution rates trigger the development of more wear resistant materials and have a positive effect on the service life of refractory products. On the other hand, in the field of metallurgy, non-metallic inclusions are absorbed by the slag, in which case rapid dissolution of the particles is important to ensure high product quality. One task of this thesis is the investigation of the dissolution kinetics, including the determination of effective binary diffusion coefficients of ideal spherical alumina particles and real fused magnesia particles in synthetic slags using high temperature confocal laser scanning microscope (HT-CLSM). There are several publications on the dissolution study of refractory particles in slags using HT-CLSM, but scientifically sound models for diffusivity determination out of HT-CLSM experiments are still missing. The aim of this work is to apply critical and scientific interpretation of dissolution process and methods for the determination of diffusivity.

In case of HT-CLSM experiments a relative motion between dissolving particle and slag may occur, but the fluid flow is not well defined. Normally, characteristics of the fluid flow like e.g., Reynolds number are required to determine effective boundary layer thickness and accurately quantify dissolution. To fulfil this requirement, dynamic finger test of alumina and magnesia fine ceramics were carried out in a molten slag bath using a so-called continuous wear testing device (CWTD). A laser scanner attached to CWTD measures surface profiles before and after corrosion steps. Dissolution parameters were extracted from the laser measurements.

Slag and material properties are required for the quantification of dissolution mechanisms. Slags were prepared using high purity limestone, magnesia powder, calcined alumina, and quartz powder. Chemical analysis of each raw materials was carried out using X-Ray fluorescence spectroscopy (XRF). Saturation limits of dissolving species in the slags at experimental temperatures and viscosities were calculated using FactSage 7.2.



## 2. State of art

### 2.1. Fundamentals of refractory dissolution in melts

Refractory corrosion due to thermo-chemical attack generally is caused by disequilibrium with other chemical species in contact with the material. In this thesis work corrosion is defined in a narrower sense as dissolution of a refractory component in a molten phase. **Figure 1** shows a graphical representation of the main processes of refractory corrosion by dissolution [1]. Usually, refractory wear by erosion also concurs with refractory corrosion as dissolution of the refractory matrix weakens the bond and promotes following erosion. Corrosion of refractories is considered to be a diffusion-controlled mechanism and the pure diffusive mass flux ( $j$ ) is governed by Fick's 1<sup>st</sup> law [1].

$$j = D \cdot \frac{(c_1^l - c_0^l)}{\delta} = D \cdot \frac{(c_s^l - c_0^l)}{\delta} \quad (1)$$

Here,  $D$  is effective diffusion coefficient of dissolving species,  $c_1^l$  and  $c_0^l$  are the concentration of the dissolving species at the refractory-slag interface and bulk slag respectively,  $c_s^l$  is the solubility limit of the component in the slag and  $\delta$  is the boundary layer thickness.

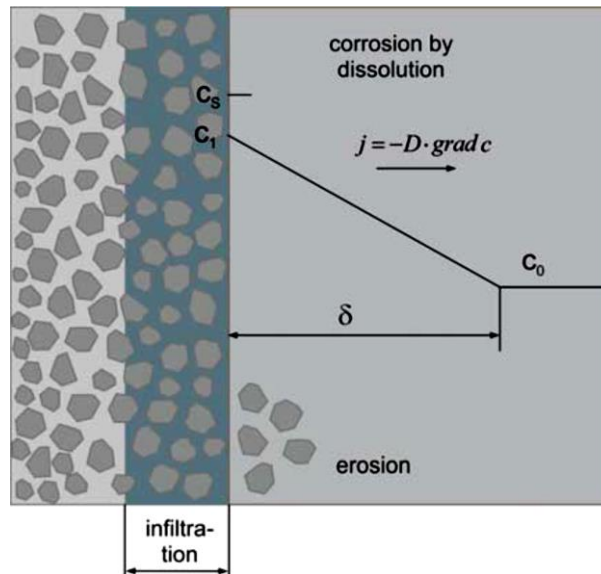


**Figure 1: Schematic representation of the main processes of refractory corrosion [1].**

Justification of the substitution of  $c_1^l$  by  $c_s^l$  will be discussed later. Further this equation is simplified by introducing mass transfer coefficient  $\beta$  which equals the ratio  $D/\delta$  [1].

$$j = \beta \cdot (c_s^l - c_0^l) \quad (2)$$

Fluid flow is a major factor which influences mass transfer coefficient by altering effective boundary layer thickness,  $\delta$ . Impact of fluid flow on mass transfer was originally quantified analytically especially with the help of boundary layer theory. Additionally, nowadays it can be determined by computational fluid dynamics (CFD) for by far more complex arrangements.

The Sherwood number ( $Sh$ ), the Reynolds number ( $Re$ ), and the Schmidt number ( $Sc$ ) are the dimensionless quantities which are applied to relate the mass transfer coefficient to other independent variables [1].

$$Sh = \frac{\beta \cdot L}{D} \quad (3)$$

$$Re = \frac{u \cdot L}{\nu} \quad (4)$$

$$Sc = \frac{\nu}{D} \quad (5)$$

Here  $L$  and  $u$  are spatial dimension and a velocity chosen as significant quantities for the case study, respectively, and  $\nu$  is the kinematic viscosity. As per the actual case, further simplexes or complexes  $\Gamma_i$  involving geometrical parameters may contribute. These dimensionless numbers can be correlated and represented by a power law [1], [2]:

$$Sh = const. \cdot Re^a \cdot Sc^b \cdot \prod_i \Gamma_i^{c_i} \quad (6)$$

The constant coefficient and the exponents of equation (6) can be determined by fitting the results of several simulations. Explicitly expressing  $\beta$  from equation (6), substituting into equation (2) and rearranging as equation (1), the diffusive flux can be represented as:

$$j = \frac{D}{\delta} \cdot D^{-b} \cdot const. \cdot \underbrace{\nu^{b-a} \cdot u^a \cdot L^{a-1} \cdot \prod_i \Gamma_i^{c_i}}_{1/\delta} \cdot \underbrace{(c_s^l - c_0^l)}_{\Delta c} \quad (7)$$

This equation shows the dependency of corrosive mass flux on various parameters. The combination of refractory and slag will majorly influence the concentration difference and further effective diffusion coefficient. Fluid dynamics and geometrical conditions influence the corrosion process through influencing  $1/\delta$  or  $\delta$ .

The following comments focus on the relation between  $c_1^l$  and  $c_s^l$  and follow the representation in [3]. The mass flux balance of the dissolving flux of a solid species with the diffusive flux at the interface is shown in Equation (8):

$$\underbrace{c_s^s \cdot \frac{D \cdot \zeta}{a} \cdot e^{\frac{\Delta\mu_c}{RT}} \cdot \frac{a_s - a_1}{a_s}}_{\text{Dissolution kinetics}} = \underbrace{\frac{D}{\delta} \cdot \frac{c_s^s}{c_s^s - V_v \cdot c_1^l} \cdot (c_1^l - c_0^l)}_{\text{Diffusion}} \quad (8)$$

Here,  $D$  is effective binary diffusion coefficient,  $\zeta$  is the frequency factor,  $a$  is a distance characterizing the dissolving species (~ ion diameter),  $a_s$  is the activity of the dissolving species in saturated slag,  $a_1$  is activity of species in the slag at the interface,  $\Delta\mu_c$  is difference of Gibbs

energy of dissolving species in the solid minus the pure liquid state,  $c^s$  is concentration of dissolving species in the solid (refractory),  $c_1^l$  is the concentration at the solid-slag interface,  $c_s^l$  is concentration of slag saturated by species,  $c_0^l$  is the bulk concentration of species in the slag unaffected by the dissolution,  $\delta$  is the boundary layer thickness and  $V_v$  is the partial volumetric volume [1].

Equation (9) can be obtained from equation (8) after cancelling the equal quantities and rearranging [3]. Due to the fact that “ $a$ ” is in the size range of an ion diameter and therefore much smaller than the effective boundary layer thickness ( $a/\delta \approx 10^{-7}$ ),  $a_s - a_1$  is very small and it can be concluded that  $a_1 = a_s$  and  $c_1^l = c_s^l$ . Furthermore, we can say that the diffusion is the rate determining step of the dissolution process, mainly because of the relatively larger boundary layer thickness ( $\delta \gg a$ ). It means, dissolution is a diffusion-controlled process.

$$\frac{a_s - a_1}{a_s} = \frac{a}{\delta} \cdot \frac{1}{\zeta} \cdot e^{-\frac{\Delta\mu_c}{RT}} \frac{c_1^l - c_0^l}{c^s - V_v \cdot c_1^l} \quad (9)$$

While representation of  $c_1^l$  by  $c_s^l$  is believed to be accurate enough in all cases considered in this thesis work, deviations from this are not impossible. It might be a point of discussion whether diffusivity relay is the same on both sides of equation (8), or whether it is lower on the left side. The latter case would tend to increase the difference between  $c_1^l$  and  $c_s^l$ . To quantify the dissolution, two types of experimental setups are widely used. First one, high temperature confocal laser scanning microscope (HT-CLSM) is used for particle dissolution in melts. There may be relative motion between refractory particle and slag due to a temperature gradient inside the crucible, but this is uncontrolled and immeasurable. Second one is the rotating finger test or disc test. In this case, boundary layer thickness can be defined clearly with known fluid flow or Reynolds number.

In general, dissolution is controlled by the diffusion in the liquid phase, the diffusivity is therefore the most important parameter to quantify dissolution. Here the approach of effective binary diffusivity will be used. In various references some approaches are reported to determine diffusivity. First those related to CLSM studies will be discussed. In [4] which was prepared in course of this thesis work deficiencies of various approaches reported in the literature, possible remedies and the verification of results with a reference method are exemplified.

For the exact evaluation of the general case of particle dissolution, a relatively complex problem would need to be represented for determination of diffusivity by inverse simulation. This includes the diffusion-convection equation together with the fluid dynamical problem according to Navier-Stokes equations. Further, the moving boundary would have to be considered by the so-called Stefan condition. Also, without any additional source of fluid motion, viz. in the case of pure molecular diffusion, solution of the diffusion equation alone would not exactly suffice, as a convective part of the mass flux originates from the fact that the solid/liquid interface is impermeable for the not dissolving species. This case, the diffusion-convection equation with moving boundary in infinite space and spherical symmetry, was

investigated by Readey and Cooper [5]. Solution of the general problem including additional fluid flow and arbitrary geometry is so far normally not applied for evaluation purposes. Probably one reason is the fact that the geometrical conditions (e.g., the position of the particle relative to the crucible and the free surface) are not registered in dependence of time. A more satisfying reason is that simple approximations may be suitable in several cases.

Most of the researchers have used the simplest classical shrinking core model (SCM) to confirm the dissolution mechanism and to determine diffusivity for spherical particle dissolution in CLSM experiments [6]–[12]. This model is based on diffusion through a boundary layer. Equation (10) represents the ordinary differential equation for diffusion according to SCM. The boundary layer thickness is assumed equal to the particle radius in this model. The accuracy of this approach is questionable, especially for cases where fluid motion is observed. This model follows a steady state diffusion problem, viz. neither time dependence nor the impact of the convection is represented exactly, and the Stefan condition is not considered. Deficiencies of SCM and counter measures will be discussed later.

$$\frac{dR}{dt} = -\frac{D \cdot (c_s^l - c_0^l)}{R \cdot \rho^p} \quad (10)$$

Here,  $R$  is particle radius,  $t$  time and  $\rho^p$  is the particle density.

Some researchers observed that in many cases classical SCM is not sufficient to describe the dissolution behavior. They used one dimensional diffusion equation (11) to obtain concentration profiles for the diffusion-controlled dissolution of spherical particle into a stagnant melt.

$$\frac{\partial c}{\partial t} = D \cdot \frac{1}{r^2} \cdot \frac{\partial}{\partial r} \left( r^2 \cdot \frac{\partial c}{\partial r} \right) \quad (11)$$

Here,  $r$  is the radial coordinate and  $c$  is the concentration of the dissolving species.

Liu, Verhaeghe and their research group used a lattice Boltzmann model (LBM) to solve this diffusion equation [13]–[16]. Yi et al. [17] introduced three dissolution parameters  $Du1 = R/\tau$ ,  $Du2 = R^{1.5}/\tau$  and  $Du3 = R^2/\tau$ . Here,  $R$  is the observed radius ( $\mu\text{m}$ ) of the inclusions (which changes with time,  $t$ ) and  $\tau$  is the time for complete dissolution of a particle of radius  $R$ . Each parameter will have a constant or nearly constant value when a particular mechanism dominates.  $Du1$  and  $Du3$  are constant when a surface reaction or boundary layer diffusion are the respective controlling mechanisms [17].

Whelan reported equation (12) for the diffusion controlled dissolution of a spherical particle based on the complementary error function [18]; originally this equation was applied for solid state. The term  $R^{-1}$  on the right of the equation (12) arises from the steady-state part of the diffusion field and the term in  $t^{-1/2}$  arises from the transient part. Here, it was tried to address the deviation from the steady state, however, it doesn't fully consider Stefan flow [18].

$$\frac{dR}{dt} = -\frac{c_s^l - c_0^l}{c^s - c_s^l} \cdot \frac{D}{R} - \frac{c_s^l - c_0^l}{c^s - c_s^l} \cdot \sqrt{\frac{D}{\pi \cdot t}} \quad (12)$$

Feichtinger et al. modified the equation (12) by introducing a factor  $f$  [19]. The value of  $f$  varies from 0 to 1 and was considered to be related with slag viscosity.

$$\frac{dR}{dt} = -\frac{c_s^l - c_0^l}{c^s - c_s^l} \cdot \frac{D}{R} - f \cdot \frac{c_s^l - c_0^l}{c^s - c_s^l} \cdot \sqrt{\frac{D}{\pi \cdot t}} \quad (13)$$

Equations (12) and (13) consider the deviation from steady state, however, these equations approximate the solution of the diffusion equation only, not for the diffusion-convection equation and they don't fully consider the Stefan flow. In equations (10) and (11), the Stefan flow is neglected. It is essential to include the Stefan flow in the evaluation methods. It arises from the fact that the interface is impermeable for the non-dissolving species 2, which comprises all non-dissolving constituents of the melt in the case of effective binary diffusion. This triggers a flow perpendicular to the interface, balancing the diffusion of species 2 and contributing to the mass transfer of species 1 [4]. Equation (14) combines both diffusive and convective transport due to Stefan flow and describes the entire mass flow of a dissolving species from the boundary layer into the Slag [3]. This mass balance is known as Stefan condition.

$$-\frac{dx_0}{dt} \cdot c^s = \underbrace{-D \cdot \frac{dc^l}{dx} \Big|_{x=x_0}}_{\text{Diffusive term}} \underbrace{- \frac{dx_0}{dt} \cdot V_v \cdot c_s^l}_{\text{Convective term}} \quad (14)$$

Here,  $\frac{dc^l}{dx} \Big|_{x=x_0}$  is the concentration gradient at the slag-refractory interface,  $x_0$  the interface coordinate, and  $\frac{dx_0}{dt}$  is the velocity of the interface.

Here the Stefan condition is applied for a dissolution of a particle in a molten slag and the sphere radius  $R$  is introduced in place of  $x_0$ . The concentration derivative is replaced by the difference quotient and the effective diffusion boundary layer thickness is assumed equal to the sphere radius  $R$  (Particle radius). Equation (15) is obtained from the mass balance of the equation (14) after rearrangement and represents the SCM including the convective part of the mass flux.

$$\frac{dR}{dt} = -\frac{D \cdot (c_s^l - c_0^l)}{R \cdot (c^s - V_v \cdot c_s^l)} \quad (15)$$

The inaccuracy of equation (15) may be due to convection in addition to the Stefan flow and deviation from the steady state. The assumption of effective boundary layer thickness,  $\delta = R$

is based on steady state, under this condition, it holds for the diffusion not for the diffusion-convection equation, which is not accurate enough in all cases. All equations ((10)-(13), (15)) quoted here so far for the diffusivity determination from CLSM studies, do not include the impact of additional slag motion. This has been observed to occur frequently for several reasons. Thermal heterogeneity causes liquid flow not only because of density differences, but also possibly owing to Marangoni convection driven by temperature-dependent slag surface tension. Furthermore, the Marangoni effect may also occur owing to concentration differences at the liquid surface, which also results in surface tension gradients. In all cases, fluid motion decreases the effective diffusive boundary layer thickness and therefore, increases the mass transfer. In [4] the effect of bath movement was considered in a more realistic manner. The approach used there originates from a Sherwood relation for a sphere and assumes that the relative velocity between solid and fluid is proportional to  $R^2/\nu$  [4], [3], [20]. This results in the equation (16) below, from which the effective boundary layer thickness according to equation (17) can be seen.

$$\frac{dR}{dt} = -D \cdot \frac{1 + K \cdot R^{1.5}}{R} \cdot \frac{c_s^l - c_0^l}{c^s - V_v \cdot c_s^l} \quad (16)$$

$$\delta = \frac{R}{1 + K \cdot R^{1.5}} \quad (17)$$

The parameters  $D$  and  $K$  can be determined from an experiment by an inverse calculation procedure.

Mass transfer equations can be used to determine diffusivity from rotating finger or disc test experiments. Sherwood correlations are frequently used to calculate mass transfer coefficient. Using Cochran's equation [21], Levich introduced the famous equation (18) for the mass transfer of a disc shaped surface of infinite radius submerged in a semi-infinite medium [22]. This equation provides an accurate approximation to the mass flux density for real finite geometries when the velocity boundary layer thickness is much smaller than the disc radius. Furthermore, the mass flux density is uniform throughout the disc surface, as a result this equation can be applied to estimate the change in length of a cylindrical sample which was reported by Cooper and Kingery [23].

$$Sh = \frac{\beta \cdot R}{D} = 0.62Re^{1/2}Sc^{1/3}; \quad Re = \frac{\omega R^2}{\nu} \quad (18)$$

Here,  $R$  is the disc radius and  $\omega$  is the angular velocity.

Amini et al. described the dissolution of disc shape lime samples in  $Al_2O_3$ -CaO-SiO<sub>2</sub> slags through rotary disc experiments. They added up the individually calculated mass flux of the dissolving species from bottom of the disc (based on Levich [22] equation) and cylindrical side surface of a rotating disc (based on Kosaka and Minowa [24] equation). They derived equation

(19) to develop the correlation between mass transfer coefficient and effective diffusion coefficient under forced convection [25].

$$\beta_{total} = \underbrace{\frac{R_1}{R_1 + 2l} \cdot 0.621 \cdot D^{\frac{2}{3}} \cdot \omega^{\frac{1}{2}} \left( \frac{\rho_{melt}}{\eta} \right)^{\frac{1}{6}}}_{Disc \ surface} + \underbrace{\frac{2h}{R_1 + 2l} \cdot 0.055 \cdot D^{\frac{2}{3}} \cdot R_1^{\frac{1}{2}} \cdot \omega^{\frac{3}{4}} \left( \frac{\rho_{melt}}{\eta} \right)^{\frac{5}{12}}}_{Side \ surface} \quad (19)$$

Here,  $R_1$  is radius of rotating sample,  $l$  is immersion depth in the melt,  $D$  is diffusivity of the dissolving species in the melt,  $\omega$  is angular velocity,  $\rho_{melt}$  is the density of the melt, and  $\eta$  is melt viscosity.

Kosaka and Minowa reported Sherwood relations for the dissolution of cylindrical metallic samples into liquid metals [24]. They characterized the dissolution process in terms of change in chemical composition of the liquid metal. They reported two Sherwood relations (cylinder radius as characteristic length) (equations (20) and (21)) for two different range of validity.

$$Sh = 0.4935 \cdot Re^{\frac{1}{2}} \cdot Sc^{\frac{1}{4}}; \quad 10^3 < Re^2 \cdot Sc < 10^8 \quad (20)$$

$$Sh = 0.1390 \cdot Re^{\frac{2}{3}} \cdot Sc^{\frac{1}{3}}; \quad 10^8 < Re^2 \cdot Sc < 10^{11} \quad (21)$$

Eisenberg et al. reported the work on ionic mass transfer. Their proposed equation can be implemented for the dissolution of solid in melt. Equation (22) represents the Sherwood relation for the dissolution. One limitation is that the Schmidt number was 2230 to 3650 for the experiments from which equation (22) was deduced. But usually for the dissolution of oxide in slags, Schmidt number is much higher [26].

$$Sh = 0.0642 \cdot Re^{0.7} \cdot Sc^{0.356} \quad (22)$$

In many cases it is found that a heat/mass transfer analogy is used and Nusselt correlations are translated into Sherwood relations for estimating mass flux density. Tachibana and Fukui reported different empirical equations for heat transfer in different setups [27]. Heat transfer in annuli with a rotating inner cylinder is quite similar to the dynamic finger test for dissolution. Equation (23) is the Sherwood relation transformed from the Nusselt relation for the aforesaid setup, where specimen radius is considered as characteristic length. When Sherwood relation is transformed from Nusselt relation and this Sherwood relation is utilized to calculate mass flux density, one should incorporate moving boundary condition due to relative motion of solid/melt interface and Stefan's velocity. These two phenomena are missing in case of heat transfer problem. This incorporation will be discussed later in section 3.3.2.5.

$$Sh = 0.21 \cdot (Ta^2 \cdot Sc)^{\frac{1}{4}} \cdot \left( \frac{R_1}{R_2 - R_1} \right) = 0.21 \cdot Re^{\frac{1}{2}} \cdot Sc^{\frac{1}{4}} \cdot \left( \frac{R_2 - R_1}{R_1} \right)^{-\frac{1}{4}}; \quad Ta \leq 10^4 \quad (23)$$

$$\text{with } Ta = \frac{\omega \cdot R_1^{\frac{1}{2}} \cdot (R_2 - R_1)^{\frac{3}{2}}}{\nu} \text{ and } Re = \frac{\omega \cdot R_1^2}{\nu}$$

Here,  $R_1$  is the radius of cylinder specimen and  $R_2$  is the radius of crucible.

Guarco et al. reported a method for determination of diffusivities in the dissolution of dense ceramic materials even for large Schmidt number [28]. This method also considered the advection that occurs in an orthogonal direction to the solid/melt interface and the effect of the Stefan's velocity on the boundary layer thickness. They applied two different ways in this methodology to determine effective binary diffusion coefficients. The first approach equalized the experimental mass flux density with the average mass flux density that was calculated with the simulation. The second method applied curve fitting along the end worn profile with a simulated profile. They believe that the latter approach is the most accurate because it includes fewer approximations for the unknown geometry of the tip sample; however, both methods are consistent in that they deliver similar results. They used the experimental results from continuous wear testing device (CWTD) [28]. Details of CWTD will be discussed later in this thesis.

## **2.2. Experimental setups for dissolution studies**

### **2.2.1. Static corrosion test**

In static corrosion test, there is no relative motion between refractory and slag bath. As a result, the species boundary layer thickness grows with corrosion time which decreases the aggressiveness of dissolution [29], [30]. Due to this and further considerable drawbacks the result of this test method may largely deviate from actual refractory corrosion in the industrial vessels. Static tests will generally give lower corrosion rates compared to that is observed under real working conditions. Anyway, these tests are beneficial to study the interaction and chemical reactions that take place between the refractories and the corrosive media [31].

#### **2.2.1.1. Cup or crucible test**

A cubic sample of specified dimension as per testing standard is cut from a refractory brick or sample is prepared by pressing or casting with appropriate recipe. A vertical central bore is prepared by core drilling, truncation of core and milling of bottom. Required amount of slag/other charge materials (e.g., raw mix, clinker) is fed in the borehole of the refractory sample and placed in a laboratory furnace to heat up to the elevated temperature according to the specified heating schedule. If required, the atmosphere in the furnace can be controlled. After cooling, the sample is cut diagonally so that the borehole axis is on the cutting plane and evaluated to measure the corroded and penetrated depth. Advantage of this approaches are that the test can be performed easily, and number of samples can be tested at a time. But there are many severe drawbacks: one can receive only comparative information about corrosion resistance of the refractories, there is no bath movement, no temperature gradient and aggressiveness of the slag decreases with saturation of slag [29], [31]–[35]. For the aims of this thesis work it provides no information. **Figure 2** is the schematic representation of crucible test [31].



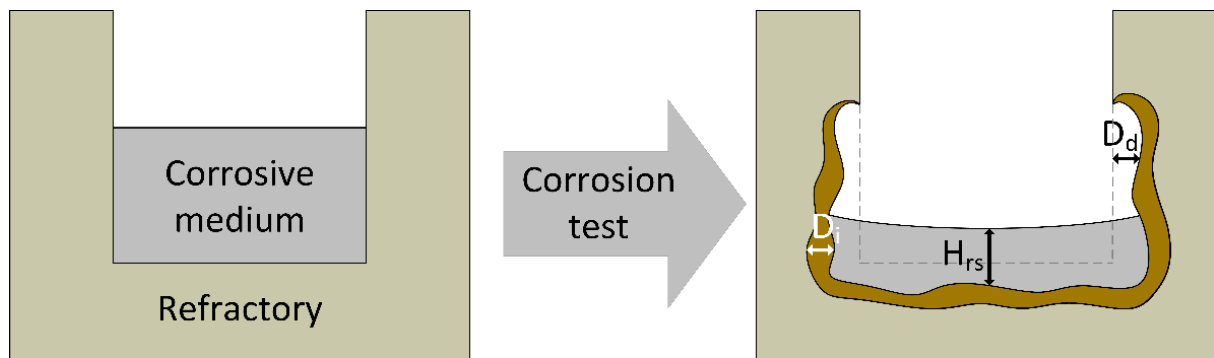


**Figure 2: Schematic of crucible test;  $D_d$  is the dissolved refractory thickness,  $D_i$  is the infiltration depth and  $H_{rs}$  is the remaining slag level [31].**

### 2.2.1.2. Static finger test

The static finger test can also be called immersion or dipping test. A cylindrical refractory sample is prepared by core drilling of the refractory. The typical size of the samples is 10 to 30 mm in diameter and 50 to 120 mm in length, but samples with other dimensions can also be used. **Figure 3 a)** is a schematic representation of static finger test setup and the typical evolution of sample shape during this test is indicated in **Figure 3 b)**. The large ratio of charge to sample weight or charge renewal during the experiment helps to avoid the saturation of the corrosive liquid. To carry out the experiments, the corrosive medium is heated up in a furnace to the designated temperature. The refractory samples are usually maintained above the crucible to heat them up before the dipping to avoid thermal shock [36], [37], then they are dipped (by 30 to 70% of their length) into the molten liquid for a specified corrosion time. If the furnace is in a closed chamber the atmosphere can also be controlled [31]. Static finger test setup for more than one sample at a time can be established.

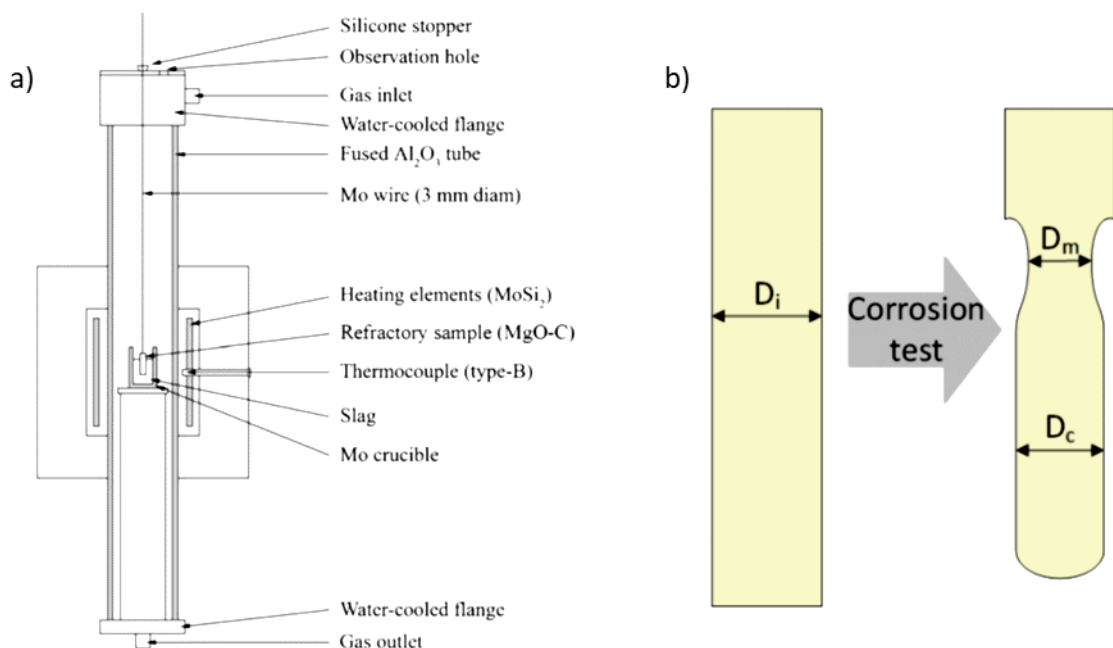


**Figure 3: a) Schematic diagram of vertical tube furnace with the setup for static finger test [38]; b) sample evolution during the static finger test, here  $D_i$  is the original sample diameter,  $D_m$  is the diameter of corrosion neck and  $D_c$  diameter of the corroded sample away from corrosion neck [31].**

After the experiment, the extent of wear can be evaluated by measuring the mass loss or dimension change at the slag-refractory-air triple-point ( $D_m$ ) where the highest degradation takes place due to Marangoni convection [39], [40] and at mid-height of the bottom part of the sample ( $D_c$ ). The evaluated results can also be used to obtain a rough approximation of the average corrosion rate [31]. The infiltration depth can be measured in addition to the decrease in diameter when the sample is cut. The static finger test has many advantages. It is relatively easier to measure, in some cases several samples can be used at a time, and as the sample is dipped in the melt this prevents solid state reaction before start of corrosion time as it is the case for the cup test. If this test is applied for determination of diffusivity, it is essential to exactly know details of the mass transfer conditions. The cases of pure molecular diffusion, Marangoni convection, buoyancy diffusion and combinations of these have to be considered. Therefore the evaluation of the test procedure may be hindered by badly defined mass transfer conditions. One way to overcome this difficulty is to overrule other influences by a sufficiently high specimen rotation, as it will be exemplified in the next sections.

### **2.2.2. Dynamic corrosion test**

In case of dynamic corrosion, there is a relative motion between refractory and corrosive melt. The fluid flow or Reynolds number is important to define effective boundary layer thickness, which leads to accurate estimation of dissolution parameters. Also the experimental conditions are usually closer to the actual industrial operating conditions compared to static test, but the experiments are more difficult to realize [29]–[31], [41]–[43].

#### **2.2.2.1. HT-CLSM study**

High Temperature – Confocal Laser Scanning Microscopy is an important tool for in-situ observation of the dissolution of micro-particles in a corrosive melt. A gold coated elliptical chamber is used as a furnace. One halogen lamp is placed at the lower focal point as energy source and sample holder is situated at the upper one point where all reflected light beams coincide to heat the slag filled crucible. Videos of the dissolution of micro-particles in the slag at experimental temperature are recorded and later evaluated to determine the dissolution rate [6], [44]. A possible relative motion between particle and melt impacts the mass transfer. Nevertheless this method enables an in situ investigation with limited effort. **Figure 4** shows the schematic diagram of HT-CLSM setup [44].

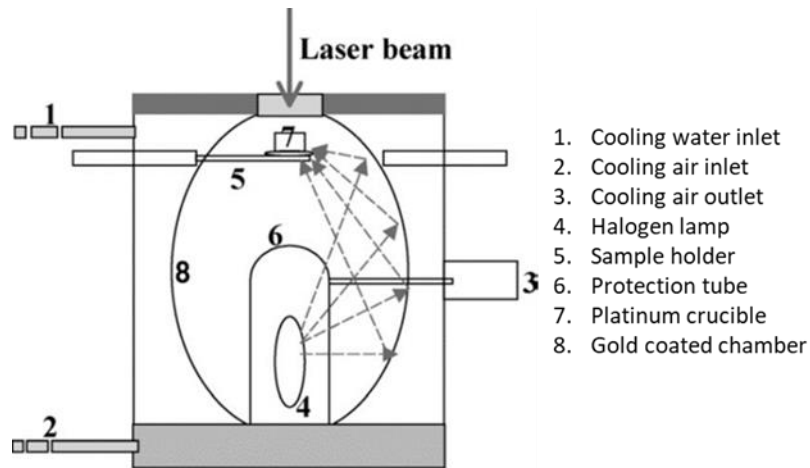


**Figure 4: Schematic diagram of high temperature confocal laser scanning microscope setup [44].**

### 2.2.2.2. Rotary slag test

A cylindrical drum is lined with refractories to be tested for corrosion resistance against corrosive charge. Solid slag and/or steel is introduced in the cylindrical chamber and melted with a burner as shown in **Figure 5 a)** [31]. The cylindrical chamber is lined with refractory bricks to create a chamber with 6 to 12 faces as shown in **Figure 5 b)** [31]. The drum is rotated horizontally at low speed with the charge causing a relative motion between refractory lining and molten slag. To avoid saturation slag is discharged after some dissolution time by tilting of the drum and new slag is fed [45]–[47]. After testing, the samples can be examined by visual inspection, and the dissolution and infiltration of different materials can be compared in relative terms if they are tested together; the phases and the composition can be analyzed using X-ray diffraction (XRD) and combined scanning electron microscopy – energy dispersive X-ray spectroscopy (SEM-EDS) [31]. In this test setup, there is a temperature gradient similar to the actual industrial operation. A further advantage of this experimental setup is that many samples can be tested and compared at a time. Attention should be paid to their compatibility and comparable corrosion rates for specimens lined in different rings [31], [48]. It may be difficult to control the temperature accurately and as a result, reproducibility of the test may be limited. Relatively large amount of refractory and charge materials are required for this test [29].

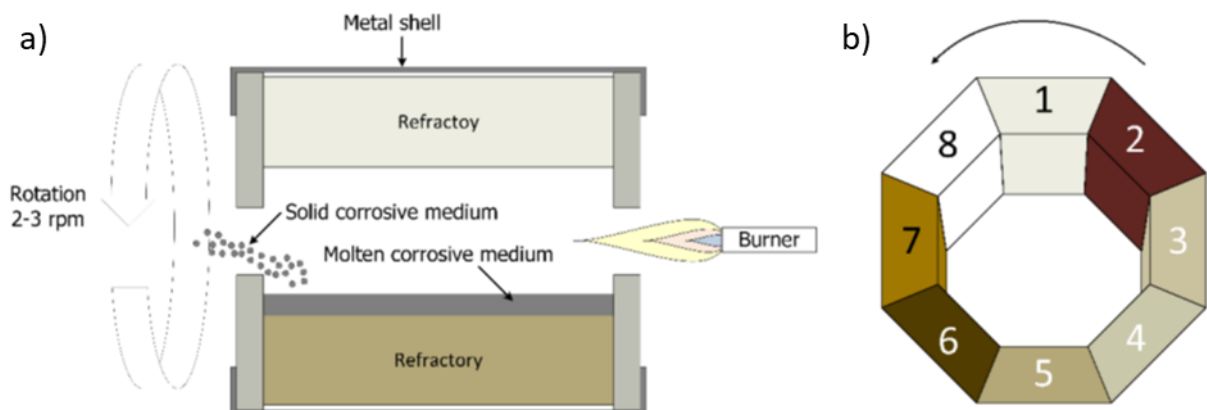


**Figure 5: a) rotating chamber; b) Schematic of refractory lining in the rotating chamber [31].**

### 2.2.2.3. Rotating finger test

The rotating finger test is quite similar to the static finger test, only a motor assembly is additional here to rotate the refractory cylinder. Sample is dipped in molten slag in a laboratory furnace and rotated with a suitable chosen speed inside the molten slag in order to provide well defined mass transfer conditions. Experiment can be conducted with varying experimental temperature, rotational speed (rpm), and corrosion time. In general, after each experiment, the corroded sample is evaluated to determine the corrosion rate at different experimental conditions. But with some advanced setups like the CWTD established and used here, corrosion parameters can be measured at experimental temperature with varying corrosion time steps in one experiment. Details of CWTD will be discussed in section 3.1.2. A well-defined boundary layer thickness is the main motivation and advantage for the rotating finger test. [23], [25], [30], [41], [43], [49]–[62].

**Table 1** compares of corrosion parameters for the above mentioned setups and shows advantages and disadvantages. Reynaert et al. reported a similar comparison table in their review paper [31]. Only both finger tests and the HT-LSCM show the potential to allow diffusivity calculations.

**Table 1: Comparison of corrosion test parameters.**

Test type →	Static corrosion test		Dynamic corrosion test		
Parameters ↓	Cup test	Static finger test	HT-CSLM	Rotary slag test	Rotating finger test
Thermal gradient	No	No	No	Yes	No
Slag/Refractory (volume)	Low	High	Very high	Medium	High
Slag renewal	No	No	No	Yes	No
Temperature control	Good	Good	Very good	Difficult	Good
Atmosphere control	Possible	Possible	Possible	Impossible	Possible
Slag agitation	No	No	Medium	Strong	Strong
Cost	Cheap	moderate to expensive	Expensive	moderate to expensive	Expensive
Scale	Low	Medium	Very low	High	Medium

## 2.3. Evaluation techniques for dissolution index

One of the important steps in corrosion experiment is evaluation of the corroded refractory sample to determine the results in a revealing manner. Evaluation can be carried out in-situ or as a post-mortem analysis. Corrosion of refractory can be represented through different approaches which have been discussed below.

### 2.3.1. Dissolution rate in terms of change in dimension

The most popular evaluation technique is change in dimension of the refractory sample with time. It is observed that some researchers reported directly the dimension change, e.g. change in diameter or radius [23], [53]–[55]. On the other hand normalized dimension e.g. normalized

diameter is a tool to represent the corrosion trend [61], [62]. Normalized dimension is the ratio of a particular dimension after corrosion experiment to initial dimension. Sometimes the surface of corroded refractory sample becomes highly rough, and it is hard to measure the dimension with accuracy due to unevenness. In this case an equivalent radius is calculated from weight ( $w$ ), height ( $h$ ) and density ( $\rho$ ) of the refractory as per equation (24) [52]. This equivalent radius is used to determine the corrosion index.

$$R_{eqv.} = \sqrt{\frac{w}{\rho \cdot \pi \cdot h}} \quad (24)$$

### **2.3.2. Relative remaining volume**

Relative remaining volume of the corroded refractory sample is another way of expression for corrosion index. It indicates remaining volume of refractory sample after corrosion experiment with respect to initial volume [41].

### **2.3.3. Reaction area**

When the degree of corrosion reaction is low, the change in dimension and weight are also significantly small. In this case, one section from the bottom of the refractory sample is cut after corrosion experiment. Polished section is analyzed by optical microscope and reaction area is measured by the image processing software to represent the corrosion index [52].

### **2.3.4. Change of dissolving refractory species concentration in the slag**

Refractory species dissolve in molten slag in every corrosion experiment. The concentration of dissolving refractory species in slag is a function of the dissolved amount. Change in concentration of dissolving species in slag can be measured after corrosion experiment. It can serve as a corrosion index in correlation with other corrosion experiment parameters [25], [30], [56], [58], [59].

## 3. Experiment

### 3.1. Experimental setup

It was exemplified above (2.2) that the experimental setup is very important to yield reliable and realistic results from a corrosion experiment. Dynamic corrosion experiments with an in-situ measurement system can provide more accurate results which can be used to calculate diffusivities. Due to this advantage, in this study HT-CLSM and CWTD have been adopted for dissolution experiments.

#### 3.1.1. High temperature confocal laser scanning microscope (HT-CLSM)

High-temperature confocal laser scanning microscopy facilitates high-resolution images at both room and very high temperatures (approx. 1650°C). It combines the advantages of a gold coated elliptical mirror furnace with those of confocal optics including a laser system with camera to capture images. The elliptical mirror furnace allows for high heating and cooling rates.

##### 3.1.1.1. Construction

The HT-CLSM used in this research work is situated at the Chair of Ferrous Metallurgy at the Montanuniversitaet Leoben [63], [64]. **Figure 6** shows the photograph of the HT-CLSM, it consists of a (1) laser head, a (2) laser confocal microscope from Lasertec (type VL2000DX) with a (3) objective turret, the (4) mirror furnace from Yonekura (type SVF17-SP) including the (5) furnace control unit and a (6) gas cleaning system. Inlet/outlet lines for the water cooling of mirror furnace and compressed air-cooling system for the halogen lamp are attached to the furnace. In addition, a PC is employed for furnace control and video recording, as well as controllers for the laser head and the horizontal movement of the furnace.

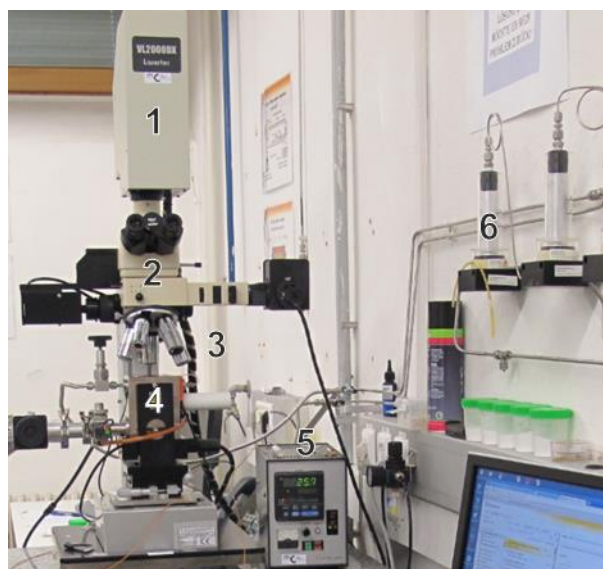


**Figure 6:** Photograph of HT-CLSM situated at the Chair of Ferrous Metallurgy at Montanuniversitaet Leoben: (1) laser head, (2) laser confocal microscope, (3) objective turret, (4) mirror furnace, (5) furnace control unit and (6) filter for gas cleaning [2].

The high-temperature chamber has the shape of an ellipsoid, at the lower focal point of the ellipsoid, a 1500 watt halogen lamp is situated, which heats a sample on a sample holder in the upper focal point to a maximum temperature of approx. 1650°C. This heating method enables heating rates of up to 1200°C/min and cooling rates of a maximum of 1000°C/min. The S-type thermocouple is situated at the lower surface of the sample holder to measure the furnace temperature. The furnace chamber is coated with gold because it reflects the infrared light very well [65], thus facilitates to achieve very high heating rate and also it is chemically inert. The halogen lamp is enclosed in a quartz glass tube through which compressed air flows. The flow rate can be regulated and thus the lamp can be cooled. The furnace chamber is water cooled to maintain lower temperature at the outside of furnace chamber and to achieve higher cooling rate. A temperature sensor at the outside of the furnace chamber is interlocked with the furnace program as a safety feature. If the temperature at the outside exceeds 50°C due to insufficient water cooling, the furnace program will automatically stop, and the furnace will start to cool. It is possible to evacuate the furnace chamber and the furnace atmosphere can be adjusted to be inert, oxidizing or reducing by means of various purging gases. The control unit for the laser head of the laser confocal microscope enables the head to be moved vertically for focusing. The controller for the mirror furnace allows for the horizontal movement in order to set the desired sample area or to follow a dissolving particle in a slag. The brightness of the image can be adjusted by this controller during the capture of images. **Figure 7** shows the radiography of the mirror furnace available at Chair of Ferrous Metallurgy at Montanuniversitaet Leoben.

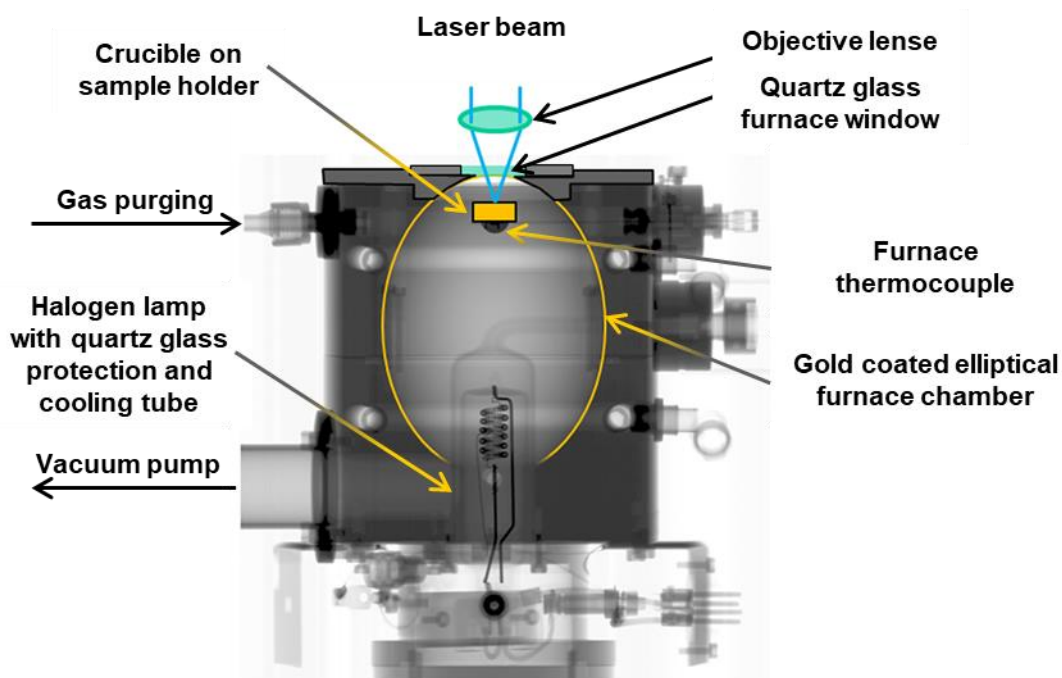


**Figure 7: Radiography of the mirror furnace at the Chair of Ferrous Metallurgy at Montanuniversitaet Leoben [2].**

In addition to the furnace, the imaging system is particularly important to get information about the sample as much as possible at high temperatures. The beam path of a confocal optic can

be seen in **Figure 8** [66]. In the HT-CLSM, a laser beam is focused on the sample via a pinhole through an objective and the light reflected (and also fluorescent radiation) by the sample is then focused on a photon detector through another pinhole and a beam splitter. An image of the sample surface is created by scanning it [67]. Detailed description of the HT-CLSM technique can be found in the publications of Chikama and Yin [68], [69].

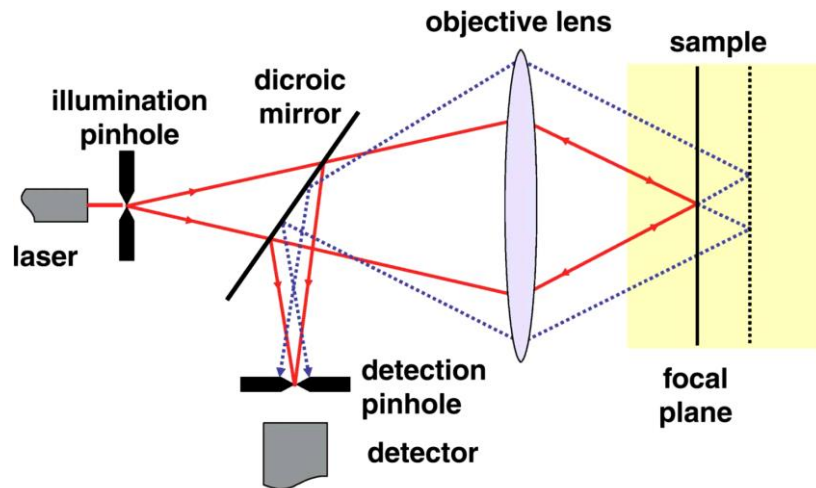


**Figure 8:** Beam path of confocal optic used in HT-CLSM for higher resolution at focal plane [66].

The CLSM technique works with a confocal pinhole, which only allows the incident light from the focal plane to pass through to the detector. The pinhole blocks the scattered light and the thermal radiation emitted from the specimen other than the focal plane [67]. This can be seen in **Figure 8**. Jones et al. examined the image resolution of the CLSM in comparison to conventional microscopy [67]. They observed that the maximum intensity in CLSM occurs only for the focused plane which implies that the axial resolution of the CLSM technique is high with short depth of field, though the depth of field increases with decreasing magnification. **Figure 9** shows this comparison. Hence, only the polarized reflection of the high intensity laser beam reaches the imaging sensor, thereby it is possible to observe samples at high resolution at elevated temperatures [67].



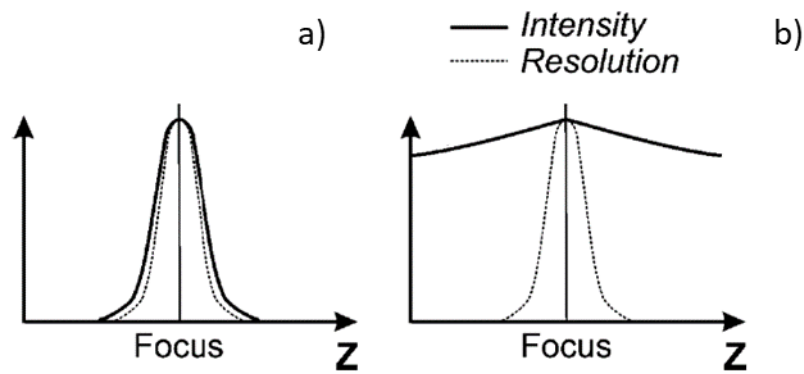


**Figure 9: Comparison between confocal (a) and conventional microscopy (b), with Z being the (vertical) distance from the objective lens [67].**

In case of high-temperature chamber in combination with a light microscope, the contrast is reduced at elevated temperatures, since the characteristic spectrum of glowing bodies approaches that of the standard illumination of microscopes with increasing temperature. The HT-CLSM overcomes this limitation by using a laser as a radiation source whose wavelength (408 nm in the present work) is far below that of the characteristic spectrum of the thermal radiation from a body glowing at around 1600°C [63].

### 3.1.1.2. Application

Confocal laser scanning microscopy covers a wide range of application at extensive temperature range. It is a powerful optical tool to observe the dissolution of particle in melt at elevated temperature, phase transformation with temperature, crystallization of melt, temperature of first melt formation and structure of biopolymer mixtures and food product in micrometer range. For this research work, it is used to observe the dissolution behavior of oxide particles in slags at varied experimental temperatures.

Velde et al. used CLSM to visualize the biopolymer mixtures to get the added advantage of sample thickness over light microscopy [66]. Tromp et al. studied the texture development in food biopolymer (gelatin, polysaccharides) in three dimensions using CLSM [70]. Blonk et al. used CLSM based method to determine the phase behavior of aqueous mixtures of biopolymers [71].

Sridhar presented the summary about application of confocal scanning laser microscopy in steel research at high temperature [72]. T. Emi and coauthors at Tohoku University, Japan did innovative research work in the field of metallurgy using HT-CLSM [68], [69], [73], [74]. Chikama et al. used HT-CLSM for real time observation of cellular and cellular to dendritic transition of crystal growing in Fe-C alloy melts [68]. Shibata et al. reported the peritectic solidification in Fe-C alloys [73]. In a further research work they also performed real time observation of nonmetallic inclusions interaction with advancing melt/solid interface of steel [74]. Yin et al. published their research work on the in-situ observation of the dynamic behaviors of grain and interphase boundaries of low carbon steel at high temperatures [69]. Bernhard and coworkers of Montanuniversitaet Leoben also published innovative research work in the field of metallurgy using HT-CLSM [75]–[78]. Fuchs et al. presented the use of HT-CLSM as a tool for indirect determination of precipitates by real-time grain growth observations

[75]. Fuchs et al. also reported the potential and limitations of direct austenite grain growth measurement by means of HT-CLSM [76]. Bernhard et al. reported the research work on high temperature phase equilibria in the iron rich part of the Fe-P and Fe-C-P system [77]. They tried to link the differential scanning calorimetry (DSC) measurements with HT-CLSM observations to visually identify phase stabilities and estimate transformation temperatures. Fuchs et al. also reported in-situ investigation of austenite grain growth processes in steels using HT-CLSM [78].

HT-CLSM is also a powerful tool to investigate the crystallization behavior of melts. Sohn and Dippenaar compiled the research work on crystallization of continuous casting slags using HT-CLSM [79]. Prapakorn et al. compared the different techniques for the determination of crystallization temperatures of slags including HT-CLSM [80]. Ryu et al. reported the investigation of the crystallization behavior of TRIP-steel slags with varying alumina contents and with different basicity [81]. Zhang et al. investigated the influence of basicity on the crystallization behavior of fluorine-free casting slag using single hot thermocouple technique (SHTT) and HT-CLSM [82]. Kircher investigated crystallization behavior in his doctoral thesis [2].

Dissolution of non-metallic refractory particles in slags using HT-CLSM is a major part of this research work. On this topic, several publications have been made available in last two decades. In various references the dissolution of  $\text{Al}_2\text{O}_3$ ,  $\text{MgO}$ ,  $\text{MgAl}_2\text{O}_4$ ,  $\text{SiO}_2$ ,  $\text{ZrO}_2$  and  $\text{SiC}$  in different kind of slags at varied experimental temperatures are reported. Mostly, synthetic slags were used for those dissolution experiments using HT-CLSM, as the HT-CLSM is limited to only transparent or at least translucent slags for dissolution experiments. It means only very small amount of coloring elements are permitted in the slag composition.

Liu et al. studied the dissolution of fused  $\text{MgO}$  particles in  $\text{CaO-Al}_2\text{O}_3\text{-SiO}_2$  (CAS) ( $\text{CaO/SiO}_2$  wt. ratio of 0.65) and  $\text{CaO-Al}_2\text{O}_3\text{-SiO}_2\text{-MgO}$  (CASM) ( $\text{CaO/SiO}_2$  wt. ratio of 0.76) slags at  $1600^\circ\text{C}$  [6]. They used shrinking core model (SCM) to interpret and describe the dissolution process. They observed a secondary layer formation around the dissolving  $\text{MgO}$  particle in CASM slag which consisted of  $\text{MgAl}_2\text{O}_4$  spinel and  $\text{CaMgSiO}_4$  (CMS, Monticellite) phases. They also believed that spinel was formed in-situ during the dissolution process at experimental temperature whereas CMS was formed during cooling. They explained the dissolution of  $\text{MgO}$  in CASM slag as an indirect dissolution [6].

Liu et al. in-situ observed dissolution of spherical  $\text{Al}_2\text{O}_3$  particles in a CAS slag at temperatures from  $1470^\circ\text{C}$  to  $1630^\circ\text{C}$  [13]. They concluded that neither the chemical reaction nor the boundary layer diffusion in the classical SCM can fully explain the dissolution behavior of spherical  $\text{Al}_2\text{O}_3$  particles. They applied the concept of diffusion-controlled dissolution in a stagnant liquid. In this case, the reaction kinetics are assumed to be infinitely faster compared to the diffusion process so that at the interface the saturation concentration is developed very fast. The solid phase dissolves at the rate at which the diffusion flux can remove the dissolving species away from the interface toward the bulk of the liquid. They derived the one dimensional diffusion equation in spherical coordinates and solved it with lattice Boltzmann model (LBM) [13].

Liu et al. also investigated the dissolution of  $ZrO_2$  particles in mould fluxes at 1450°C, 1480°C and 1510°C [14]. They used CaO- $Al_2O_3$ - $SiO_2$ - $Na_2O$ - $B_2O_3$  (CASNB) slags with CaO/ $SiO_2$  wt. ratio of 1.0 and 0.5. Here they also first used classical SCM and later diffusion-controlled dissolution in a stagnant liquid. They compared the normalized experimental dissolution curves for  $ZrO_2$  with the theoretical curves to determine the rate limiting step. They concluded that the dissolution of  $ZrO_2$  in the mould flux with CaO/ $SiO_2$  wt. ratio of 1.0 can be described by SCM as diffusion controlled, whereas dissolution in other flux with CaO/ $SiO_2$  wt. ratio of 0.5 follows the proposed diffusion equation [14].

Monaghan et al. studied the dissolution of  $Al_2O_3$  micro particle in a CAS slag using HT-CLSM over the temperature range of 1477°C to 1577°C [7], [9]. They used SCM to determine the rate controlling mechanism and diffusivity. They also investigated the dissolution of  $Al_2O_3$ ,  $MgAl_2O_4$  spinel and  $ZrO_2$  inclusions in a CAS (CaO/ $SiO_2$  wt. ratio of 0.25) slag [8]. They found that the rate of alumina dissolution is slower than that of spinel. They faced problems with the evaluation of  $ZrO_2$  inclusion due to the bubble formation on the  $ZrO_2$  inclusion [8].

Yi et al. investigated the dissolution behavior of  $Al_2O_3$  and MgO inclusions in  $Al_2O_3$ -CaO-MgO slags over the temperature range of 1450°C to 1550°C [17]. To analyze the dissolution mechanism, they considered the surface reaction control and boundary layer diffusion according to SCM as well as diffusion of the dissolving species into a stagnant fluid. In the latter case the relations between radius and time in the diffusion model are calculated using numerical simulation, because it is difficult to obtain an analytical solution of the spherical diffusion equation with moving boundary. They also found that sometimes it is difficult to verify the dissolution mechanism by direct comparison of normalized experimental curves with theoretical one, because the differences between the curves, especially between diffusion according to SCM and proposed diffusion equation, are comparable to the experimental scatter. To overcome this problem, they introduced three dissolution parameters, one of them is constant over measured radius for a particular dissolution mechanism. They observed that for the dissolution in  $Al_2O_3$ -CaO-MgO slag,  $Al_2O_3$  dissolution was best explained by a diffusion controlled dissolution process, whereas MgO dissolution appears to be controlled by chemical reaction kinetics ( $R/R_0 = 1 - t/t_{tot}$ ), where  $R$  is particle radius at time  $t$ ,  $R_0$  is initial radius,  $t_{tot}$  is total dissolution time. They also observed that alteration of the slag composition away from the level of  $Al_2O_3$  or MgO saturation by a few percent resulted in a drastic increase in the rate of dissolution. They quantified this change in terms of activation energy [17].

Sridhar and Cramb studied the kinetics of  $Al_2O_3$  dissolution in CASM (CaO/ $SiO_2$  wt. ratio of 0.84) slags over the temperature range of 1430°C to 1550°C [10]. They investigated dissolution of fused alumina particles in ultra-high purity argon atmosphere with the classical SCM.

Valdez et al. investigated the dissolution of fused alumina particles in CAS and CASM slags at 1470°C, 1500°C and 1530°C [11]. The slags used in this investigation are representative for ladle and tundish slags. They observed the particle morphology during the dissolution experiments. Alumina particle surface was smooth when dissolving in CAS slag, but it was rough in CASM slag. They predicted that the surface roughness was due to secondary reaction layer, and it was confirmed as  $MgAl_2O_4$  spinel reaction layer by SEM-EDS. To investigate the mechanism responsible for dissolution, the classical SCM was used. They concluded that the

average dissolution curve fits the boundary layer diffusion model for the low silica slag and lies between reaction control and diffusion in boundary layer control for the high silica slags. They concluded that this latter behavior could be caused by a change of mechanism during the dissolution process from reaction controlled ( $R/R_0 = 1 - t/t_{tot}$ ) to diffusion controlled ( $R/R_0 = (1 - t/t_{tot})^{1/2}$ ) once the boundary layer is formed [11].

Valdez et al. also investigated the dissolution behavior of  $Al_2O_3$ ,  $MgO$  and  $MgAl_2O_4$  particles in a CAS slag in the temperature range of 1470°C to 1550°C [12]. Here also they used classical SCM to investigate the mechanism responsible for the dissolution. They found that the dissolution mechanism curves lie between the reaction control and diffusion in boundary layer mechanism for  $Al_2O_3$  and the  $MgAl_2O_4$  dissolution. The dissolution of  $MgO$  seems to follow the boundary layer diffusion mechanism [12].

Fox et al. studied the dissolution behavior of  $ZrO_2$ ,  $Al_2O_3$ ,  $MgO$  and  $MgAl_2O_4$  particles in a  $B_2O_3$  containing commercial fluoride-free mould slag [83]. Non-metallic inclusions composed of  $ZrO_2$ ,  $Al_2O_3$ ,  $MgO$  and  $MgAl_2O_4$  are associated with the problems during the continuous casting of steels and so it is necessary that such particles dissolve completely. Therefore, the dissolution rate of the above-mentioned oxides plays an important role to design the mould flux. They investigated the dissolution behavior in HT-CLSM over the temperature range of 1250°C to 1500°C. They found that the dissolution rates of  $Al_2O_3$ ,  $MgO$  and  $MgAl_2O_4$  are comparable to one another whereas the dissolution rate of  $ZrO_2$  is four times slower. Empirical relationships have been derived which may be used to approximately predict the dissolution time for particles of these compositions in the slag. They used classical SCM and one-dimensional finite difference model (FDM) to investigate the mechanism responsible for dissolution. They observed that in all cases the rate of dissolution is surface reaction controlled, except 20% of the  $ZrO_2$  cases where some intermediate behavior between surface reaction and diffusion in boundary layer controlled was observed. They also concluded that the dissolution of  $ZrO_2$  is very slow at all investigation temperatures, hence, the removal of such particles by dissolution in the slag is not feasible. Adjusting the slag composition to further reduce the solubility of  $ZrO_2$  is suggested as a possible means to decrease the attack of  $ZrO_2$  containing refractory and hence reduce the uptake of these particles [83].

Verhaeghe et al. investigated the dissolution behavior of  $Al_2O_3$  in a CAS (CaO/SiO<sub>2</sub> wt. ratio of 0.65) slag with experimental-numerical approach [15], [16]. Dissolution experiments over the temperature range of 1470°C to 1550°C were carried out. Simulation for the dissolution of particle keeping the similarity with HT-CLSM setup was performed. Lattice Boltzmann model was applied to analyze the dissolution phenomena of arbitrarily shaped solids in multicomponent liquids. The experimental results were compared with classical SCM and lattice Boltzmann model. Good agreement of experimental results was observed with the simulation results, rather than SCM [15], [16].

Park et al. studied the dissolution behavior of SiC particle in the CaO-SiO<sub>2</sub>-MnO slags at 1600°C [84]. The wetting between SiC and slag phase was observed more dominant for higher CaO/SiO<sub>2</sub> ratio. According to their observation, the dissolution of SiC particle in the slag through the reaction with MnO is enhanced for higher CaO/SiO<sub>2</sub> ratio not only due to greater thermodynamic driving force but also due to accelerated mass transport kinetics.

Feichtinger et al. investigated the dissolution of  $\text{SiO}_2$  particles in CAS slags at  $1450^\circ\text{C}$  and analyzed the dissolution mathematically [19]. They used six types of slags with varied  $\text{CaO}/\text{SiO}_2$  ratio and viscosity. They modified a diffusion equation reported in [18] by introducing a factor  $f$ . This factor  $f$  denotes the weight of the contribution of the unsteady part of the solution. Remarkably, for some slags, the correlation of  $f$  with slag viscosity and tridymite activity has been shown [19].

Michelic et al. studied the dissolution of oxide inclusion in secondary steelmaking slags at  $1450^\circ\text{C}$  and  $1600^\circ\text{C}$  in argon atmosphere [64]. Experimental results were compared with different models to identify dissolution mechanism [19].

Kircher reported a wide range of results for the dissolution of  $\text{Al}_2\text{O}_3$  and  $\text{ZrO}_2$  in seven different mould slags and three synthetic slags at  $1550^\circ\text{C}$  [2]. He used four different models for diffusivity determination. He observed faster dissolution of  $\text{Al}_2\text{O}_3$  than  $\text{ZrO}_2$  for a particular set of experiment.

### 3.1.1.3. Crucible and thermocouple

Size and shape of the crucible are very important to produce accurate measurements and to minimize problems during experiments. Size of the crucible must be optimum so that it can be placed on the sample holder safely and it can accommodate sufficient amount of slag to maintain proper slag to particle weight ratio. In this research work this ratio has been maintained at 1000 or more to avoid any adverse effect of change in bulk concentration. If the size is too big, more amount of slag can be accommodated to maintain the ratio, but the peripheral portion of the crucible will be out of visible area. As a result, if the particle travels towards periphery during dissolution experiment, it will be missing in the video. Shape of the crucible is also vital for visibility especially at the peripheral area of the crucible. Visibility at the vicinity of the wall is poor for the crucible with straight wall and this can be improved by changing the crucible wall from straight to inclined (diameter at the top of the crucible is higher than that of bottom). Platinum and 10% rhodium (Pt-Rh10) crucibles have been used for this research work. **Figure 10** shows the drawing and photograph of the newly designed crucible for HT-CLSM experiments.

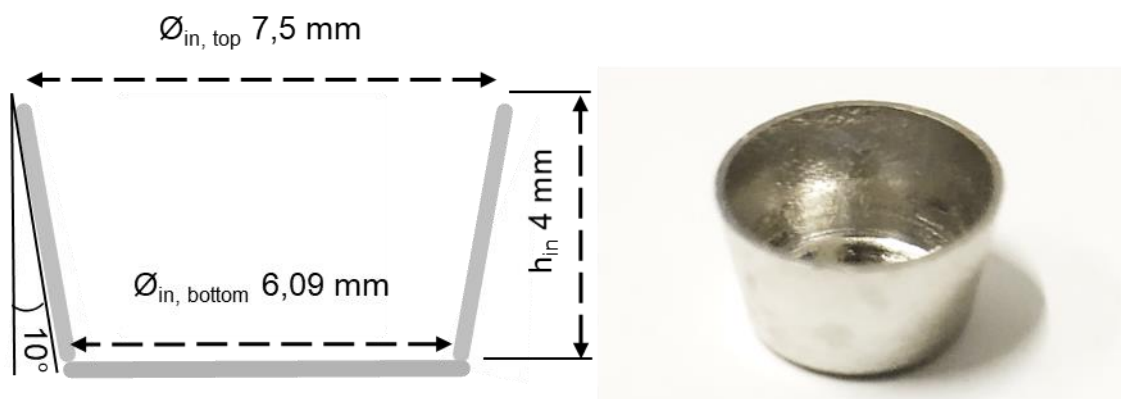


**Figure 10: Drawing and photograph of crucible used for HT-CLSM experiments.**

As discussed in section 3.1.1.1, the S-type thermocouple to measure the furnace temperature is situated at the bottom surface of the sample holder. For the current setup of HT-CLSM

experiment a thin alumina plate is placed between platinum base of the sample holder and crucible. The slag in the crucible is situated few mm above the furnace thermocouple. It is important to measure the actual slag temperature by an external S-type thermocouple embedded in the slag. The relation between furnace and sample temperatures is investigated and adopted in the temperature program to perform the experiments at actual slag temperature. Wires of 0.127 mm diameter have been used for the sample thermocouple. Due to thinner diameter of the wires, sample thermocouple is able to measure the slag temperature accurately. Temperature calibration will be discussed in details in the section 3.2.1.2.

### **3.1.2. Continuous wear testing device (CWTD)**

CWTD is the most contemporary finger test device with in-situ wear profiles measurement at experimental temperature. It is suitable for static and dynamic corrosion experiments and erosion experiments. A high-precision laser device is attached with it to measure the sample profiles at room temperature as well as experimental temperature.

#### **3.1.2.1. Construction**

The CWTD was assembled by the company NET-Automation GmbH, and it is based on a high temperature chamber furnace (type HTK 40/17/S;  $T_{\max}$  1750°C; Thermconcept GmbH) [85]. The dimensions of the chamber are (width × depth × height): 360 mm × 350 mm × 380 mm. The furnace is connected to a control board located inside an electric cabinet, where process control, data recording, and the management of the test procedure are performed digitally. An industrial PC is used for visualization, input of the digital schedule of the test procedure, data storage and laser scanner configuration [85]. The exterior view of the Continuous Wear Testing Device (CWTD) is shown in **Figure 11** [85]. Design of CWTD, operation, sample preparation, experimental procedure and evaluation procedure have been reported by Kircher et al. [85].

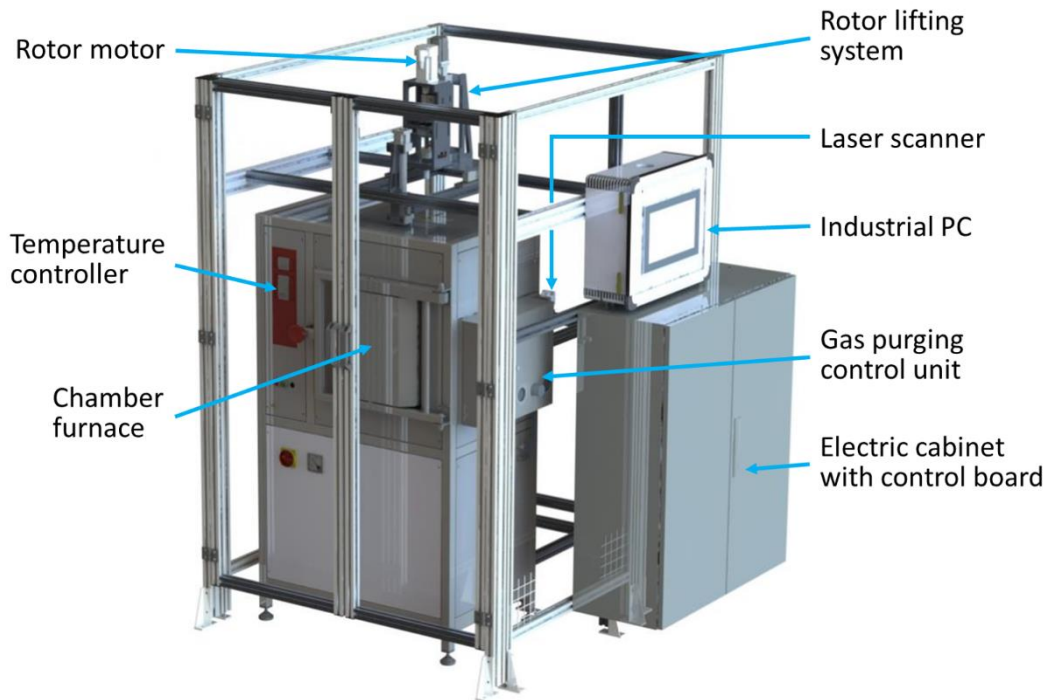


**Figure 11: Exterior view of the Continuous Wear Testing Device (CWTD) [85], [86].**

Six  $\text{MoSi}_2$  heating elements are used to attain a homogeneous temperature distribution inside the furnace chamber in order to avoid free convection in the slag bath caused by thermally induced density differences [85]. The maximum experimental temperature is limited to  $1650^\circ\text{C}$  because platinum-rhodium parts are used for the measurement. Furnace is lined with high temperature insulating material. Two thermocouples (type B) are used to measure the furnace temperature and another two thermocouples (type B) are located directly underneath the Pt-Rh10 crucible to accurately measure the slag temperature. Additionally, the temperatures of the laser sensor housing and of the load cells are measured by resistance temperature detectors (RTD;  $100\ \Omega$ ). An alumina rod is used for the vertical connection of a Pt-Rh10 sample holder to the lift-able drive which offers an adjustable speed in the range of 0-3000 rpm. The sample holder is attached to the rod with a horizontal alumina bolt, which is safeguarded against slipping by an alumina sleeve. Due to the two joints in sample assembly to the rotor system, the maximum rotational speed is limited. Above a critical speed the sample rotation largely deviates from concentric motion. A vibration sensor has been installed as a safety measure in the event that the whole rotor runs unbalanced or breaks at high speeds. In analogy to Van Ende et al. [38] the ceramic sample is fixed with a central hole in the top of the specimen and a second hole perpendicular to it. Instead of Mo wires [38], the cylinder is fixed to the central Pt/Rh sample holder ( $\varnothing\ 5\ \text{mm}$ ) with another alumina fixing bolt ( $\varnothing\ 3\ \text{mm}$ ). This setup offers the opportunity to conduct experiments with different diameters from  $\varnothing\ 20\ \text{mm}$  to  $\varnothing\ 40\ \text{mm}$  (limited by crucible diameter). The entire measuring equipment of the rotor is mounted on two parallel supports and two load cells are situated between the supports and the rotor assembly to provide information of the mass loss during a corrosion experiment. **Figure 12** shows the inside view of the furnace chamber at room temperature with a worn alumina fine ceramic specimen during a laser measurement. Apart from the laser device, the window at the back wall of the furnace is closed with a plug that is lined like the furnace. The laser scanner

situated at the reverse side of the furnace can be seen in **Figure 12** through a sapphire window mounted close to the inner lining, when the furnace plug was pulled out for the laser measurement. A fan is attached at the reverse side of the furnace which is used only during the laser measurement to cool the laser measurement system. In addition to this, there is an industrial water chiller especially to cool the laser device. **Figure 13** shows the laser scanner assembly and furnace plug at the reverse side of the CWTD. All the moving parts in CWTD are equipped with position sensors to direct their movement [85].

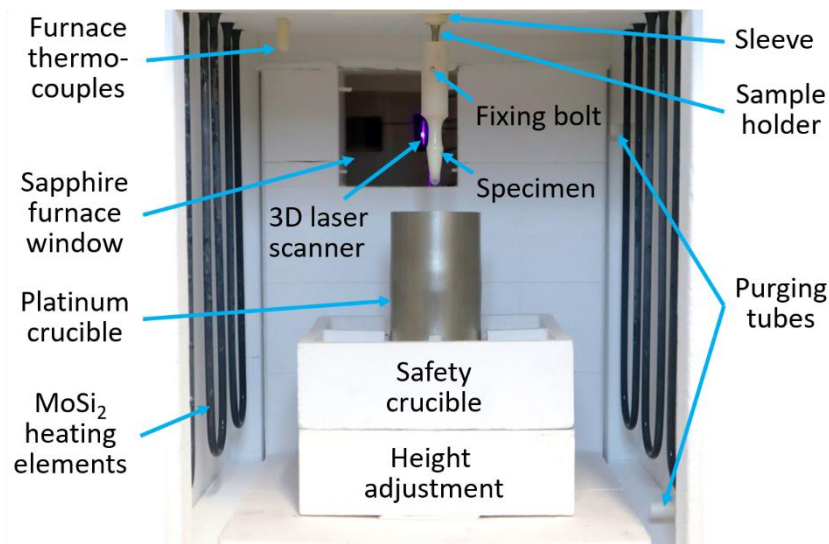


**Figure 12: Chamber furnace of the CWTD during a laser measurement of a worn  $\text{Al}_2\text{O}_3$  specimen at room temperature [85].**

Whenever required the oxygen partial pressure in the furnace chamber can be reduced by means of inert gas or Varigon (98% Ar, 2%  $\text{H}_2$ ) purging. In order to prevent the system from oxygen contamination, the furnace window is sealed with a sapphire glass and the gap between main rotor and the top of the furnace is also gas purged [85].

### 3.1.2.2. Principle of 3D laser measurement using laser line triangulation

The laser device with a laser power  $\leq 8$  mW (laser class 2 M) is installed at the reverse side of the furnace and the main components are shown in **Figure 13** [85]. The high-precision laser scanner of type LLT2900-100/BL (Micro- Epsilon Messtechnik GmbH & Co. KG) uses a semiconductor laser diode with a wavelength of 405 nm (violet-blue). Due to the fact that the wavelength is much shorter than the visible emission at test temperature, the scanner enables optical surface profile measurements of specimens at elevated temperatures. The profile sensor uses laser line triangulation for two-dimensional profile detection on the target surface [85]. Lenses enlarge a laser beam to form a static laser line that is mapped onto the sample surface and an optical system projects the diffusely reflected light of this laser line onto a highly susceptible sensor matrix. From the position of the light spots on the receiver element and the distance from the sender to the receiver element, the controller calculates the distance information (i.e., distance from the specimen axis, here addressed as z-axis) and the position alongside the laser line (i.e., height longitudinal to the specimen axis, here addressed as x-axis). The profile scan rate (i.e. the number of line scans per second) was adjusted to  $100 \text{ s}^{-1}$



and due to a the sample rotation (at 2 rpm) during the laser measurement, it is possible to obtain a full 3D measurement including circumferential values (y-axis) [85], [87].

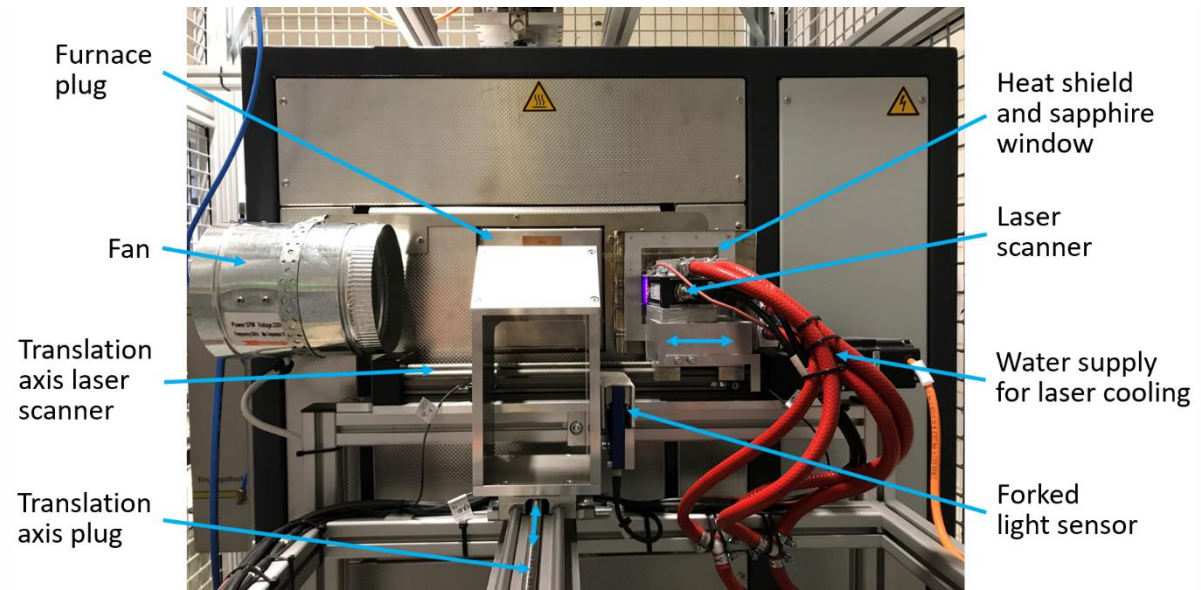


**Figure 13: Laser scanner assembly, cooling system and furnace plug at the back side of the CWTD [85].**

The laser scanner scans 3000 profile lines for a complete rotation of the sample and assembles them in a particular manner to produce the 3D pattern of the flattened sample mantle. As an example, **Figure 14** shows 3D view made of all scanned profile lines of a corroded  $\text{Al}_2\text{O}_3$  fine ceramic sample measured at  $1500^\circ\text{C}$ .

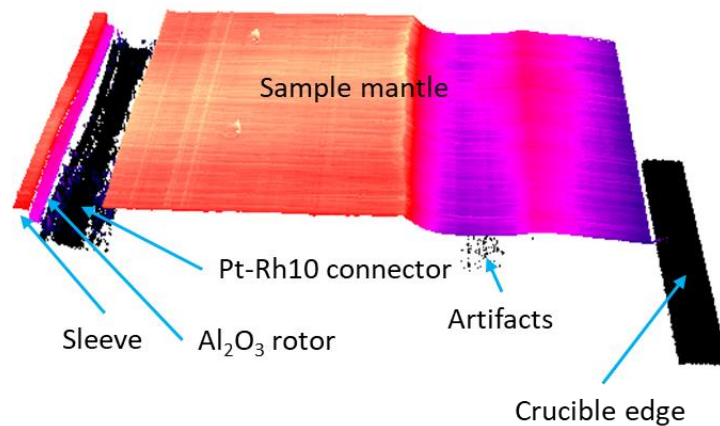


**Figure 14: 3D view of a corroded  $\text{Al}_2\text{O}_3$  fine ceramic sample surface at  $1500^\circ\text{C}$ .**

### 3.1.2.3. Application

CWTD is a newly developed contemporary wear measurement device. It is suitable for static and dynamic corrosion experiments of fine ceramics with in-situ wear measurement at experimental temperature. It is also possible to conduct erosion experiment of coarse grain materials at varied temperature range. The device has a provision of atmosphere control, erosion experiments of carbon bonded refractories are also possible. Because a Pt-Rh10

connector is used to fix the cylindrical sample to the rotor shaft, samples with varying diameter (20 mm – 40 mm) can be used. Rotation speed can be varied as per the experimental need, which allows the study of its effect on the wear rate. It is also possible to determine the critical rotational speed or critical Reynolds number, for which the effect of Marangoni convection can be suppressed. In this research work, this device has been used for static and dynamic corrosion experiments of  $\text{Al}_2\text{O}_3$  fine ceramics in silicate slags at different temperatures. Dynamic corrosion experiments of  $\text{MgO}$  fine ceramics have also been conducted at three temperatures.

As it was mentioned, this is a newly developed device and as per author's best knowledge, nobody has reported in-situ wear measurement at experimental temperature except Yuan et al. [88]. They used X-ray radiographic apparatus to take X-ray photographs at experimental temperature. Otherwise, static, and dynamic corrosion experiments and erosion experiments with post-mortem analysis have been quite popular for several decades. Some interesting research works on finger test are discussed below to understand the applications of this type of experimental setup.

Yuan et al. investigated the local corrosion of magnesia-chrome refractories due to Marangoni convection at slag-metal interface [88]. They did static corrosion experiments of seven magnesia-chrome refractories with varying  $\text{MgO-Al}_2\text{O}_3$  spinel content at  $1600^\circ\text{C}$ . They used a high-temperature X-ray radiographic apparatus for X-ray photographs of the corroded specimen inside the charged filled crucible at experimental temperature. But the sample was not clearly visible inside the melt. It is possible to estimate the shape of the corroded sample from the side where the X-ray photograph was taken, but not the extent of corrosion throughout the sample surface. They reported X-ray photographs of bath movement at slag-metal interface due to Marangoni convection. It is clear to depict the Marangoni convection path from these photographs [88].

Cooper and Kingery studied the molecular diffusion, natural convection and forced convection of sapphire dissolution in CAS melts [23]. They measured dissolution rate of single crystal sapphire in the temperature range of  $1340^\circ\text{C}$  to  $1550^\circ\text{C}$ . They found that the rate of dissolution was controlled by mass transport in the melt. They used cylindrical and disc sample for free and forced convection studies respectively. They investigated the dependency of corrosion rate on experimental temperatures and corrosion time [23].

Amini et al. investigated the effect of additives and temperature on dissolution rate and diffusivity of lime in CAS slags [25]. They carried out dynamic corrosion experiments of dense lime specimens over the temperature range of  $1430^\circ\text{C}$  to  $1600^\circ\text{C}$ . They measured the dissolution rate in terms of change in lime concentration in the slag. A strong impact of rotational speed, temperature, and slag composition on the dissolution rates was observed. They also checked the effect of additives to the slag:  $\text{CaF}_2$ ,  $\text{MnO}_x$ ,  $\text{FeO}_x$  and  $\text{TiO}_2$  increased the diffusivity of  $\text{CaO}$ , whereas  $\text{SiO}_2$  had opposite effect. Levich equation [22] for the mass transfer coefficient from the disc surface and Kosaka and Minowa [24] equation for the lateral cylinder surface have been applied. It was concluded that diffusion in slag phase is the rate limiting step [25].

Wang et al. investigated dissolution of MgO based refractories in CASM ladle slag at 1600°C [61]. Instead of a rotating finger test, a new setup for the dynamic corrosion was used, where the refractory sample is situated in the slag filled crucible and the slag is stirred with a molybdenum stirrer. After the experiment, the corroded MgO sample imbedded in solidified slag was examined under an optical microscope [61].

Wang et al. studied the kinetics of solid dissolution into liquids at elevated temperature with a new experimental design [89]. A rotating cylinder was placed concentrically in a crucible fabricated by boring four holes into a blank material for creating an internal volume with a quatrefoil profile. A strong flow in the radial direction in the liquid was created, which was evidently shown by computational fluid dynamic (CFD) calculations and experiments at both room temperature and elevated temperature. The new setup was able to quench the sample as it was at experimental temperature, particularly the interface between the solid and the liquid to understand the reaction mechanism. At room temperature they used sugar rod and water to validate the setup and at high temperature graphite crucibles were used as slag container for the experiment with MgO-Al<sub>2</sub>O<sub>3</sub> spinel and porous MgO refractories [89].

Chen et al. investigated the effect of Marangoni convection on the dissolution of a MgO refractory by a SiO<sub>2</sub>-CaO-(Al<sub>2</sub>O<sub>3</sub>)-FeO<sub>x</sub>-MgO slag with or without Al<sub>2</sub>O<sub>3</sub> keeping CaO/SiO<sub>2</sub> constant [40]. They observed that the rate of dissolution was marginally lower in the case of alumina containing slag.

Dunkl and Brückner studied dynamic corrosion of refractory materials in container glass melt at 1500°C and compared with results of 1400°C [90]. They used fused cast alumina bricks, two types of fused cast alumina-zirconia-silica bricks and alumina-chrome bricks.

Um et al. investigated the wear behavior of a MgO-C refractory in ferromanganese slags over the temperature range of 1450°C to 1600°C [52]. Three CaO-SiO<sub>2</sub> slags with varying basicity, three CaO-SiO<sub>2</sub>-Al<sub>2</sub>O<sub>3</sub> slags with fixed basicity but varying Al<sub>2</sub>O<sub>3</sub> content and one CaO-SiO<sub>2</sub>-Al<sub>2</sub>O<sub>3</sub>-MnO slag have been used for dynamic corrosion experiments with 200 to 600 rotations per minute and immersion times from 60 min to 360 min. Reaction area of a polished section served as a corrosion index when the radius of the specimen was not significantly affected, otherwise average radius reduction was employed. They observed that the corrosion of MgO-C in CaO-SiO<sub>2</sub> slags increases with increasing rotational speed and immersion time but decreases with increasing basicity. In case of CaO-SiO<sub>2</sub>-Al<sub>2</sub>O<sub>3</sub> slags corrosion decreases with increasing Al<sub>2</sub>O<sub>3</sub> content due to higher slag viscosity and spinel formation at the interface when the Al<sub>2</sub>O<sub>3</sub> content is higher than 20%. They also observed that the degradation of the MgO-C refractory immersed in CaO-SiO<sub>2</sub>-Al<sub>2</sub>O<sub>3</sub>-MnO slag is very intense due to the oxidation of the carbon in contact with MnO [52].

Jansson et al. studied the rate of dissolution of solid MgO-C and doloma refractories in CaO-Al<sub>2</sub>O<sub>3</sub>-SiO<sub>2</sub>-MgO slags at the temperature range of 1500°C to 1650°C under forced convection by rotating finger test [53]. They varied the dissolution time from 15 to 120 minutes at rotational speeds of 100 to 400 rpm to check their effect on dissolution. Corrosion rate was measured by diameter change. It was found that the corrosion rate of MgO-C and doloma refractory

materials increased with increasing rotational speed and temperature. Further, they observed linear dependency of corrosion rate with time [53].

Wang et al. investigated the corrosion behavior of a sintered high purity  $\alpha$ - $\text{Al}_2\text{O}_3$  refractory in contact with soda-lime-silicate (SLS) glass under dynamic conditions [41]. Experiments were conducted as function of rotation speed, contact time and temperature. The phase composition and microstructures of the glass-refractory interface of the corroded samples were studied by X-ray Diffraction (XRD) and combined Scanning Electron Microscopy – Energy Dispersive X-ray Spectroscopy (SEM-EDS), respectively. They compared the dynamic corrosion test results with static crucible test results and found good agreement [41].

Liang et al. studied the effect of dynamic slag/refractory interaction of a lightweight  $\text{Al}_2\text{O}_3$ – $\text{MgO}$  castable during steel refining [43]. For the castable microporous alumina aggregate was applied as a coarse grain. They observed almost similar corrosion rate compared to conventional  $\text{Al}_2\text{O}_3$ – $\text{MgO}$  castable and concluded that a light weight refining ladle lining can be applied with the same lifetime as common castables [43].

## 3.2. Experimental procedure

Sample preparation, accurate sample temperature measurement and experiments with required parameters have to be carried out carefully to generate valid results. In this section experimental procedures for HT-CLSM and CWTD will be discussed in detail.

### 3.2.1. Experimental procedure of HT-CLSM measurements

#### 3.2.1.1. Slag quenching and pre-melting

Synthetic slags have been used in the current studies. Slag batch has been prepared from pure oxide. Quartz, calcined alumina, magnesium oxide, and calcium carbonate have been used as  $\text{SiO}_2$ ,  $\text{Al}_2\text{O}_3$ ,  $\text{MgO}$  and  $\text{CaO}$  sources respectively. First decarburization of calcium carbonate and dehydration of magnesium oxide (to get rid of hydration by atmospheric moisture) were carried out at  $1050^\circ\text{C}$  for 3 hours. Every time, the weight loss was checked to ensure the complete decarburization and then immediately slag components were weighted to avoid prior hydration by atmospheric moisture. 100 g of batch for each slag were prepared. In a first step, slag batch was melted in a platinum crucible in a preheated furnace at  $1450^\circ\text{C}$  for 15 min and quenched on a steel plate. To enhance homogeneity and to facilitate its application, the solidified quenched slag was powdered in a tungsten carbide lined cup mill.

As few air bubbles as possible are desired in the slag after melting in the Pt-Rh10 crucible. Contact of the dissolving particle to the air bubble may alter the dissolution rate in CLSM experiment due to the surface tension gradient. To avoid this, the required amount of slag is pre-molten in the Pt-Rh10 crucible before the CLSM experiment. Also, it is convenient to fix the sample thermocouple inside the slag at the center of the crucible during slag pre-melting. Otherwise, if the sample thermocouple is situated at the vicinity of the crucible wall, it may touch the wall at high temperature and thus not measure the true slag temperature. **Figure 15** shows a small setup to fix the sample thermocouple at the center of the crucible. 0.2 g slag was pre-molten in each crucible in a preheated furnace at  $1450^\circ\text{C}$  for 15 min. For crucibles

with thermocouple, slags were pre-molten in one step and for crucibles without thermocouple in two steps (0.08 g + 0.12 g) for easy removal of air bubble during pre-melting.

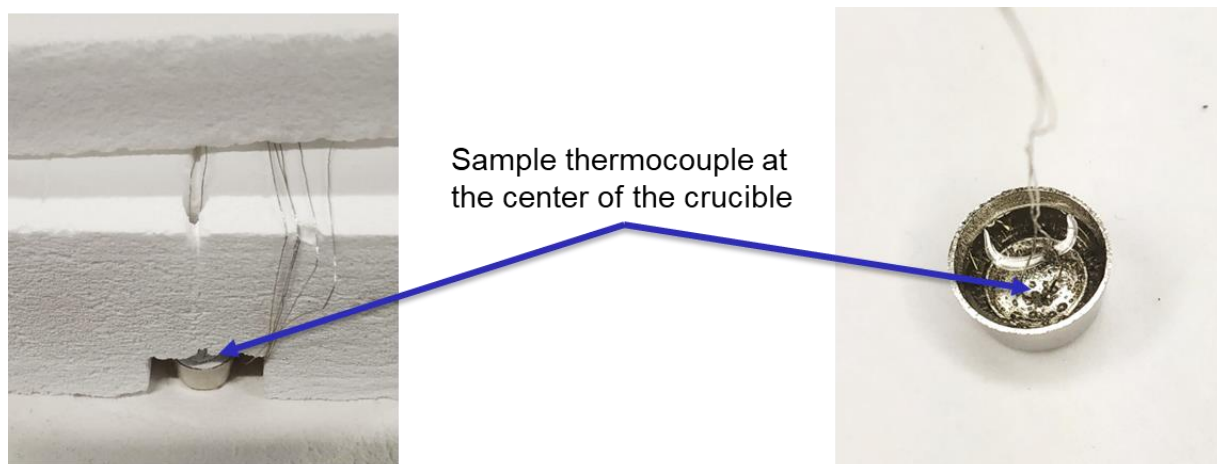


**Figure 15: Setup for thermocouple fixing at the center of CLSM crucible.**

### 3.2.1.2. Temperature measurement

The furnace thermocouple is situated a few mm below the slag-filled crucible which can cause differences in slag and furnace temperatures. The offset of both may change when the halogen bulb is replaced as it also depends on the filament position. Therefore, before starting the dissolution experiments, the relation between furnace and sample temperature was always investigated. The sample temperature was measured using an S-type thermocouple connected to a data logger. It was made of 0,127 mm diameter wires which were guided to the furnace opening through a corundum tube with two channels. The determined relation was adopted in the temperature program to actually achieve the desired slag temperature. **Figure 16** shows the temperature referencing results as an example.

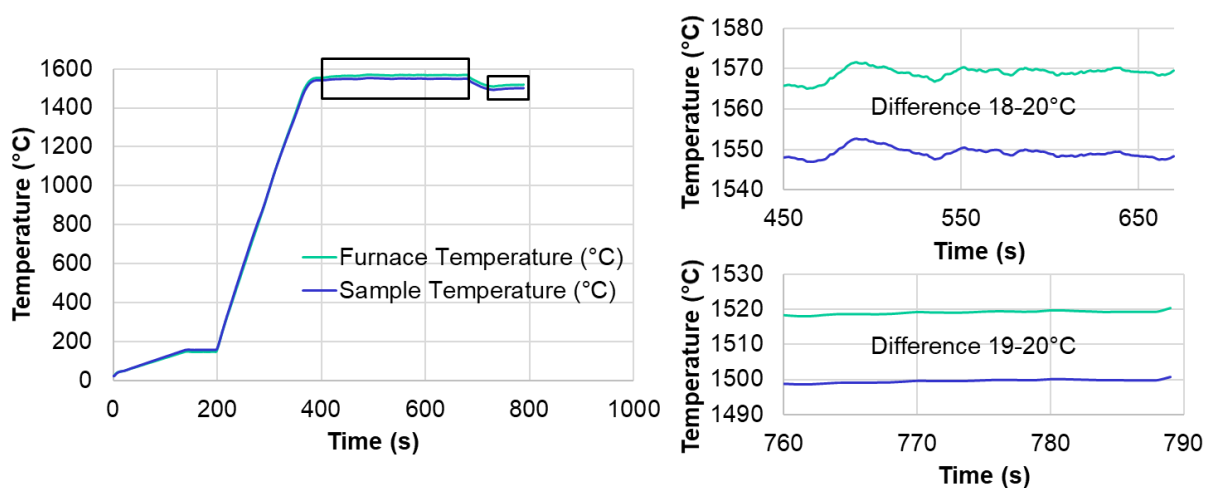


**Figure 16: Furnace and sample temperature referencing for HT-CLSM experiments.**

### 3.2.1.3. Dissolution experiments

The slag-filled Pt-Rh10 crucible is placed on a thin alumina plate which itself rests on the platinum sample holder plate. The particle is dropped at the center of the crucible with the help

of forceps at room temperature and the furnace lid is closed. The compressed air supply and water supply are turned on. Then the mirror furnace is heated according to the schedule. The heating rate is 50°C per min till 150°C and 1 min holding at 150°C to keep initially lower load on the halogen bulb, then 500°C per min till 50°C below the maximum temperature and the rest is heated at the rate of 100°C per min. The heating program is kept on hold just before reaching the experimental temperature and manually controlled to avoid overheating. Experimental temperature is maintained until the complete dissolution of the particle and then the furnace is cooled at the rate of 400°C per min. Video is captured starting at 150°C and including the whole dissolution process at experimental temperature. Particle tracking, focusing of camera and brightness adjustment are controlled manually. Experiments were carried out in ambient atmosphere. Several experiments were carried out at similar experimental conditions to check the repeatability and get an average result. The inner wall of the mirror furnace was cleaned after every experiment with ethanol-soaked cotton pads and flushed with compressed air.

### **3.2.2. Experimental procedure of CWTD**

#### **3.2.2.1. Slag preparation**

Slag was prepared using decarburized CaCO<sub>3</sub>, alumina powder, quartz powder and MgO powder. Slag batch preparation is identical to the CLSM experiments (3.2.1.1), only the quantity is higher for CWTD experiments. For each experiment, 580 g slag was molten in two steps in a platinum-10% rhodium (Pt-Rh10) crucible of 65 mm inner diameter and 100 mm height [91]. At first, around 380 g slag was pre-molten, and rest of the slag was molten during the CWTD experiment. The target slag bath height was around 70 mm without submerged sample and around 75 mm with sample.

#### **3.2.2.2. Corrosion experiment**

The slag-filled crucible is placed on a crucible holder in a high alumina safety crucible inside the furnace. Sample thermocouples are situated inside the crucible holder and position can be adjusted near to the crucible bottom for accurate sample temperature measurement. A cylindrical sample is fixed to the alumina rotor shaft using the Pt-Rh10 sample holder and the alumina bolts. Gap between sample bottom and crucible top edge is measured by lowering the sample till the crucible top edge. Clearance between crucible bottom and sample tip is calculated from this measured gap, the crucible height, the laser measurement position and the rotation position of the sample assembly. Initially, the clearance between crucible bottom and sample tip was set to 20 mm and this increases continuously with proceeding dissolution of sample [85], [91].

Experimental parameters can be individually chosen by a digital schedule with up to 10 steps for each experiment [85], [91]. Temperature, holding time, rotational speed of the sample, slag dropping time before laser measurement, gas purging (yes or no) and laser measurement (yes or no) can be defined for each step. Heating and cooling rates as well as the submersion temperature above which sample assembly goes down to rotation position are applicable for all steps. **Figure 17** shows an example of experimental parameters in digital schedule. Additionally, the lower position of the sample assembly i.e., rotation position and the upper rotor position for the laser measurement must be defined in the software. During the

experiment, values of all the experimental parameters are stored in a csv file and the saving frequency can be chosen between 1 and 10 per second [85], [91].

Rezept 3											
Aufheizsteigung [°C/Min.]	<input type="text" value="5"/>										
Abkühlwert [°C/Min.]	<input type="text" value="5"/>										
Eintauchtemperatur [°C]	<input type="text" value="1492"/>										
Rezeptschritt	1	2	3	4	5	6	7	8	9	10	
Sollwert [°C]	<input type="text" value="200"/>	<input type="text" value="1490"/>	<input type="text" value="1495"/>	<input type="text" value="1495"/>	<input type="text" value="1495"/>	<input type="text" value="1495"/>	<input type="text" value="1495"/>	<input type="text" value="1495"/>	<input type="text" value="1495"/>	<input type="text" value="1495"/>	
Haltezeit [Min.]	<input type="text" value="1"/>	<input type="text" value="30"/>	<input type="text" value="90"/>	<input type="text" value="90"/>	<input type="text" value="90"/>	<input type="text" value="90"/>	<input type="text" value="90"/>	<input type="text" value="90"/>	<input type="text" value="90"/>	<input type="text" value="90"/>	
Probenentnahme [0=Nein/1=Ja]	<input type="text" value="0"/>	<input type="text" value="0"/>	<input type="text" value="0"/>	<input type="text" value="0"/>	<input type="text" value="0"/>	<input type="text" value="0"/>	<input type="text" value="0"/>	<input type="text" value="0"/>	<input type="text" value="0"/>	<input type="text" value="0"/>	
Vermessung 3D [0=Nein/1=Ja]	<input type="text" value="1"/>	<input type="text" value="1"/>	<input type="text" value="1"/>	<input type="text" value="1"/>	<input type="text" value="1"/>	<input type="text" value="1"/>	<input type="text" value="1"/>	<input type="text" value="1"/>	<input type="text" value="1"/>	<input type="text" value="1"/>	
Abtropfdauer [Sek.]	<input type="text" value="60"/>	<input type="text" value="1800"/>	<input type="text" value="1800"/>	<input type="text" value="1800"/>	<input type="text" value="1800"/>	<input type="text" value="1800"/>	<input type="text" value="1800"/>	<input type="text" value="1800"/>	<input type="text" value="1800"/>	<input type="text" value="1800"/>	
Rotor [U/min.]	<input type="text" value="0"/>	<input type="text" value="0"/>	<input type="text" value="200"/>	<input type="text" value="200"/>	<input type="text" value="200"/>	<input type="text" value="200"/>	<input type="text" value="200"/>	<input type="text" value="200"/>	<input type="text" value="200"/>	<input type="text" value="200"/>	
Inertgas [0=Nein/1=Ja]	<input type="text" value="0"/>	<input type="text" value="0"/>	<input type="text" value="0"/>	<input type="text" value="0"/>	<input type="text" value="0"/>	<input type="text" value="0"/>	<input type="text" value="0"/>	<input type="text" value="0"/>	<input type="text" value="0"/>	<input type="text" value="0"/>	

Figure 17: Experimental parameters in the digital schedule.

The offset between the slag temperature and the furnace temperature was measured using S-type thermocouple immersed in the slag-filled crucible. From the temperature offset measurement, it was found that the slag temperature was 4–5°C higher at 1500°C and 1550°C where at 1450°C the difference was 9°C. These temperature differences were incorporated in the experimental heating schedules. Heating and cooling rate were defined to 5°C per min. Immersion temperature was set 3°C less than the experimental temperature. 30 min holding time was set at 5°C less than the target temperature to ensure homogeneous temperature distribution and complete as well as homogeneous melt formation. Corrosion time per step was defined dependent on the slag-refractory combination and the experimental temperature. Dynamic corrosion experiments were mainly carried out at 200 rpm. Some experiments also were conducted at 0 and 100 rpm to investigate the effect of the rotational speed on dissolution. After each corrosion step, the corroded sample was lifted and rested at measurement position for 30 minutes to allow the slag to drop down from the sample surface and then the laser device scanned the whole sample surface. The corrosion step and the sample scan cycle are repeated at the isothermal experimental temperature until the last step specified or until the test is terminated due to reasonably small sample diameter [85].

### 3.2.2.3. Slag drain out

After the experiment the slag quantity was in the range of 600 – 630 g which is not feasible to leach out with acid. The only feasible option to remove the slag from Pt-Rh10 is to drain it out at elevated temperature in a furnace. A setup for this was prepared in-house with self-flow high alumina castable. This setup consists of a holder to support the crucible in inclined condition, a refractory cup partially filled with bubble alumina to retain the slag and a safety crucible. **Figure 18** shows the slag drain out setup. The assembly with slag filled crucible was placed in a furnace and heated well above the liquidus temperature of the slag for 5 – 10 min.



Figure 18: Setup for slag drain out at elevated temperature; crucible before and after drain out.

### 3.3. Evaluation methods

Evaluation of the experimental results is the next important step. After CLSM experiments, videos are evaluated to receive the particle diameter over dissolution time. Processing of laser measurement data is carried out to receive the dissolution parameters from CWTD experiments.

#### 3.3.1. Evaluation methods for HT-CLSM experiments

##### 3.3.1.1. Evaluation of particle diameter over dissolution time

Videos of the CLSM dissolution experiments were analyzed with image processing software ImageJ. Time, furnace temperature and scale bar are available with every frame of the video. Scalein factor was defined by the scale bar of the video. A line was drawn through the boundary of the particle image to determine the area which was used to calculate the equivalent diameter of the dissolving particle and recorded in dependence of time. **Figure 19** shows an example for evaluation of CLSM video.



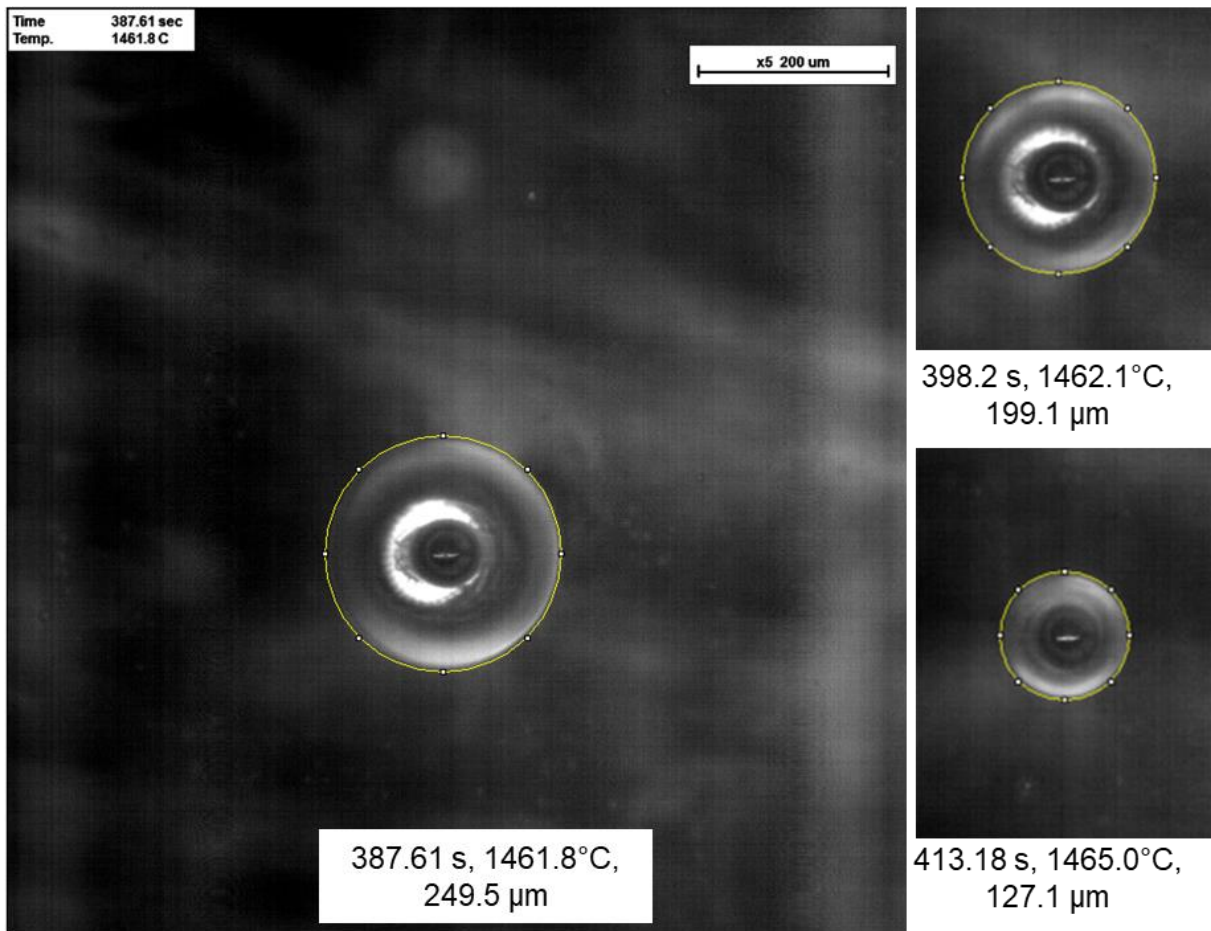


**Figure 19: Video frames at different time with the measurement line through the boundary of the particle.**

This measurement procedure was repeated in intervals from the beginning of isothermal experimental temperature till complete dissolution and produced the curve of equivalent diameter over dissolution time, hereafter referred to as dissolution curve. Diffusivity was determined using these data. As the measured initial particle diameters are not same in all experiments, a trend function was used to calculate the corresponding dissolution time of each experiment at the same initial diameter for comparison. **Figure 20** shows the measured equivalent diameter over dissolution time for the above-mentioned example.

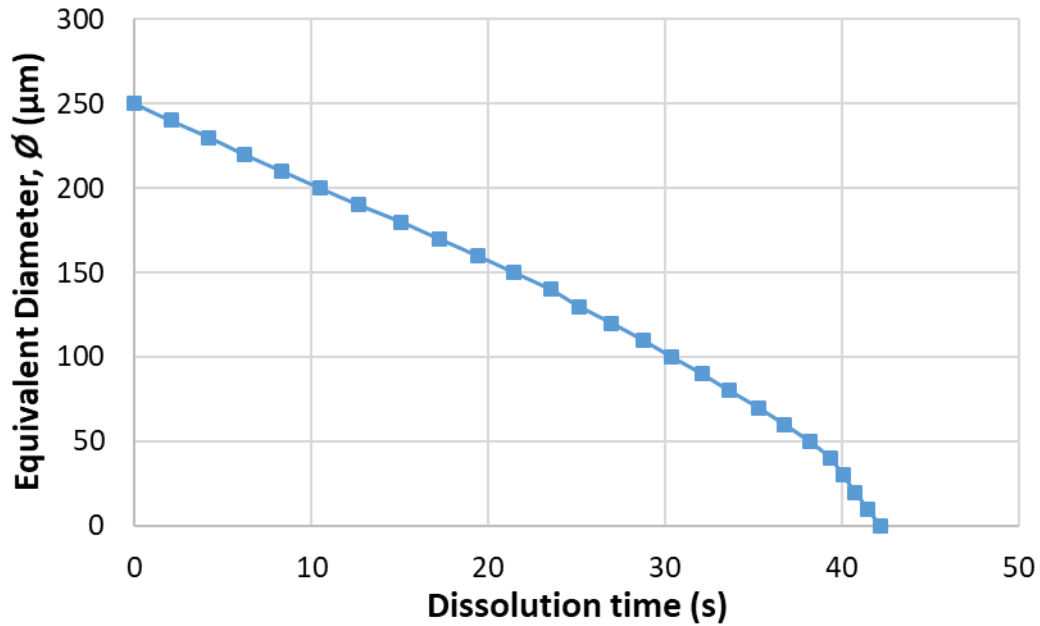


Figure 20: Equivalent diameters over dissolution time from CLSM experiment.

### 3.3.1.2. Evaluation of dissolution rate

After obtaining the equivalent diameters over dissolution time, third order polynomial regression was applied and the equation of the fitting curve was obtained. The first order derivative of the equation with respect to time was calculated to get the dissolution rate over the time. **Figure 21** shows an example of equivalent diameters over time with the polynomial fitting curve and dissolution rate over time. Dissolution rate was calculated for each experiment and the average of several experiments with similar experimental condition will be presented as representative dissolution rate. The equation of the fitting curve and first order derivative are also mentioned in the diagram.

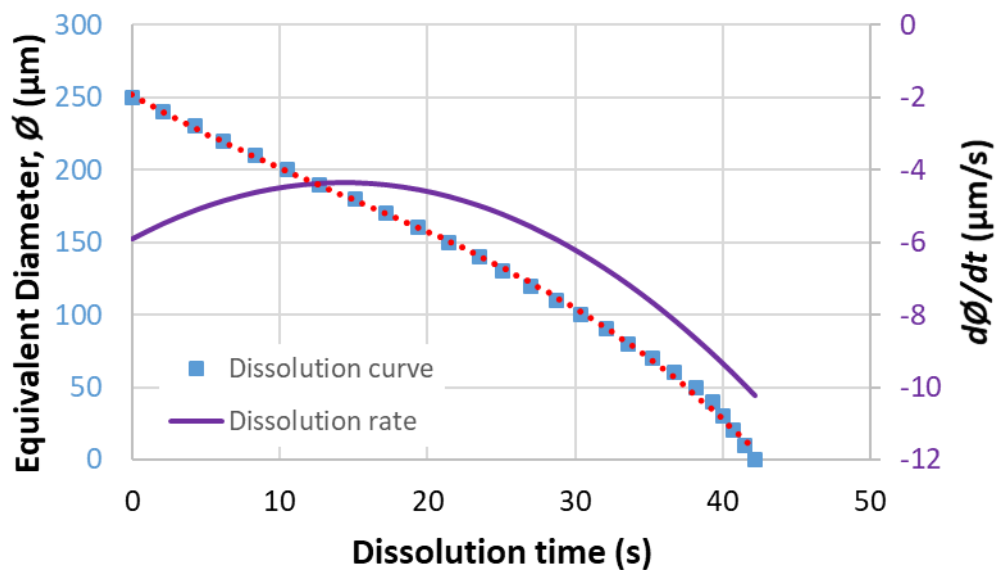


Figure 21: Dissolution rate over dissolution time from CLSM experiment.

### 3.3.1.3. Evaluation of diffusivity

Diffusivity was determined for each individual CLSM experiment using raw data of equivalent diameters over time and other experimental parameters with three different models. First one (M1), is the classical shrinking core model (SCM) for the boundary layer diffusion, and the equation (10) was applied to calculate diffusivity. Second one (M2), is also SCM, but including the convective part of mass flux and equation (15) was used. In these two cases, particle radius was considered as the effective boundary layer thickness. In the third case (M3), the equation (16) was used and the fitting parameters ( $D$  and  $K$ ) were determined, where the sum of the residual square is minimized.

### 3.3.2. Evaluation methods for CWTD experiments

Laser measurement data have to be evaluated to get the information about dissolution experiment. First, the 3D measurement was visualized to depict the sample geometry and then it was evaluated to obtain a representative continuous wear (CW) curve. The dissolution parameters can be extracted from this CW curve. All these details have been reported in the publication [85] which was prepared in course of this thesis work.

#### 3.3.2.1. 3D data visualization

After each laser measurement, the data are stored in video format and the 3D view and individual profiles can be visualized with the laser scanner software. For better visualization of the profile scanning, **Figure 22** a) shows the photograph of the sample, b) one profile line scanned by the laser device and c) the 3D view made out of all scanned profile lines. The width of the non-corroded sample part in 3D view corresponds to the initial circumferential length. This width is used as reference dimension. If the 3D view is observed from left to right, at the very left one can see the mantle surface of the alumina sleeve that safely locks the Pt/Rh-sample holder, then small part of alumina rotor and the Pt-Rh10 sample holder. Afterwards, the mantle surface of the corroded cylinder specimen can be seen where the left part of the mantle surface is un-corroded and the right part is corroded. 2 cm below the upper edge of the cylinder specimen, both ends of an alumina fixing bolt are visible, which fixes the cylinder sample to the sample holder. At the very right of the 3D view, Pt-Rh10 crucible top edge is visible. In this 3D view a low amount of laser scattering (artifacts) is observed and the measurement represents the shape of the worn specimen very well. The reduction in diameter and the slightly larger diameter in the middle of the slag-corroded part are clearly visible [85].

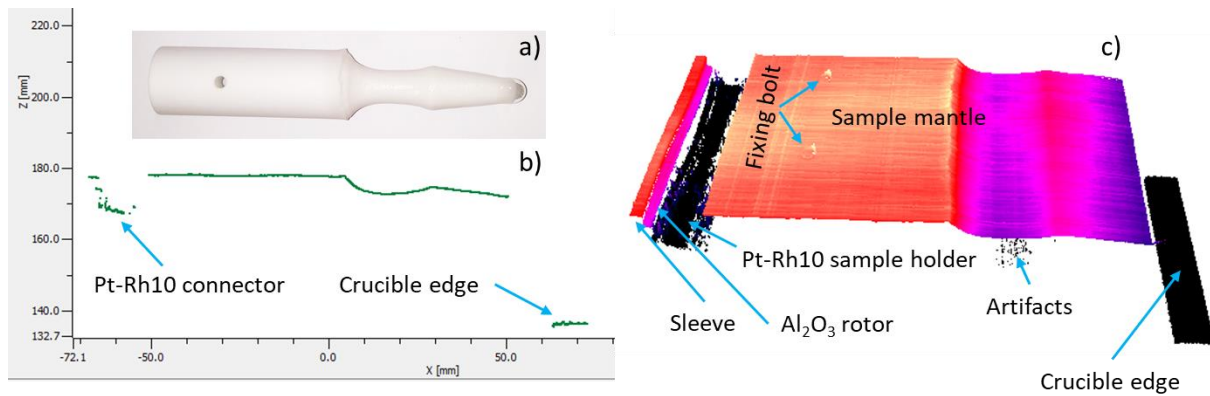


**Figure 22: Profile line scanning of a corroded Al<sub>2</sub>O<sub>3</sub> fine ceramic sample surface at 1500°C. a) Photograph of the same corroded sample at room temperature, b) line scan of a single profile and c) 3D view made out of all scanned profile lines.**

### 3.3.2.2. Mean value curves

3000 (or more usually 2974 profiles) profiles of laser measurement construct the 3D view, and each profile contains the dimension information for a particular azimuth [85]. It is unfeasible to analyze each individual profile to receive the dimension information. The corroded sample is not exactly uniform in circumferential direction which necessitates calculation of a mean interface profile. Furthermore, the sample axis may deviate slightly from the axis of rotation. The rotating body thus depicts a cone of very small, apex angle with the lower end showing the greatest deflection. During a laser measurement of 360°, the individual profiles of the corroding body may be slightly inclined with a positive or negative angle to the theoretical rotation axis [85]. To explain this, an example of static corrosion experiment of alumina ceramic is considered here. Two sample profiles of the static experiment are shown in **Figure 23** [85]. The dotted line shows minor inclination towards the laser scanner (8  $\mu\text{m}/\text{mm}$ ) of a single profile (1). Therefore, the lowest point of the sample surface is displaced by an additional 0.8 mm from the dashed-dotted theoretical axis of rotation [85]. For this reason and because of laser scattering from diffuse reflection of slag-covered areas at high temperature, a single corrosion profile is not representative for the entire sample surface. To ensure reliable results for corrosion or erosion measurements, mean value curves (2) are calculated from raw data of all profiles, resulting in a perfectly aligned axis of rotation and leveling out of erroneous values. Nevertheless, mean value curves calculated from the raw data show a different trend at the top end of the cylinder specimen as they do not end straight. The laser scanner detects either the Pt/Rh-sample holder or the sample surface at the top edge, causing the profile to shift towards the rotation axis. Because of this slope and to minimize the influence of artifacts on mean values, the raw data for mean value curves must be pre-processed [85].

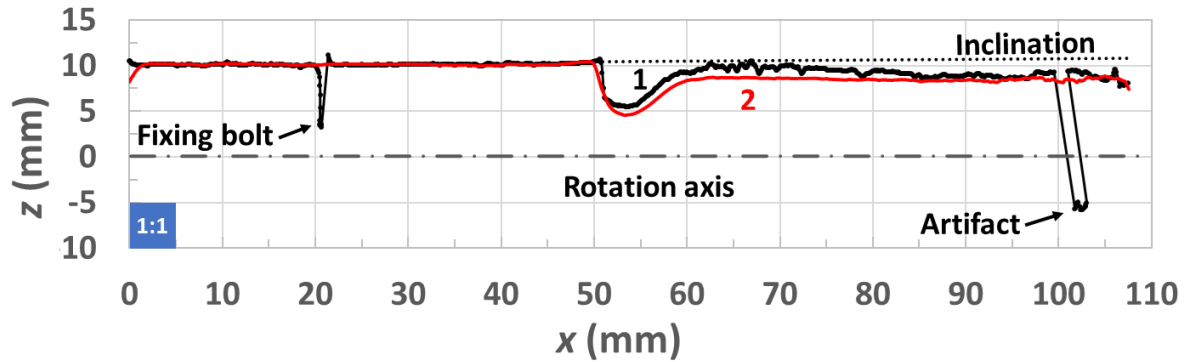


Figure 23: Representation of a corroded alumina fine ceramic cylinder specimen as single corrosion profile (1) and as mean value curve (2) [85].

### 3.3.2.3. Identification and elimination of artifacts

During continuous wear measurements of dissolution experiments in slags, artifacts occur primarily when the laser measures through a slag layer that exceeds a certain thickness, but minor scattering could also be found at sharp edges. Therefore, laser scattering is observed mainly at slag-filled pores and at the bottom tip of the ceramic cylinder, where a slag droplet forms during slag dropping time and this affects the measurement. The method of identification and elimination of artifacts is reported in [85].

If artifacts are located far enough from the surface, like the artifact in **Figure 23** [85], it is easily possible to distinguish them by a maximum or minimum  $z$ -value from evaluable information. It was found that in the regions with a scatter in  $z$ -direction also errors in  $x$  direction can be observed but are by far smaller [85]. Data received after erasing of obvious artifacts are called cleansed raw data here. Due to this procedure no profiles but single data points only are removed. For not obvious artifacts, i.e. those closer to the sample surface, a different procedure is performed with the cleansed raw data. In the following, the measurement position is defined by the subscripts  $i,j$  for the  $i$ -th point on the  $j$ -th profile. Approximately 1100 points are measured on any of 2974 profiles representing one revolution. A value  $z_{i,j}$  or  $x_{i,j}$  of the cleansed raw data is considered as evaluable information for a mean value curve if it follows the restrictions of equation (25) or equation (26), respectively.  $\mu_{z,i}$  and  $\mu_{x,i}$  are the mean  $z$  and  $x$  values of all profiles from the cleansed raw data at the position  $i$ , respectively.  $\sigma_{z,i,\infty}$  and  $\sigma_{x,i,\infty}$  are the associated standard deviations of the cleansed raw data of  $z_i$  and  $x_i$ , respectively. In the following conditions  $\varepsilon$  is a constant to be determined that defines possible outliers which have to be neglected for further evaluation:

$$\mu_{z,i} - \varepsilon \cdot \sigma_{z,i,\infty} \leq z_{i,j} \leq \mu_{z,i} + \varepsilon \cdot \sigma_{z,i,\infty} \quad (25)$$

$$\mu_{x,i} - \varepsilon \cdot \sigma_{x,i,\infty} \leq x_{i,j} \leq \mu_{x,i} + \varepsilon \cdot \sigma_{x,i,\infty} \quad (26)$$

The refined data set comprises all measurements satisfying these conditions [85]. The most justified  $\varepsilon$  value is determined by comparison of results received for different choices where

the unwanted artifact are eliminated with minimum loss of data points. Due to the indicated conditions, the number of  $z_{i,j}$  and  $x_{i,j}$  values in the refined data sets decreases. For given  $\varepsilon$ , a higher percentage of  $z_{i,j}$  values fails to fulfil condition (equation (25)) than  $x_{i,j}$  values violate condition (equation (26)). Nevertheless, an  $x_{i,j}$  value associated with a  $z_{i,j}$  value not satisfying (equation (25)) is also erased for the sake of data consistency. The standard deviations calculated from the refined data set are denominated by  $\sigma_{z,i,\varepsilon}$  and  $\sigma_{x,i,\varepsilon}$  [85].

**Figure 24** a) shows the 3D view of in-situ laser measurement of the static corroded alumina sample and **Figure 24** b) the standard deviations along  $\mu_{x,i}$  [85]. It is clear that the highest deviations can be found at the top, at the onset of the corrosion groove and at the corroded lower part of the sample where more laser scattering occurred. The benefit of outlier removal from the raw data can be seen from **Figure 24** b) by comparing the standard deviations of  $z$  for pure raw data  $\sigma_{z,i,raw}$  and cleansed raw data  $\sigma_{z,i,\infty}$  [85]. Furthermore, it can be seen from the diagram that the standard deviations from the refined data  $\sigma_{z,i,\varepsilon}$  decrease with decreasing  $\varepsilon$ . The evaluation of the cleansed raw data with  $\varepsilon = 2.25$  smoothed the standard deviation of the upper sample edge, the artifacts of the alumina bolt ( $\mu_{x,i} = 20$  mm) and the lower sample part from 100 to 105 mm without distorting the sample geometry. The standard deviation in  $x$ -direction is low and increases only at the top of the cylinder specimen due to slight misalignment between rotation and specimen axis and maybe scattering at the sharp edge [85].

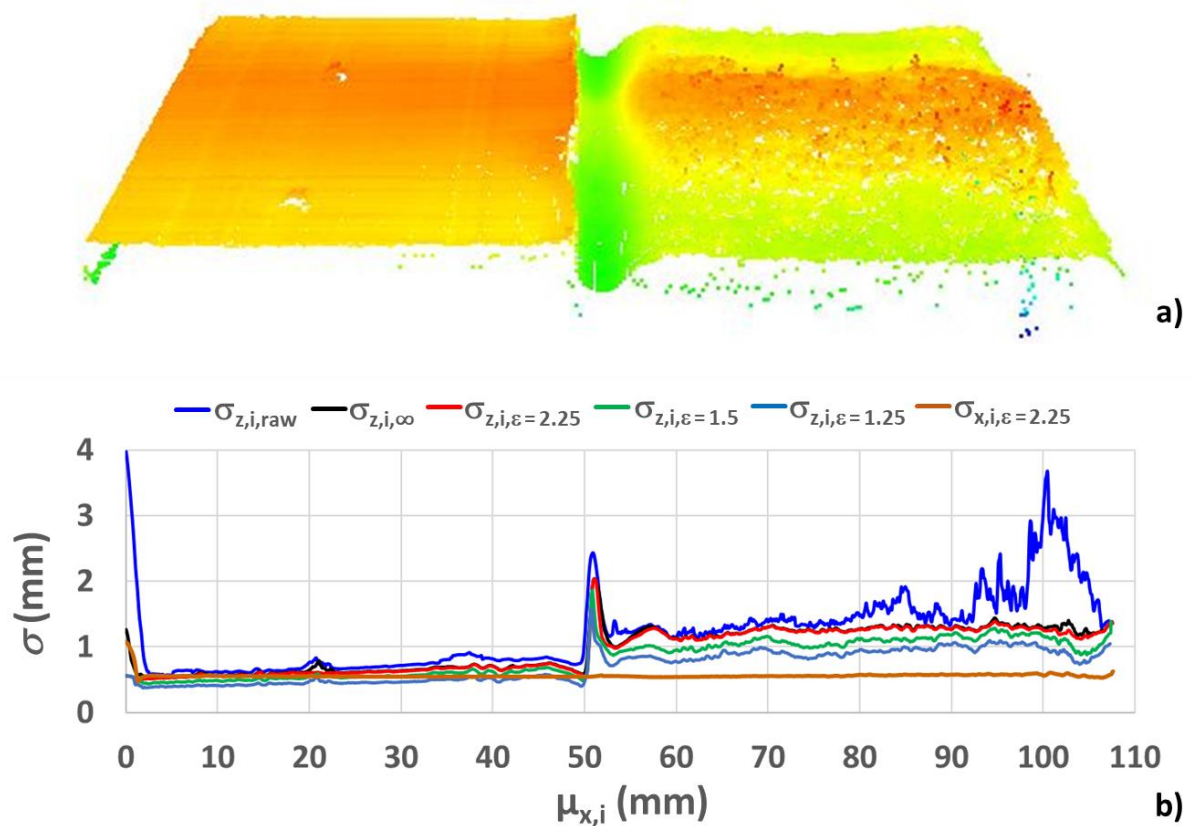


**Figure 24:** Static corroded alumina sample as a) visualized in situ 3D laser measurement [39] and b) diagram of standard deviations of profiles in dependence of  $\mu_{x,i}$  [85].

The dimensions of the static cylinder sample were measured manually with a vernier caliper as post mortem analysis and the thermal expansion was considered for comparison with the high temperature laser measurement [85]. In **Figure 25 a)**, the differences  $\Delta r$  received by subtracting hand gauged radii from measurements of the laser scanning device are represented. For the latter the following options have been chosen: The radii calculated from mean cleansed raw data  $\bar{r}_{i,\infty}$ , the radii of a single profile of the cleansed raw data set  $r_{i,\infty}$  as well as radii calculated from refined mean value curves  $\bar{r}_{i,\varepsilon}$ . For the dotted linear trend line of the single profile (black),  $\Delta r$  at 20 mm (fixing bolt) was not considered to show that the trend line mirrors the inclination of the specimen at the measurement position, while the trend line for  $\bar{r}_{i,\varepsilon=2.25}$  shows a perfect alignment with the x-axis. For the latter curve  $\Delta r$  is well distributed over the whole sample length. Lower  $\varepsilon$  values seem to partly underestimate the cylinder radius, while results for values up to 3 are not depicted here because they do not differ significantly from those for 2.25 [85].

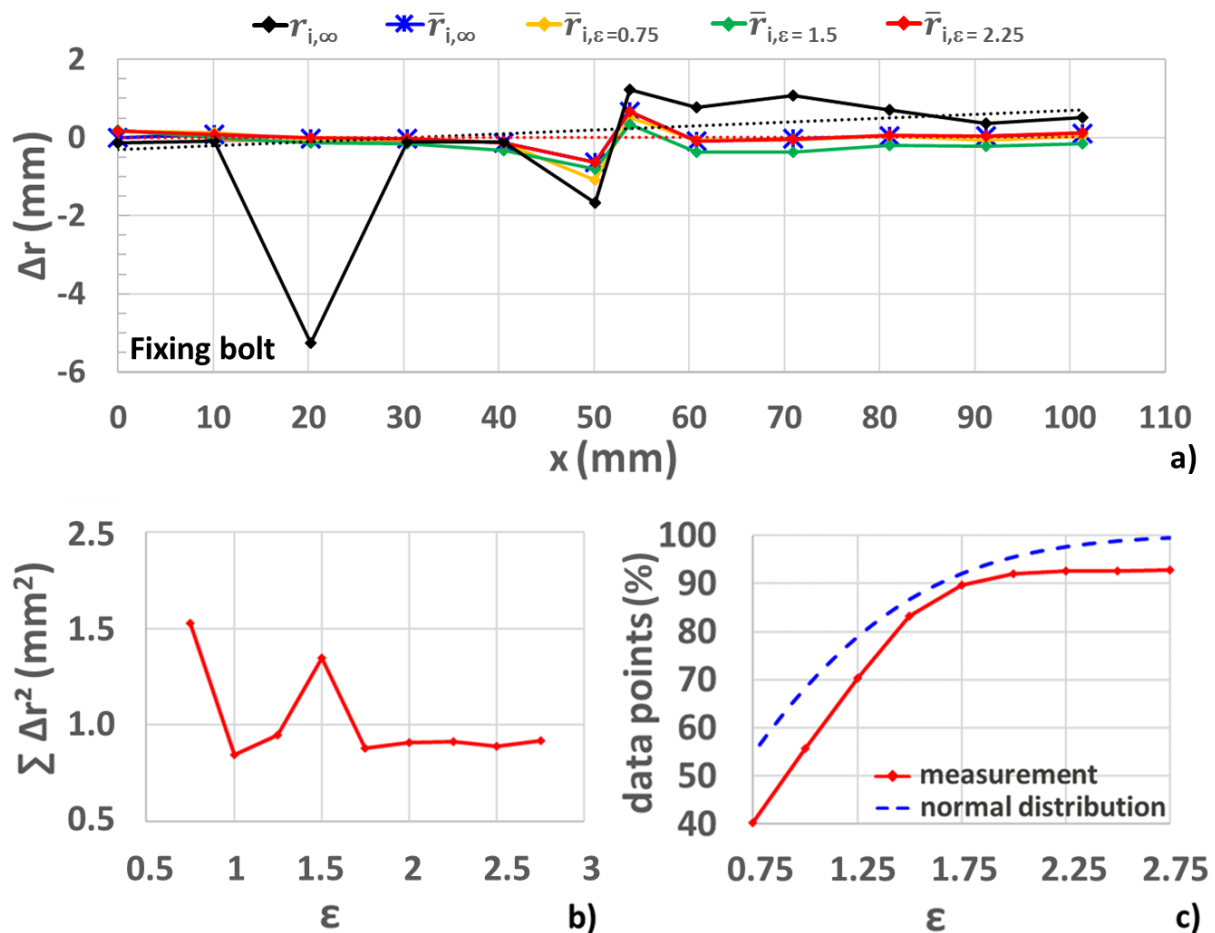


**Figure 25: Diagrams of 3D measurement raw data evaluation of corroded  $\text{Al}_2\text{O}_3$  fine ceramic cylinder. a) Radius difference  $\Delta r$ , from hand measured radii to radii from cleansed raw data and refined data over x-axis. b)  $\Sigma \Delta r^2$  plotted against  $\varepsilon$  and c) percentage of data points after evaluation, plotted against  $\varepsilon$  [85].**

For a suitable choice of  $\varepsilon$ ,  $\Sigma \Delta r^2$  (**Figure 25 b)**) as well as the percentage of data points after evaluation with different  $\varepsilon$  (**Figure 25 c)**) have to be considered. **Figure 25 b)** follows from **Figure 25 a)**. All  $\Delta r$  (refined data) are squared and summed for the 12 radii at the corresponding x-axis positions.  $\Sigma \Delta r^2$  is higher for  $\varepsilon < 1.75$  with exception of  $\varepsilon = 1$  where  $\Sigma \Delta r^2$  is similar to

higher  $\varepsilon$  values. For  $2 \leq \varepsilon \leq 2.75$   $\Sigma \Delta r^2$  remains constant in the range of  $0.91 \pm 0.01 \text{ mm}^2$ . This constant behavior for  $2 \leq \varepsilon \leq 2.75$  also shows the percentage of remaining data points in **Figure 25 c)**. The percentage of data points increases with increasing  $\varepsilon$ . Around  $\varepsilon = 1.75$  the curve flattens and remains stable for  $2.25 \leq \varepsilon \leq 2.75$  with a mean data point amount of  $92.64 \pm 0.12\%$ . As **Figure 25 c)** also shows the percentage of data points of refined data (solid curve) is somewhat smaller than would be expected from a normal distribution (dashed curve); this means that the cleansed raw data are not normally distributed with good accuracy [85].

A high percentage of remaining data points and an accurate identification and erasure of artifacts shows that the evaluation of CWTD 3D laser measurements with equations (25) and (26) and  $\varepsilon = 2.25$  is reasonable. Mean value curves refined in this way are hereafter referred to as CW curves, where CW stands for continuous wear [85]. The intersection point of the initial curve of the un-corroded sample and the actual CW curve defines the onset for the corroded part. The immersion length is defined from the sample tip to the onset of the corroded part [85].

#### 3.3.2.4. Accuracy of the laser measurement

Resolution along the sample length depends on the specification of the laser device (resolution and angle of the laser beam) and distance between sample and laser device. Whereas, the resolution along circumferential direction depends on the scan rate, sample diameter and rotational speed during laser measurement. In case of present setup of CWTD, the laser scanner projects a line with a vertical angle of  $21.4^\circ$ . The cylindrical sample is situated at a distance of 325 mm from the laser device and the laser line extends along the height of the sample. The laser scanner provides 1280 measurement points ( $i$ ) per profile and as the sample is situated to close to allow for the maximum measurement range around 1070 points per profile are sampled from the surface of a 110 mm long specimen, resulting in a resolution of  $100 \mu\text{m}$  along the sample height ( $x$ -axis). In circumferential direction ( $y$ -axis) a higher resolution of  $20 \mu\text{m}$  could be achieved for cylinder specimens with 20 mm diameter, due to a high scan rate of 100 per second and rotational speed of 2 rpm during laser measurement [85]. To assess the accuracy of the laser measurement, a cylindrical polymer sample was produced with a lathe and the dimensions were measured manually with a caliper (mean of three measurements) and by laser device in CWTD. **Figure 26** [85] compares the sample dimensions of a) the visualized 3D data from the laser measurement in front view and the profile with b) the hand gauged dimensions. Actual dimensions can be extracted from the CW curve of the laser measurement. In the visualized laser measurement, the depth information in  $z$ -direction is colored. The compared sample dimensions are in good agreement, since the mean difference between the five manually measured mean radii and those calculated from CW curve (average of 3000 profiles) was  $111 \mu\text{m}$ . The mean calculated sample height differed only by  $20 \mu\text{m}$  [85].



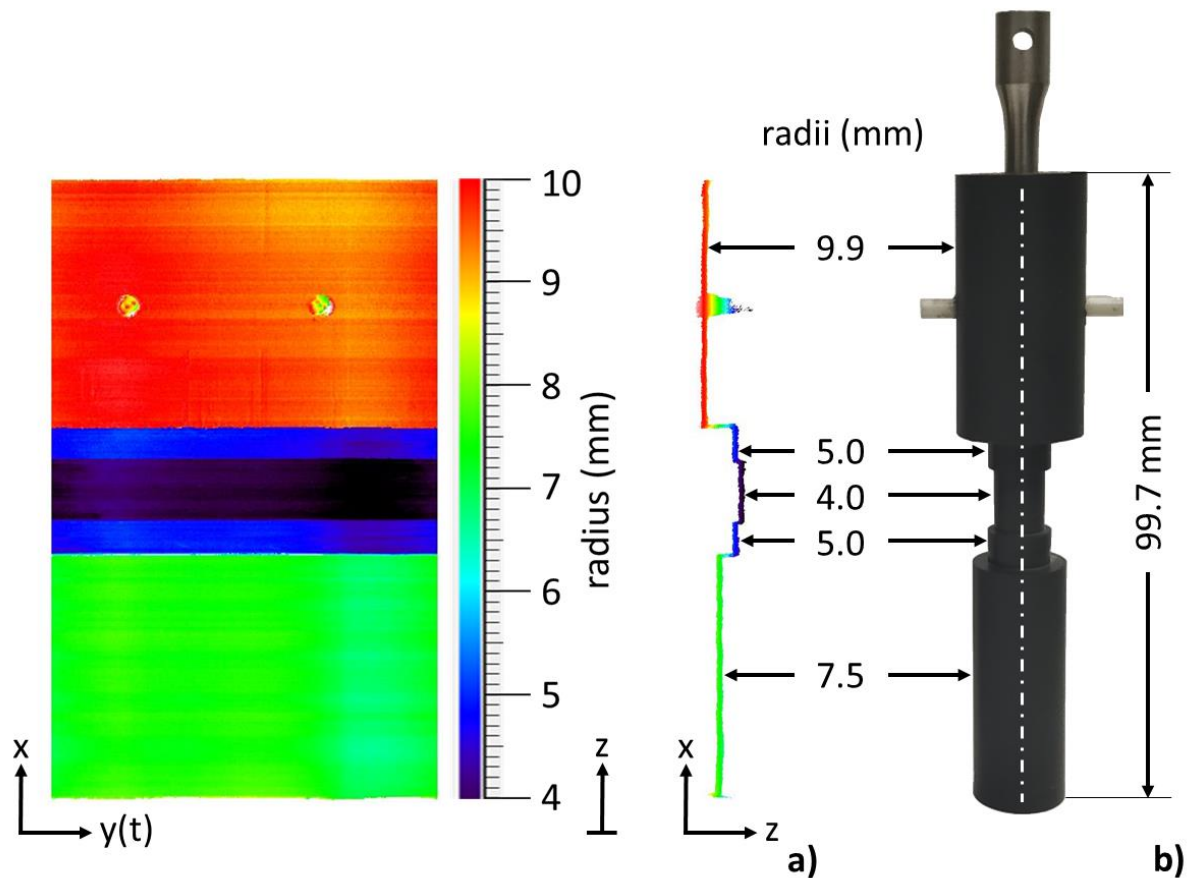


Figure 26: Cylindrical polymer sample as a) visualized 3D laser measurement and b) photograph [85].

### 3.3.2.5. Evaluation of diffusivity

In the present work, dissolution of alumina and magnesia fine ceramics have been studied in silicate slags. It is evident from many references that the dissolution of alumina and magnesia in molten slag is controlled by the diffusion through a boundary layer [6]–[13], [16], [17], [55], [92], [93]. The most important aim of this work is the determination of the effective binary diffusion coefficient, this being necessary to quantify the dissolution process. While simulation of diffusion by CFD methods is promising with respect to include realistic boundary conditions and to consider the actual fluid flow, it is hindered by the high Schmidt numbers of slags which would necessitate an inefficiently fine spatial resolution. This could be overcome by a combination of computational fluid dynamics (CFD) with an asymptotic boundary layer approach. Guarco et al. has reported this technique for the case of laminar flow and used alumina dissolution in silicate slag as an example to describe the method [28]. Diffusivities for dynamic corrosion experiments have been determined in this work.

To quantify the dissolution process, it is important to know the flow field around the dissolving body. In the already quoted reference [28], the flow field was resolved with CFD simulations and the volume of fluid (VOF) multiphase approach was employed for the resolution of slag and atmosphere phases. In the current system of interest, effects of surface tension cannot be neglected and these are incorporated with the continuous surface force (CSF) model. The

employed model was laminar, 2D and axisymmetric, what was supported by the experimental range of Reynolds number. The flow regimen was characterized by the Taylor number, which gives the ratio of the centrifugal to the viscous forces. In annular set-ups with rotating cylinders, centrifugal instabilities are known to develop after a critical Taylor number is exceeded [28]. The first appearing regimen is known as the Taylor-Couette regime, which was described by Taylor [94]. Taylor numbers for the current experimental setup are far lower than the critical one and this confirms the absence of such instabilities.

Guarco et al. [28] conducted simulation for the third corrosion step of a dissolution experiment performed with above described CWTD where the shape of the corroded sample significantly deviates from a perfect cylindrical surface. The specimen shape resulted from the CW curve and was smoothed for CFD model. The sample tip was complemented with arbitrary curvature. The CFD simulations were employed exclusively for the resolution of the flow field. The transport equations for the species were not solved within the CFD model [28]. It was treated by a post-processing step using an approach based on the boundary layer theory. This methodology accounts for the advection that occurs in an orthogonal direction to the solute/solvent interface due to Stefan flow and the effect of this Stefan flow on the boundary layer thickness. Mass transfer coefficients  $\beta_{tot}$  were calculated using equation (27) [28].

$$\beta_{tot} = \frac{\chi_D}{1 - w_s} \cdot \frac{D \cdot Sh_0}{L} \quad (27)$$

Here,  $w_s$  is the alumina saturation mass fraction,  $D$  the effective diffusivity,  $L$  the characteristic length (gap width,  $d$  and tip radius,  $R_t$  for mantle surface and bottom surface respectively),  $Sh_0$  the Sherwood number without considering the influence of the interface advection on the boundary layer thickness and  $\chi_D$  is a correction factor for this effect.  $Sh_0$  was calculated according to equation (28) [28].

$$Sh_0(x) = \frac{L \cdot Sc^{\frac{1}{3}}}{9^{\frac{1}{3}} \cdot \nu^{\frac{1}{3}} \cdot \Gamma\left(\frac{4}{3}\right)} \cdot \sqrt{R \cdot \alpha(x)} \cdot \left[ \int_{\ell} R \cdot \sqrt{R \cdot \alpha(\zeta)} \cdot ds \right]^{-\frac{1}{3}} \quad (28)$$

Here,  $x$  is the local coordinate along the worn profile,  $\Gamma$  the gamma function,  $\alpha$  is a directional derivative of the velocity that is tangential to the surface in the direction normal to it, and  $R$  the radius of the revolution surface at position  $x$ . The last two variables vary along the profile, unlike the case of the mantle of an ideal cylindrical surface where only  $\alpha$  is a function of the coordinates. This line integral is evaluated numerically with the trapezoidal rule. Variable  $\alpha$  was calculated with equation (29) and the wall shear stresses were defined by equation (30) [28]. The axial wall shear stress  $\tau_z$  considers the derivative of the axial velocity in the direction normal to the surface. In addition, the radial wall shear stress  $\tau_r$  considers the derivative of the radial velocity in the normal direction.  $t_z$  and  $t_r$  are the components of tangential vector [28].

$$\alpha = \frac{\partial v_t}{\partial \hat{n}} = \frac{\partial(\hat{v} \cdot \hat{t})}{\partial \hat{n}} = \frac{\partial \hat{v}}{\partial \hat{n}} \cdot \hat{t} = \frac{1}{\mu} (\tau_z t_z + \tau_r t_r) \quad (29)$$

$$\tau_{w,a} = \mu \frac{\partial v_a}{\partial \hat{n}}; \quad a = z, r \quad (30)$$

This method allows the calculation of local, steady-state mass transfer coefficients. The obtained mass transfer coefficient profile is employed for the computation of the wear rate, which is used to predict the end worn profile and the prediction was validated with experimental results. Furthermore, the model is employed to calculate the diffusivities by using two different approaches [28].

In the first approach, the experimental average mass flux density  $j_{exp}$  was applied to determine the diffusivity value that results in the same simulated mass flux density  $j_{model}$ . The average experimental mass flux density and other parameters were calculated as per **Table 2**. The average simulated mass flux density for the model was computed from the area weighted average between the mantle ( $m$ ) and the tip ( $b$ ). The former was calculated from  $Sh_0 \cdot Sc^{-1/3}$  over corroded sample length data and the latter was calculated by using Levich equation. This results in the equation (31) [28].

$$j_{model} = \beta_{tot} \cdot \Delta c = \frac{1}{A_m + A_b} \cdot (A_m \cdot \beta_m + A_b \cdot \beta_b) \cdot \Delta c \quad (31)$$

The mass transfer coefficient  $\beta_{tot}$  was calculated from equation (27) together with the identity

$$j_{tot} = \beta_{tot} \cdot \rho^s \cdot (w_s - w_0)$$

what gives:

$$D^{\frac{2}{3}} = \frac{j_{tot} \cdot L}{\chi_D \cdot B \cdot \rho^s \cdot G \cdot \nu^{1/3}} \quad (32)$$

$$B = \frac{w_s - w_0}{1 - w_s} \quad (33)$$

Here,  $j_{tot}$  is the total experimentally determined mass flux density,  $B$  is the dimensionless concentration difference;  $\rho^s$  and  $\nu$  are the slag density and viscosity respectively,  $L$  the characteristic length. The quantity  $G = Sh_0 \cdot Sc^{-1/3}$  uses equation (28) and the Levich equation applying an area weighted average of the bottom and mantle contributions.  $Sh_0$  from the bottom of the sample was modified by multiplying it with  $d/R_t$  so it uses the same characteristic length,  $L = d$ , as the mantle and this was substituted in equation (32) [28].

The second approach was based on the good agreement between the measured and simulated sample profiles for the end of that particular corrosion step. A least-squares problem was formulated in which the diffusivity is the design variable. The advantage of this method is that no assumptions are needed for the mass flux from the tip of the sample. This is because only focus was on fitting of the predicted simulation profile to the laser measurement at the end of that particular step. The minimization problem was solved by using MATLAB and yields the global minimum [28].

Though the method reported by Guarco et al. [28] produces reliable diffusivity results as it considers flow field around the actual sample geometry of that particular step, its application takes much effort. Trustworthy diffusivity can be determined if reliably mass transfer equations are available and mass flux has been determined experimentally. In this work, diffusivities have been calculated by the method according to Guarco et al. [28] for some corrosion steps of different experiments. Additionally to this, diffusivities for all corrosion steps of all dynamic corrosion experiments have been determined from total mass flux density using modified Sherwood relation translated from Nusselt correlation reported by Tachibana and Fukui [27] for the mantle and Sherwood relation reported by Levich [22] for the bottom of the sample. All the corrosion parameters required for diffusivity calculation change with dissolution time within the corrosion step, so it is wise to evaluate the diffusivity at the middle of the corrosion step which will be representative for that particular interval. The parameters are defined in **Table 2**. Before dipping the sample into the slag its surface is scanned yielding the initial profile at  $t_0$ . Profiles are measured at time steps  $t_c, 1 \leq c \leq m$ , where  $m$  is the number of laser scans performed additional to the first one at  $t_0$ . Corrosion step between laser measurements at  $t_{c-1}$  and  $t_c$ , can also be denominated as  $c$ . This diffusivity determination procedure using mass transfer equations has been reported in [91] and is exemplified below.

**Table 2: Definition of parameters required to evaluate diffusivity for the interval ( $t_{c-1}$ ,  $t_c$ ) [91].**

Quantity	Measured at	Evaluation at
	$t_c$	$(t_c + t_{c-1})/2$
Refractory volume	$V_c^r$	$V_{c-\frac{1}{2}}^r = \frac{V_c^r + V_{c-1}^r}{2}$
Volume loss relative to initial volume	$\Delta V_c^r = V_0^r - V_c^r$	$\Delta V_{c-\frac{1}{2}}^r = V_0^r - V_{c-\frac{1}{2}}^r$
Mass loss relative to initial mass	$\Delta m_c^r = \rho^r \cdot \Delta V_c^r$	$\Delta m_{c-\frac{1}{2}}^r = \rho^r \cdot \Delta V_{c-\frac{1}{2}}^r$
Bulk concentration of species $i$ in slag		$c_{0,i,c-\frac{1}{2}}^s = \frac{c_{0,i,0}^s V_0^s + \Delta m_{c-\frac{1}{2}}^r w_k^r}{V_{c-\frac{1}{2}}^s} = \frac{c_{0,i,0}^s V_0^s + \Delta m_{c-\frac{1}{2}}^r w_i^r}{m_0^s + \Delta m_{c-\frac{1}{2}}^r} \rho^s$ $w_{0,i,c-\frac{1}{2}}^s = \frac{c_{0,i,0}^s V_0^s + \Delta m_{c-\frac{1}{2}}^r w_i^r}{m_0^s + \Delta m_{c-\frac{1}{2}}^r}$
Dimension less concentration difference		$B_{c-\frac{1}{2}} = \frac{w_s^s - w_{0,c-\frac{1}{2}}^s}{1 - w_s^s}$
Viscosity		$\eta = \eta(w_{0,i,c-\frac{1}{2}})$
Immersion specimen length	$l_c$	$l_{c-\frac{1}{2}} = \frac{l_c + l_{c-1}}{2}$
Specimen effective radius	$R_{1,c}$	$R_{1,c-\frac{1}{2}} = \sqrt{\frac{V_{c-\frac{1}{2}}}{\pi l_{c-\frac{1}{2}}}}$
Submerged surface area	$A_c = A_{m,c} + A_{b,c}$	$A_{c-\frac{1}{2}} = \frac{A_c + A_{c-1}}{2}$
Mass flux density		$j_{c-\frac{1}{2}} = \frac{\Delta m_c^r - \Delta m_{c-1}^r}{A_{c-\frac{1}{2}}(t_c - t_{c-1})}$

From equation (27) the below quoted equation (34) follows which represents the total mass flux density including diffusion, convection, and the influence of Stefan flow on the fluid flow field [91].

$$j = \chi_D \frac{D}{L} \frac{1}{1 - w_s} Sh_0 \cdot \Delta c \quad (34)$$

Here,  $j$  is the mass flux density,  $D$  the effective binary diffusivity,  $L$  a characteristic length,  $w_s$  the mass fraction of dissolving species in the saturated slag,  $Sh$  the Sherwood number and  $\Delta c$  the concentration difference. The quantities used in equation (34) are defined in equations (35), (36), and (37) [91].

$$Sh_{(0)} = \frac{\beta_{(0)}L}{D} = Sh_{(0)}(Re, Sc, \Gamma) \quad (35)$$

$$Sh_0 = Sh(B = 0); \quad \beta = \frac{D}{\delta}; \quad \beta_0 = \beta(B = 0) \quad (36)$$

$$\chi_D = \chi_D(B, Sc) = \frac{Sh}{Sh_0} \quad (37)$$

Here,  $w_0$  the mass fraction of dissolving species in the slag bulk,  $Re$  the Reynolds number,  $Sc$  the Schmidt number,  $\Gamma$  the ratio of gap width of annuli to cylinder radius,  $\delta$  the effective diffusive boundary layer thickness and  $\beta$  is the mass transfer coefficient [91].

For high  $Sc$  numbers the quantity  $\chi_D$  can be approximated by a linear expansion in  $B$ :

$$\chi_D = \frac{Sh}{Sh(B = 0)} = \chi_D \approx \frac{1}{1 + 0.5666B} \quad (38)$$

Tachibana et al. reported different empirical equations for heat transfer in different setups [27]. Heat transfer in annuli with a rotating inner cylinder is similar to the dynamic finger test for dissolution with exception of the bottom gap. Equation (39) is the Sherwood relation transformed from the Nusselt relation for aforesaid arrangement [91].

$$Sh = \frac{\beta \cdot (R_2 - R_1)}{D} = 0.21 \cdot (Ta^2 \cdot Sc)^{\frac{1}{4}} = 0.21 \cdot Re^{\frac{1}{2}} \cdot Sc^{\frac{1}{4}} \cdot \left(\frac{R_2 - R_1}{R_1}\right)^{\frac{1}{4}}; \quad Ta \leq 10^4 \quad (39)$$

$$\text{with } Ta = \frac{\omega \cdot R_1^{\frac{1}{2}} \cdot (R_2 - R_1)^{\frac{3}{2}}}{\nu} \text{ and } Re = \frac{\omega \cdot R_1 \cdot (R_2 - R_1)}{\nu}$$

Here,  $R_1$  is the mean cylinder radius,  $R_2$  is the crucible radius,  $Ta$  the Taylor number,  $\omega$  the angular velocity of the rotating cylinder and  $\nu$  is the kinematic viscosity of the melt.

According to Guarco et al. [28] modification of exponent of  $Sc$  number from  $\frac{1}{4}$  to  $\frac{1}{3}$  showed better agreement with the already described calculation procedure based on equ. (28) for the corroded sample. After this modification,  $Sh$  number from this equation is in very good agreement with the simulation results for CWTD dissolution experiment. Equation (40) represents the modified Sherwood relation for the mantle of the cylindrical sample [91].

$$Sh_{0,m} = \frac{\beta_0 \cdot (R_2 - R_1)}{D} = 0.21 \cdot Re^{\frac{1}{2}} \cdot Sc^{\frac{1}{3}} \cdot \left(\frac{R_2 - R_1}{R_1}\right)^{\frac{1}{4}}; \quad Re = \frac{\omega \cdot R_1 \cdot (R_2 - R_1)}{\nu} \quad (40)$$

Equation (41) represents the Sherwood relation for the bottom of a rotating cylinder in a finger test setup according to Levich [22].

$$Sh_{0,b} = \frac{\beta_0 R_t}{D} = 0.62 Re^{\frac{1}{2}} S c^{\frac{1}{3}}; Re = \frac{\omega R_t^2}{\nu} \quad (41)$$

Here,  $R_t$  is the tip radius.

According to equation (34) total mass flux can be represented by equation (42) and equation (43) for the submerged mantle and cylinder bottom.

$$j_{tot} \cdot A_{tot} = j_m \cdot A_m + j_b \cdot A_b; A_m = 2R_1 \pi l; A_b = R_t^2 \pi; A_{tot} = A_m + A_b \quad (42)$$

$$j \cdot A_{tot} = \chi_D \cdot D \cdot \left\{ A_m \cdot \frac{Sh_{0,m}}{R_2 - R_1} + A_b \cdot \frac{Sh_{0,b}}{R_t} \right\} \rho^s \cdot B \quad (43)$$

Here,  $j_{tot}, j_m, j_b$  and  $A_{tot}, A_m, A_b$  are the mass flux densities and surface areas of total surface, mantle and bottom of the cylinder respectively,  $l$  the immersion length and  $\rho^s$  is the density of the slag. Combining equations (38), (40), (41) and (43) yields the equation (44) [91].

$$j = \frac{1}{1 + 0.566 \cdot B} \cdot \frac{1}{2l \cdot R_1 + R_t^2} \cdot \frac{\omega^{\frac{1}{2}} \cdot \rho^s \cdot B}{\nu^{\frac{1}{6}}} \cdot D^{\frac{2}{3}} \cdot \left\{ 0.42 \cdot \frac{l \cdot R_1^{\frac{5}{4}}}{(R_2 - R_1)^{\frac{1}{4}}} + 0.62 \cdot R_t^2 \right\} \quad (44)$$

After rearranging equation (44) the effective binary diffusivity ( $D_c$ ) for an individual corrosion step  $c$  (step between laser measurements at  $t_{c-1}$  and  $t_c$ ) can be determined using equation (45) [91]. In one dissolution experiment, there are data of several in-situ measured profiles. Average of the diffusivities of all corrosion steps can provide a representative diffusivity ( $D_{0,c}$ ) [91].

$$D_c = \left[ \frac{j \cdot (1 + 0.566 \cdot B) \cdot (2l \cdot R_1 + R_t^2) \cdot (R_2 - R_1)^{\frac{1}{4}} \cdot \nu^{\frac{1}{6}}}{\omega^{\frac{1}{2}} \cdot \rho^s \cdot B \cdot \left\{ 0.42 \cdot l \cdot R_1^{\frac{5}{4}} + 0.62 \cdot R_t^2 \cdot (R_2 - R_1)^{\frac{1}{4}} \right\}} \right]^{\frac{3}{2}} \quad (45)$$

## 4. Materials

### 4.1. Slags

Three silicate and one calcium-aluminate slags were selected for this research work. Slag batches were prepared from pure oxide components. Quartz powder, calcined alumina, magnesium oxide powder and calcium carbonate (S3 Handel und Dienstleistungen UG) were

used as  $\text{SiO}_2$ ,  $\text{Al}_2\text{O}_3$ ,  $\text{MgO}$  and  $\text{CaO}$  source respectively. Slag preparation has been described in the section 3.2.1.1. First, all the raw materials were analyzed using wavelength dispersive X-ray fluorescence (WDXRF) and inductively coupled plasma (ICP) to get accurate chemical analysis. As per the chemical analysis of raw materials and targeted slag compositions, raw materials were weighed and mixed afterwards.

**Table 3** shows the chemical compositions and liquidus temperatures of the slags as calculated with FactSage 7.2. Slags are tabulated in **Table 3** with increasing basicity.

**Table 3: Chemical compositions and liquidus temperatures of slags.**

Slag No.	Slag type	CaO [wt%]	MgO [wt%]	$\text{Al}_2\text{O}_3$ [wt%]	$\text{SiO}_2$ [wt%]	$T_L$ [ $^\circ\text{C}$ ]
S1	CASM, $C/(S+A)=0.53$	32.42	6.86	11.16	49.56	1265
S2	CAS, $C/(S+A)=0.61$	38.07	-	21.00	40.93	1301
S3	CASM, $C/(S+A)=0.90$	45.03	5.00	11.33	38.64	1317
S4	CASM, $C/(S+A)=0.94$	46.00	5.00	46.00	3.00	1334

Densities of the slags at 1450, 1500 and 1550 $^\circ\text{C}$  were determined according to density calculation model of Xin et al. [95]. This model is based on constant thermal expansion coefficients and composition dependent excess molar volume. **Figure 27** represents the calculated densities which slightly decrease with increasing temperature. The composition of S4, partially lies beyond the validity range of the model.

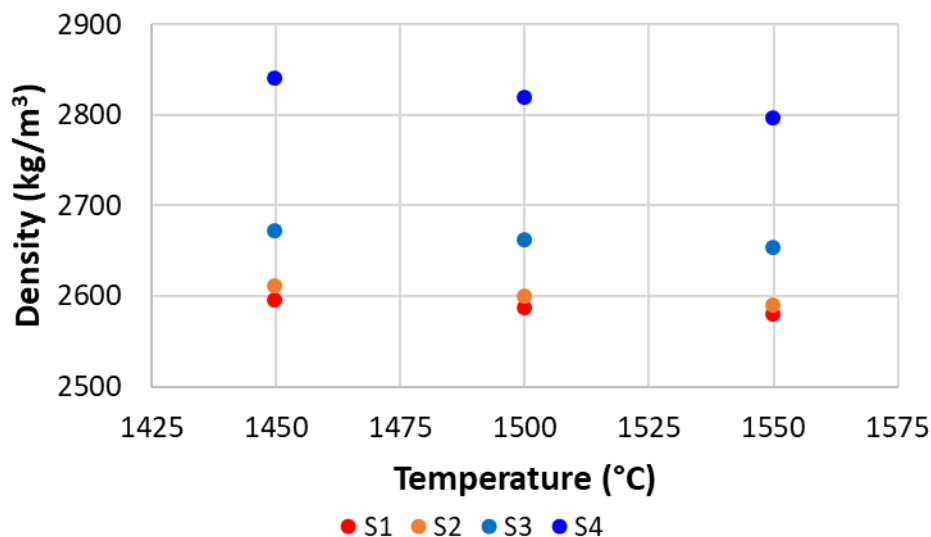


**Figure 27: Densities of slags at 1450, 1500 and 1550  $^\circ\text{C}$ .**

Viscosities of virgin, alumina saturated and magnesia saturated slags as well as saturation limits over the temperature range were calculated using FactSage 7.2. **Figure 28** a)-d) represent the viscosities of virgin slags, alumina saturated slags and saturation limits of alumina at different temperatures in S1, S2, S3 and S4 respectively. The viscosities are higher for the alumina saturated slags, and the viscosity increase at a lower temperature is larger



than that at a higher temperature. Saturation limit of alumina increases with increasing temperature and basicity.

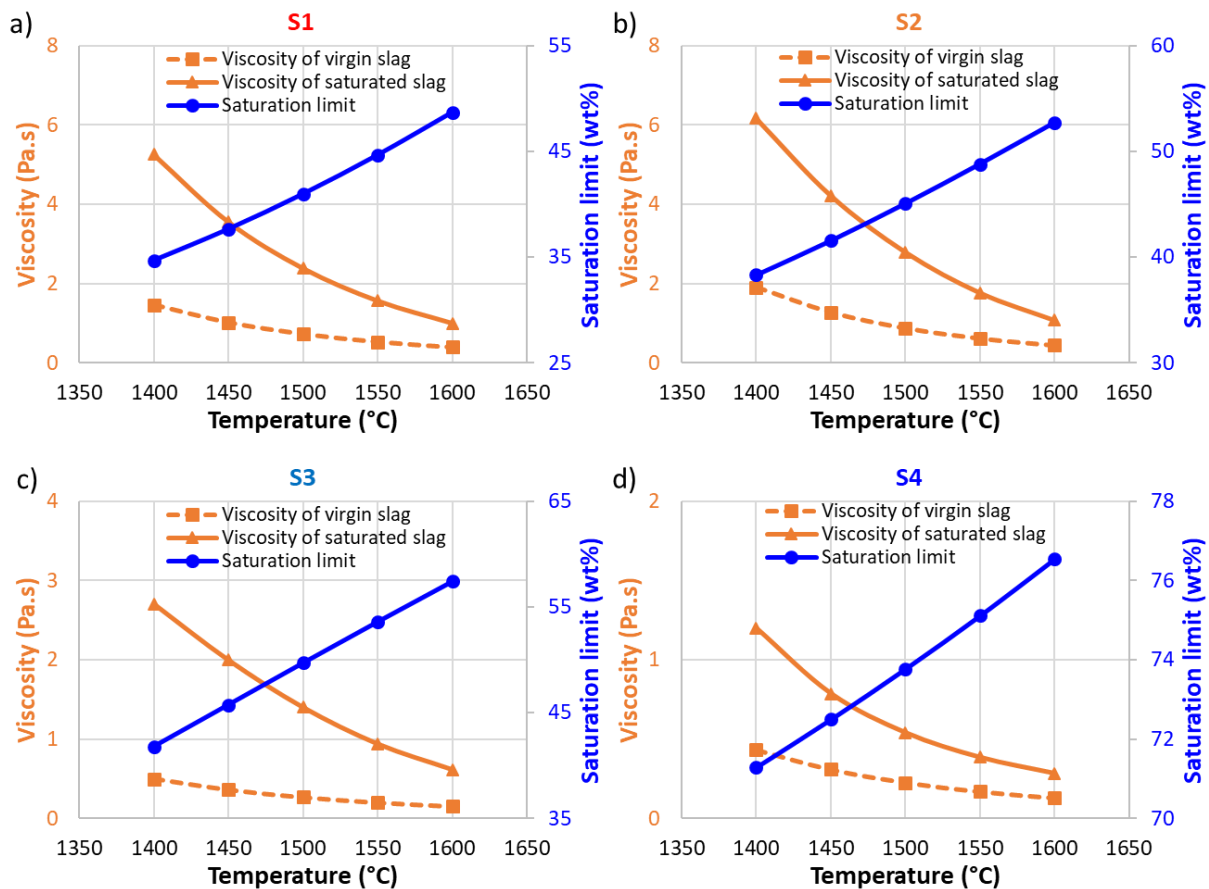


**Figure 28:** a), b), c) and d) viscosities of virgin slags, alumina saturated slags and saturation limits of alumina at different temperatures in S1, S2, S3 and S4 respectively.

The viscosities of virgin slags, magnesia saturated slags and saturation limits of magnesia at different temperatures in S1, S2, S3 and S4 are represented by **Figure 29** a)-d) respectively. Viscosities of magnesia saturated slags are lower than that of virgin slags due to the network modification by introduction of magnesia. The viscosity decrease due to dissolution at lower temperature is larger than at higher temperature in S1, S2 and S3 slags, whereas this trend is missing in S4. Saturation limit of magnesia increases with increasing temperature and decreasing basicity.

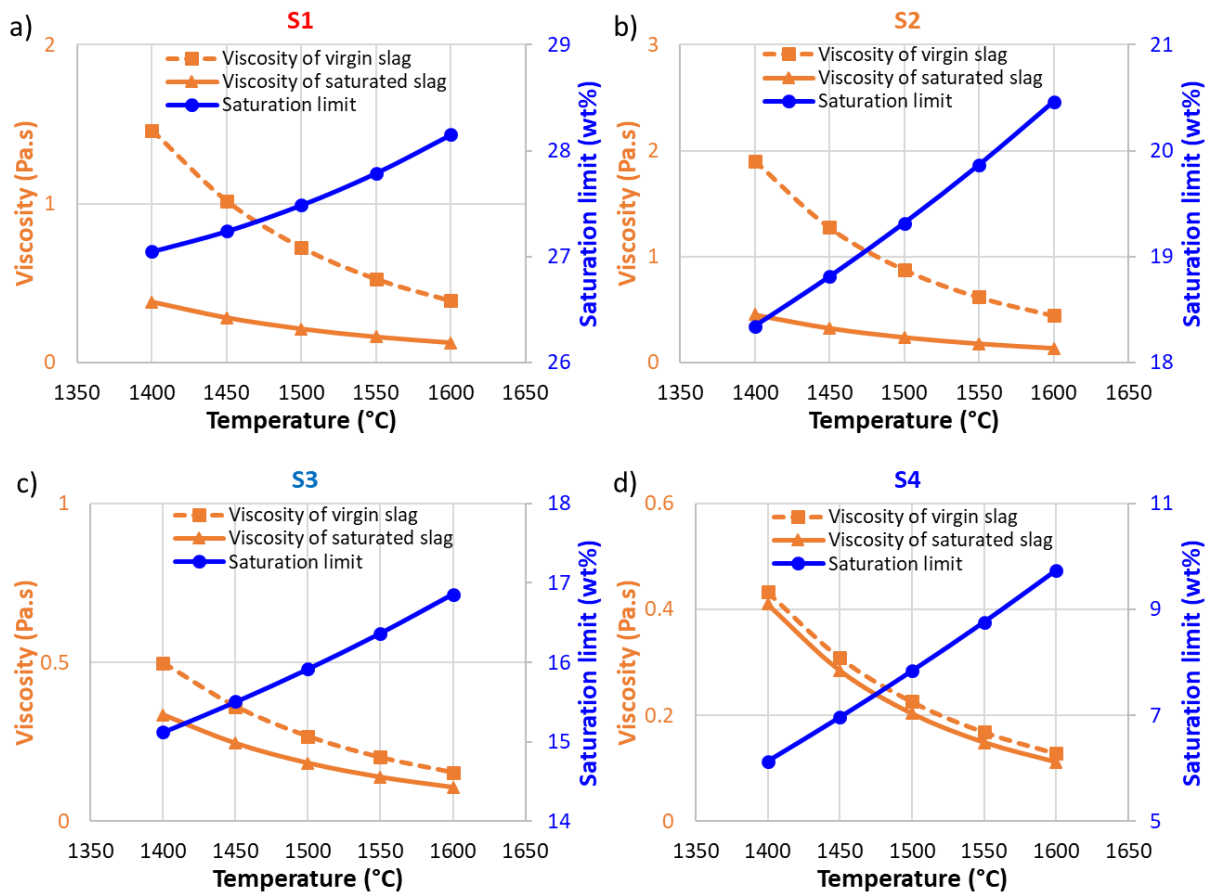


Figure 29: a), b), c) and d) viscosities of virgin slags, magnesia saturated slags and saturation limits of magnesia at different temperatures in S1, S2, S3 and S4 respectively.

## 4.2. Refractory materials

Oxide particles were used for the dissolution experiments with CLSM. Mono-crystal sapphire (Sandoz Fils SA, Switzerland) polished spheres of 350  $\mu\text{m}$  diameter were used for alumina dissolution. Alumina content was 99.99 wt% and density 3.99  $\text{g}/\text{cm}^3$ . The sapphire particles dissolved almost completely before reaching isothermal temperature in S4 at 1550  $^{\circ}\text{C}$  due to extremely high dissolution rate. White fused alumina (WFA) particles (99.5 wt%  $\text{Al}_2\text{O}_3$ , 3.96  $\text{g}/\text{cm}^3$ ) of 500 to 1000  $\mu\text{m}$  were used for the dissolution experiments in S4 at 1550  $^{\circ}\text{C}$ . 300 to 500  $\mu\text{m}$  fused magnesia particles with a magnesia content 98.66 wt% and a density of 3.58  $\text{g}/\text{cc}$  were used for the dissolution experiments in CLSM.

Alumina and magnesia fine ceramics served for the dissolution experiments in CWTD: alumina fine ceramics (Ants Ceramics Private Limited, India) with 99.7 wt%  $\text{Al}_2\text{O}_3$  and a bulk density of 3.87  $\text{g}/\text{cm}^3$  and magnesia fine ceramics (Surtec Research Europe GmbH, Germany) with 99.6 wt%  $\text{MgO}$  and a bulk density of 3.40  $\text{g}/\text{cm}^3$ . The fine ceramic cylinders of 20 mm diameter and 110 mm length were used. All samples had an axial drill of 5 mm diameter and 32 mm depth, and a side drill of 3.5 mm diameter to fix the cylinder with the rotor shaft [91].

## 5. Results and discussion

### 5.1. HT-CLSM studies for alumina dissolution

CLSM studies for alumina dissolution were conducted at 1450, 1500 and 1550 °C in ambient atmosphere in all above mentioned slags (Table 3). Dissolution times, rates and diffusivities were determined.

#### 5.1.1. Dissolution curves

Dissolution times of a particular size of particles can be compared by the dissolution curves. Figure 30 a)-d) represent the dissolution curves for alumina in S1, S2, S3 and S4 at 1450, 1500 and 1550 °C, respectively. Represented dissolution curve for a particular temperature is the average of several dissolution experiments. The number of experiments conducted at each temperature, the average standard deviations and coefficient of variations of the dissolution time are tabulated in Table 4. It was not possible to start the dissolution curves for S3 and S4 from 300 µm due to higher dissolution rates. Dissolution time rises with decreasing temperature. Dissolution time at 1450 °C in S3 abruptly increased relative to 1500 °C. Clear correlation between slag basicity and dissolution time of alumina is not observed here. Results of alumina dissolution in S1 is reported in [4].

**Table 4: Number of alumina dissolution experiments conducted at each temperature, average standard deviations and coefficient of variation of dissolution time.**

Slag	Number of experiments conducted			Standard deviation of dissolution time (s)			Coefficient of variation of dissolution time (%)		
	1450 °C	1500 °C	1550 °C	1450 °C	1500 °C	1550 °C	1450 °C	1500 °C	1550 °C
S1	5	5	5	23.0	9.8	8.0	7.2	6.2	12.4
S2	5	5	4	23.8	29.8	9.1	7.5	12.6	7.4
S3	4	5	5	45.4	4.7	4.0	7.8	8.8	13.3
S4	5	5	5	0.8	0.2	0.5	4.7	3.2	22.2

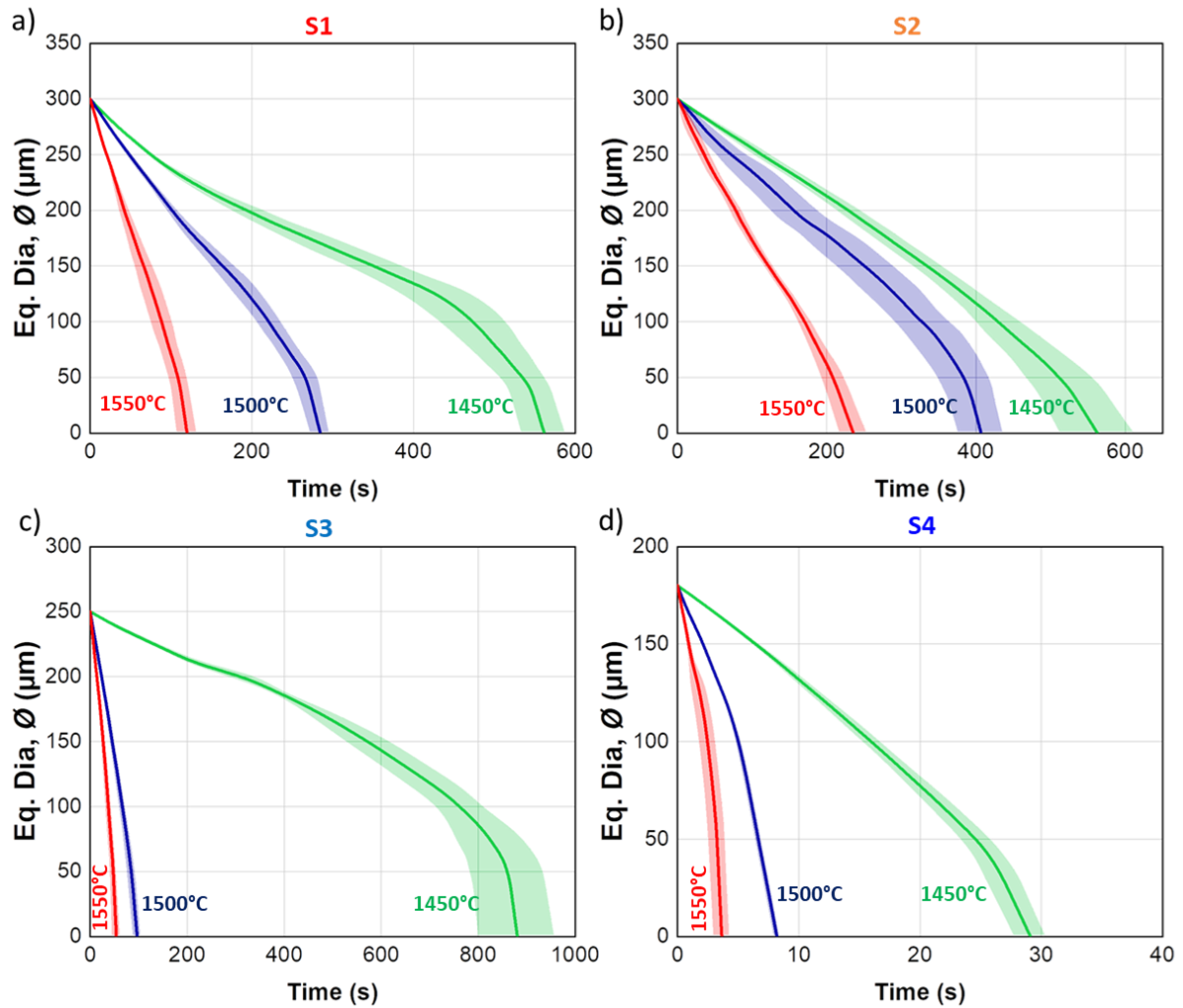


**Figure 30:** a), b), c) and d) dissolution curves for alumina in S1, S2, S3 and S4 respectively at 1450, 1500 and 1550 °C. Shaded area represents the standard deviation of dissolution time.

### 5.1.2. Dissolution rate

Figure 31 a)-d) show the dissolution rates in S1, S2, S3 and S4 respectively at 1450, 1500 and 1550 °C. Absolute rate of dissolution rate increases with rising temperature [4]. At a particular temperature, absolute value of dissolution rate decreases at the beginning to a minimum due to the development of boundary layer and then again increases because of higher ratio of surface area to volume of the particle at the later phase of dissolution. Absolute values of dissolution rates of alumina in S4 are very high compared to others presumably due to lower slag viscosity and higher concentration difference of alumina in bulk and saturated slags.

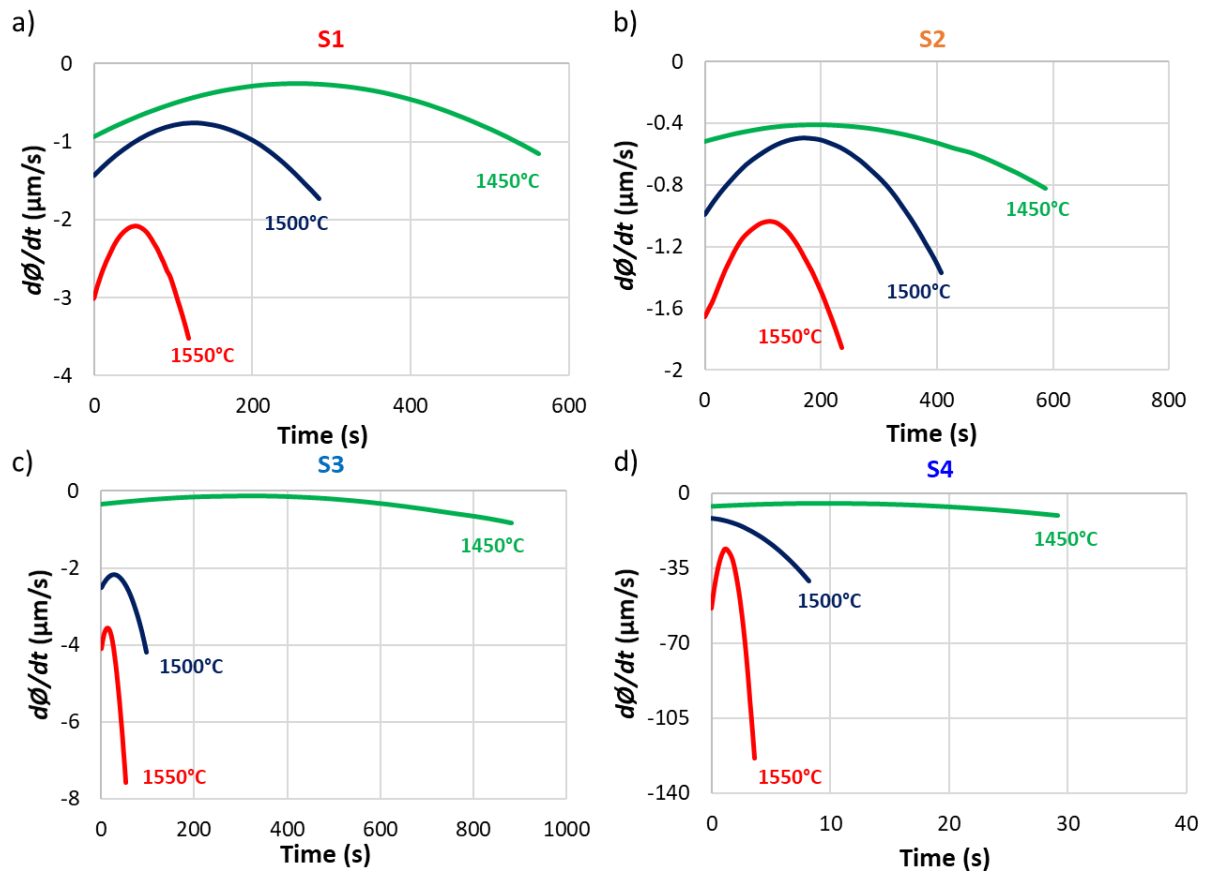


Figure 31: a), b), c) and d) dissolution rates of alumina in S1, S2, S3 and S4 respectively at 1450, 1500 and 1550 °C.

### 5.1.3. Diffusivity

Diffusivities of all individual experiments in four slags and at three experimental temperatures were determined with three models M1, M2 and M3 (see section 3.3.1.3). The average of diffusivities at a particular temperature and slag is considered as the representative diffusivity for these experimental conditions. **Figure 32** a)-d) depict the average diffusivities of alumina with three different models at 1450, 1500 and 1550 °C in S1, S2, S3 and S4 slags respectively. Diffusivity increases with rising temperature in all cases. M1 shows highest and M3 shows lowest value of diffusivity at a particular temperature. Diffusivities of alumina in S4 are largest among others and at 1450 °C in S3 are lowest. Fitting quality of model and measured radius can be quantified with the squared correlation coefficient  $r_c^2$ . The average  $r_c^2$  values for the models at different experimental conditions are mentioned on the bar charts. Always the fitting quality is far better for M3 than the other two.

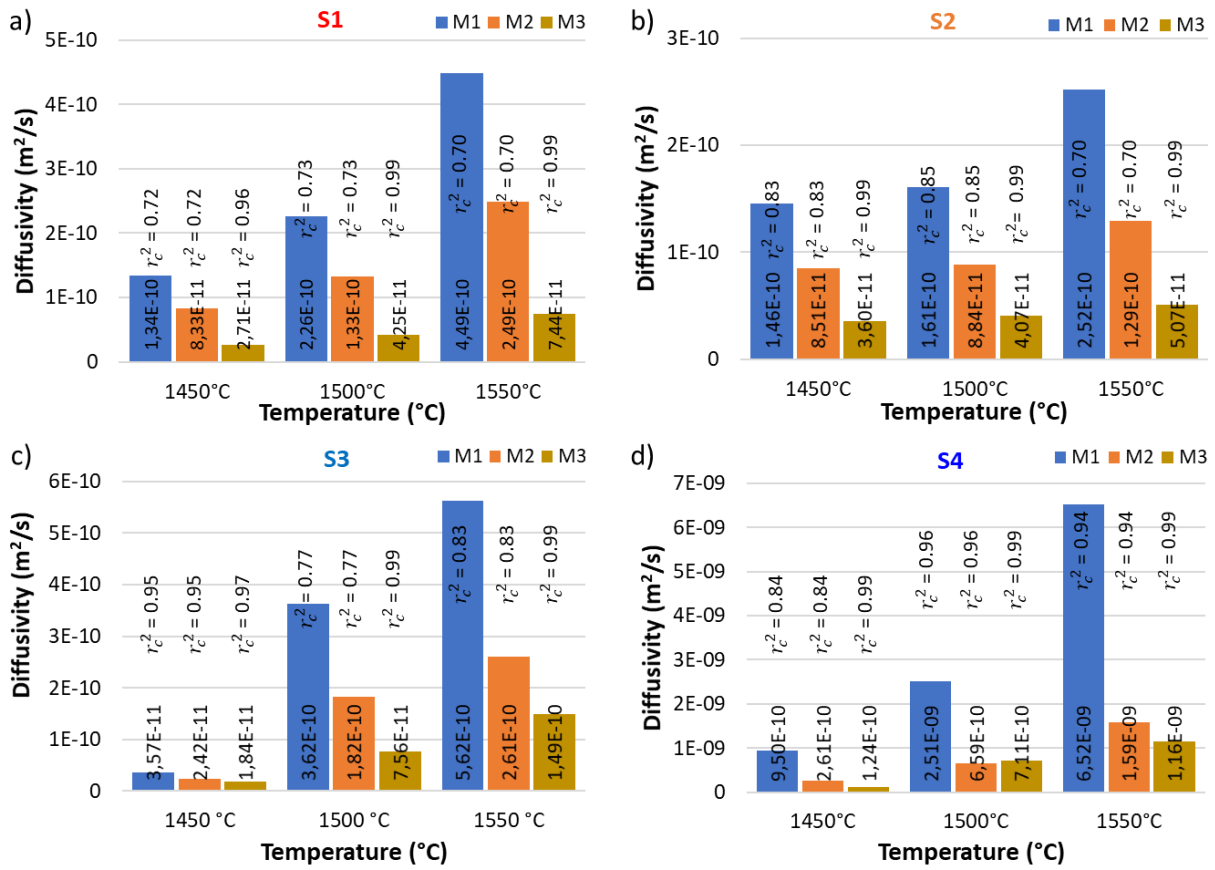


Figure 32: a), b), c) and d) diffusivities of alumina at 1450, 1500 and 1550 °C in S1, S2, S3 and S4 respectively.

According to [4], to assess the diffusivity determination models for CLSM experiments, as an example, the measured and the model radius ( $R$ ) and the effective boundary layer thickness ( $\delta$ ) in dependence on time at three experimental temperatures have been compared in **Figure 33** b)-d) for alumina dissolution in S1. For M1 and M2 diffusivity has been calculated from the total dissolution time. For M3 the information of the whole curve is considered and  $K$  and  $D$  are determined by minimization of sum of square residuals. For comparison of the models and assessment of their suitability, the effective diffusive boundary layer thickness is calculated in two ways. Results of the first procedure are denominated by  $\delta_{1,j}$  where the subscript  $j$ ,  $j = 1, 2, 3$  refers to the methods M1-M3. These  $\delta_{1,j}$  are defined by:

$$\delta_{1,j} = R(D_j) = R^{(j)}; j = 1, 2 \quad (46)$$

$$\delta_{1,3} = \delta(D_3, K); R(D_3, K) = R^{(3)} \quad (47)$$

Here  $R^{(j)}$  is calculated according to the Models M1 and M2 with the respective diffusivity  $D_j$  already identified before [4]. For  $\delta_{1,3}$  the calculation was performed according to equation (17) with the parameters  $K$  and  $D$  as identified by minimization of sum of square residuals before and applied for calculating the resulting radius  $R^{(3)}$  according to equation (16). Contrary to this, experimental boundary layer thickness ( $\delta_{2,j}$ ) is calculated from the derivative of the

measured radius  $R_m$  ( $m$ = measured) radius with respect to time. For this, a curve fit with a third order polynomial of the measured  $R_m$  over time  $t$  curves is employed. Then, in accordance with equations (10), (15) and (16) boundary layer thicknesses are calculated by:

$$\delta_{2,1} = -\frac{D_1(c_s^l - c_0^l)}{\rho^p} \bigg/ \frac{dR_m}{dt} \quad (48)$$

$$\delta_{2,j} = -\frac{D_j(c_s^l - c_0^l)}{(c^s - V_v \cdot c_s^l)} \bigg/ \frac{dR_m}{dt}; j = 2,3 \quad (49)$$

M3 shows the most satisfying results with respect to both the fit of the radius curves and the agreement between  $\delta_1$  and  $\delta_2$ . For M1 and M2 – which differ in  $D$ , but not in the resulting radii and boundary layer thicknesses – a systematic offset between measured and calculated radius and a remarkable discrepancy between  $\delta_{2,j}$  and  $\delta_{1,j}$  falsifying the assumption of  $\delta = R$  applied in equations (10) and (15) can be observed. Of course, the radius offset could be decreased by not using the final dissolution time only but also the information of all measured radii by a regression procedure like it was done for M3. But this has the disadvantage that the time of total dissolution then shows a disruptive deviation of the measured and calculated total dissolution time. Models M1 and M2 suffer from the fact they cannot represent the curve shape well, as their assumption regarding the effective diffusive boundary layer thickness proofs to be not accurate enough [4].

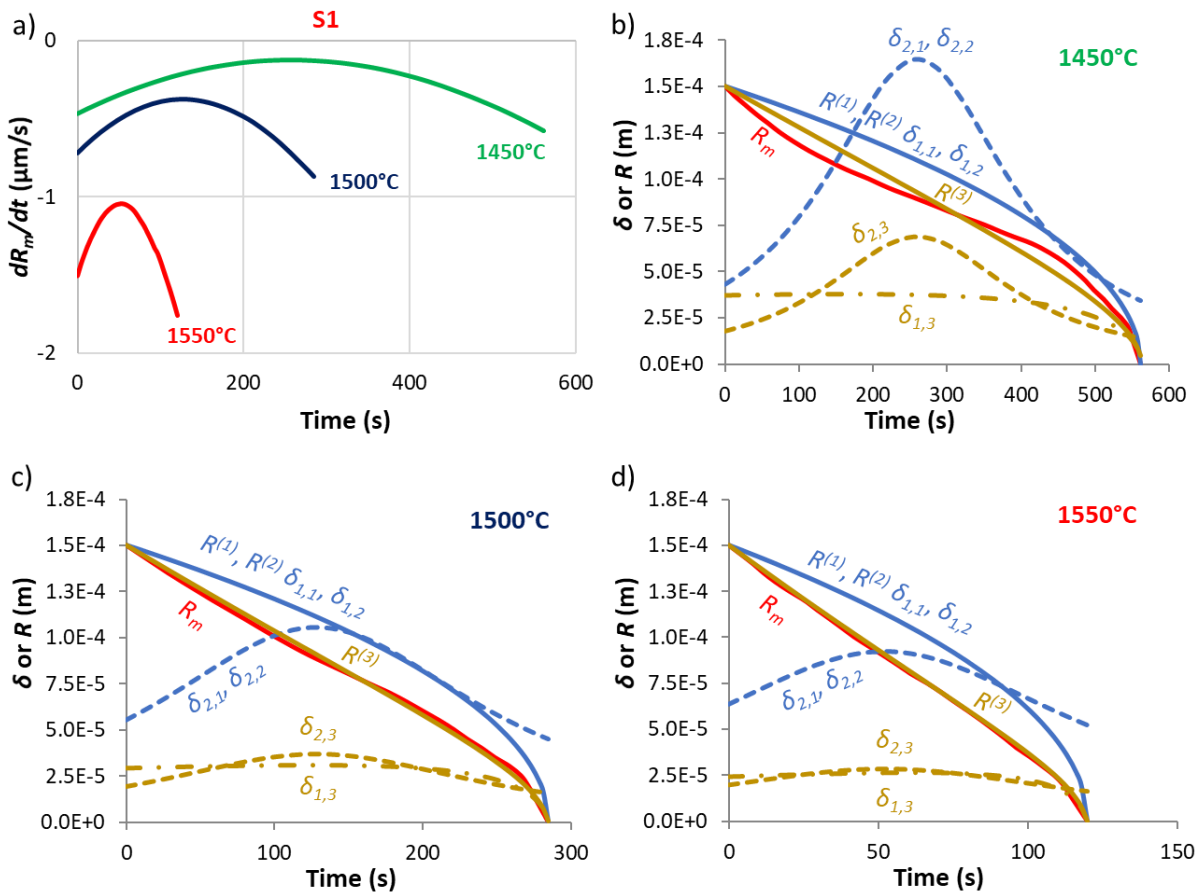


Figure 33: a) dissolution rates in S1 at 1450, 1500 and 1550 °C, b), c) and d) measured and model radius and effective boundary layer thickness over dissolution time at 1450, 1500 and 1550 °C respectively [4].

Table 5: Statistical comparison of the three models [4].

Parameters	Model	1450 °C	1500 °C	1550 °C
$r_c^2$ <sup>1)</sup>	<b>M1 &amp; M2</b>	0.72	0.73	0.70
	<b>M3</b>	0.96	0.99	0.99
$\Delta_j$ <sup>2)</sup>	<b>M1 &amp; M2</b>	13.9	20.5	24.2
	<b>M3</b>	6.1	3.8	2.5

<sup>1)</sup> Coefficient of determination ( $r_c^2$ ), calculated from measured radius and that of the respective model

<sup>2)</sup> For definition of this mean relative error see equation (50) and corresponding text.

The superiority of M3 is also shown in Table 5 by the coefficient of determination. Further, this table shows that for M3  $\delta_1$  is closer to the experimental  $\delta_2$  than for the other two models. This is expressed by the quantity  $\Delta_j$  representing an average relative error defined in the following way:



$$\Delta_j = \frac{\bar{\delta}_{1,j} - \bar{\delta}_{2,j}}{\bar{\delta}_{2,j}} 100\%; j = 1,2,3 \quad (50)$$

Here  $\bar{\delta}_{1,j}$  and  $\bar{\delta}_{2,j}$  are the mean of  $\delta_{1,j}$  and  $\delta_{2,j}$  with respect to the time, respectively. These values show that the approach used for the effective diffusive boundary layer thickness for M3 is more suitable than that of M1 and M2 [4]. Further, the accuracy of the model will be tested later by comparison with diffusivity results obtained from CWTD experiments, where the boundary layer thickness is defined accurately.

Figure 34 a)-d) show the Arrhenius plots of diffusivities of alumina in S1, S2, S3 and S4, respectively for all three models. The linear tendency of Arrhenius plot confirms the plausibility of diffusivities. Though the diffusivities from the shrinking core models with and without convective part of mass flux also show linear trend in Arrhenius plot (maybe due to the consistency of experiment with respect to temperatures) they have many fundamental deficiencies. Table 6 shows the activation energies of diffusion calculated from the Arrhenius plots. For alumina dissolution, activation energies are higher for S3 and S4 slags.

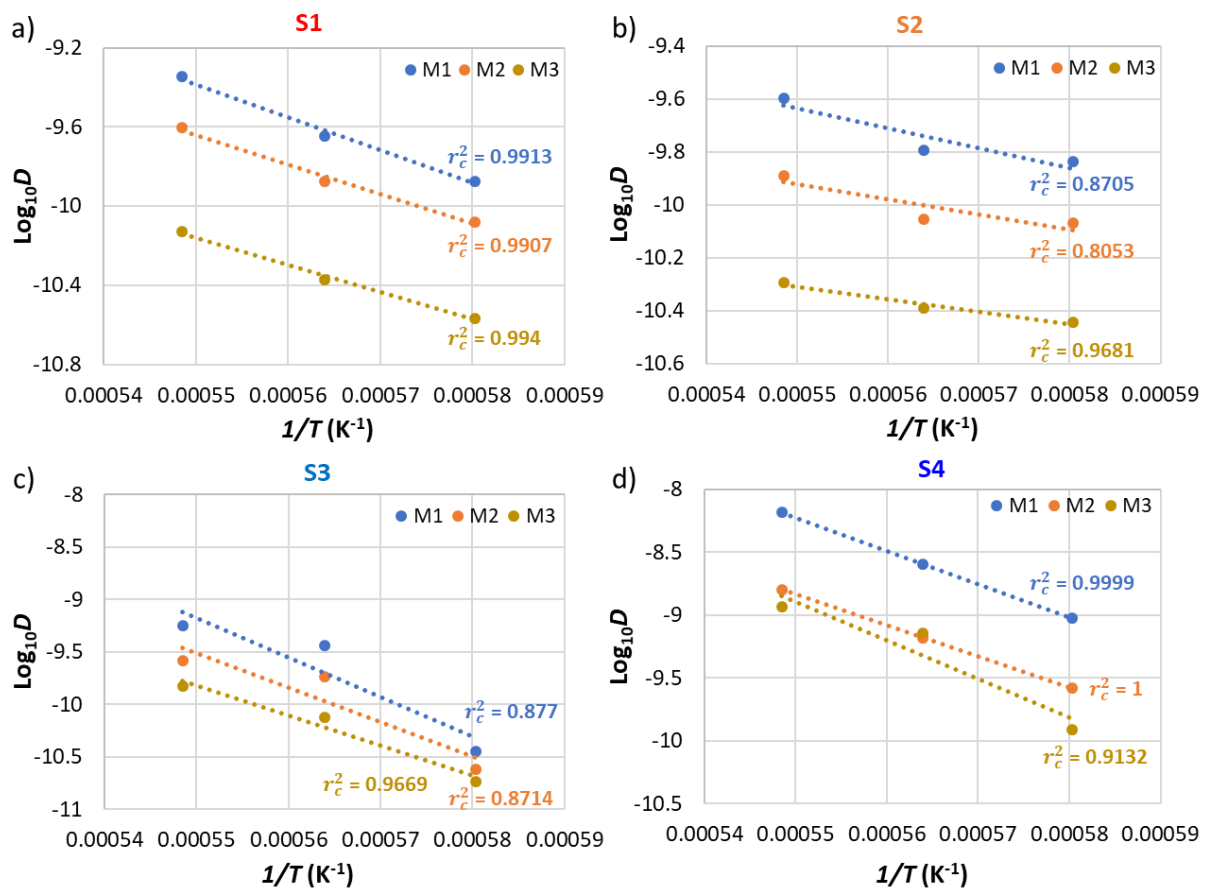


Figure 34: a), b), c) and d) Arrhenius plot of diffusivities of alumina in S1, S2, S3 and S4 respectively.

**Table 6: Activation energy of diffusion.**

Model	Activation energy of diffusion (kJ/mol)			
	S1	S2	S3	S4
M1	316	142	724	503
M2	285	108	624	472
M3	264	89	549	587

## 5.2. HT-CLSM studies for magnesia dissolution

CLSM studies for magnesia dissolution were conducted using fused magnesia particles at 1450, 1500 and 1550 °C in ambient atmosphere in all above mentioned slags (**Table 3**). Dissolution times, rates and diffusivities were determined.

### 5.2.1. Dissolution curves

Dissolution times of a particular size (300 µm) of particles were compared in the dissolution curves. **Figure 35 a)-d)** represent the dissolution curves for magnesia in S1, S2, S3 and S4 respectively at 1450, 1500 and 1550 °C. Here also the represented dissolution curve for a particular temperature is the average of several dissolution experiments. The number of experiments conducted at each temperature, the average standard deviations and coefficient of variations of the dissolution times are tabulated in **Table 7**. In case of magnesia dissolution, it was possible to compare from 300 µm initial particle diameter at isothermal conditions in all experiments. Dissolution time rises with decreasing temperature and the effect of temperature is clearly visible from the distinguished dissolution curves. As expected, the dissolution time of magnesia increases with rising slag basicity especially at higher temperature.

**Table 7: Number of magnesia dissolution experiments conducted at each temperature, average standard deviations and coefficient of variation of dissolution time.**

Slag	Number of experiments conducted			Standard deviation of dissolution time (s)			Coefficient of variation of dissolution time (%)		
	1450 °C	1500 °C	1550 °C	1450 °C	1500 °C	1550 °C	1450 °C	1500 °C	1550 °C
S1	5	5	4	17.9	9.2	5.4	15.5	15.5	14.6
S2	5	5	5	27.5	10.7	3.4	9.9	7.2	6.8
S3	5	5	5	31.6	8.7	4.7	13.0	8.7	7.1
S4	3	3	3	62.4	44.6	7.1	10.8	11.1	2.8

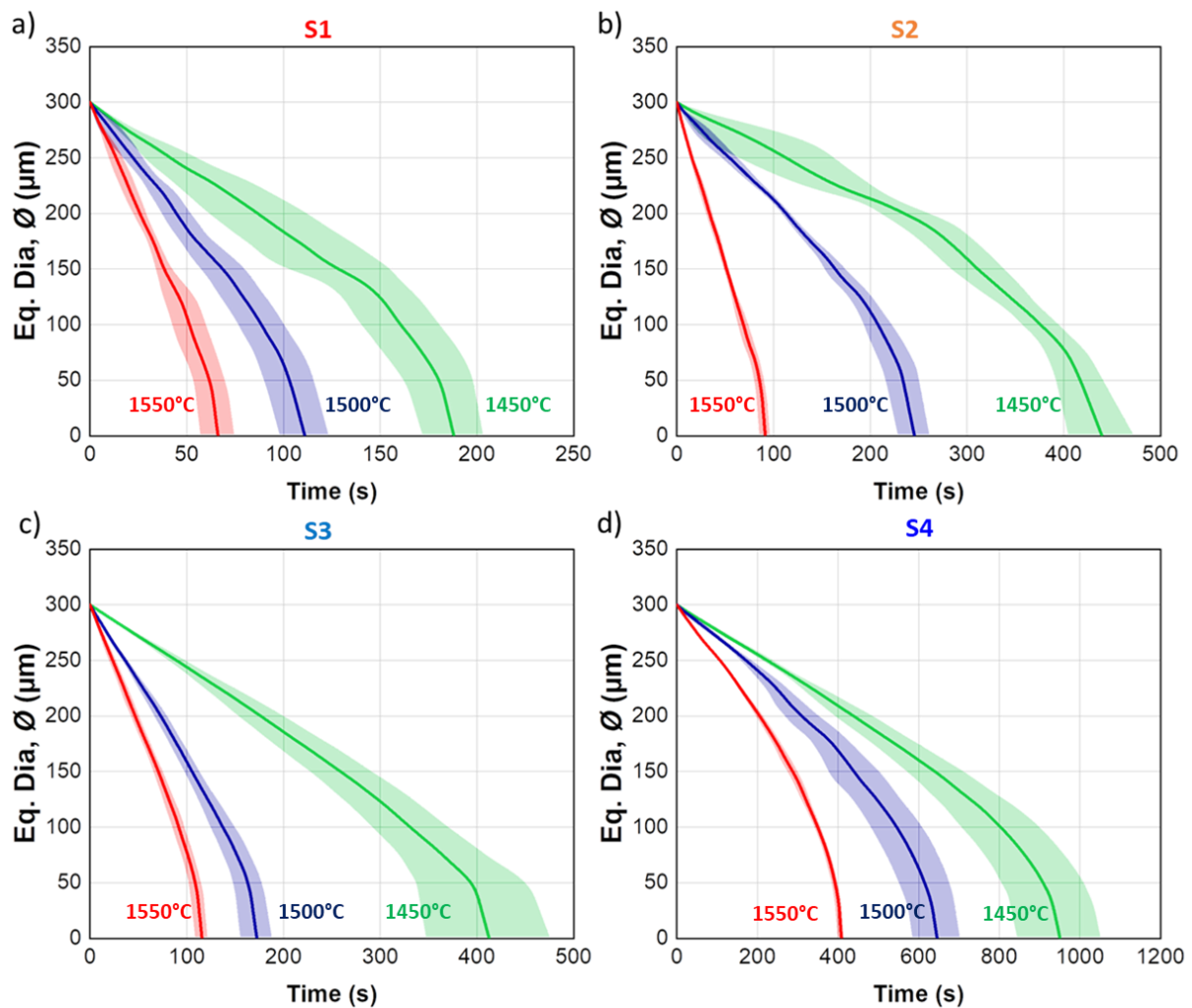


**Figure 35:** a), b), c) and d) dissolution curves for magnesia in S1, S2, S3 and S4 respectively at 1450, 1500 and 1550 °C. Shaded area represents the standard deviation of dissolution time.

### 5.2.2. Dissolution rate

Figure 36 a)-d) show the dissolution rates of magnesia in S1, S2, S3 and S4 respectively at 1450, 1500 and 1550 °C. Absolute value of dissolution rate increases with rising temperature. Similar to alumina dissolution, at a particular temperature, absolute value of dissolution rate decreases at the beginning to a minimum absolute value due to the development of boundary layer and again increases because of higher ratio of surface area to volume of the particle at the later phase of dissolution. Absolute value of dissolution rate of magnesia decreases with rising slag basicity. S4 show the lowest absolute value of dissolution rate for magnesia contrary to alumina dissolution.

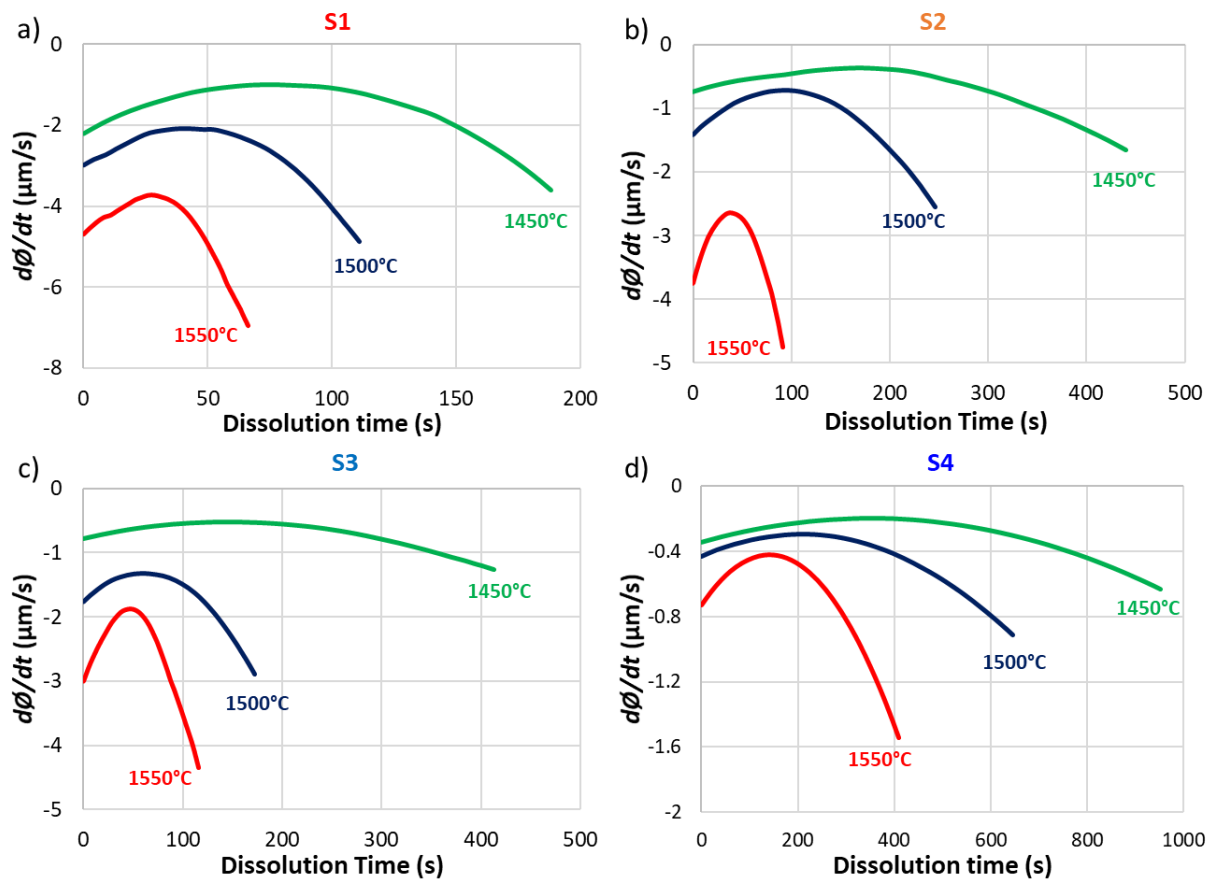


Figure 36: a), b), c) and d) dissolution rates of magnesia in S1, S2, S3 and S4 respectively at 1450, 1500 and 1550 °C.

### 5.2.3. Diffusivity

Similar to alumina dissolution, diffusivities of all individual experiments in four slags and at three experimental temperatures were determined with three models M1, M2 and M3 (see section 3.3.1.3). **Figure 37** a)-d) represents the average diffusivities of magnesia with three different models at 1450, 1500 and 1550 °C in S1, S2, S3 and S4 slags, respectively. Diffusivity increases with rising temperature in all cases. Diffusivity of magnesia in S2 at 1450 °C is the lowest. Diffusivities of magnesia show no clear trend with slag basicity, though absolute value of dissolution rate of magnesia decreases with rising slag basicity. This means that decrease of solubility with rising slag basicity is a major factor impacting dissolution rate. The average  $r_c^2$  values for the models at different experimental conditions are mentioned on the bar charts. Also here the  $r_c^2$  values are always far better for M3 than other two. Compared to alumina dissolution, shrinking core models show better fits for magnesia dissolution.

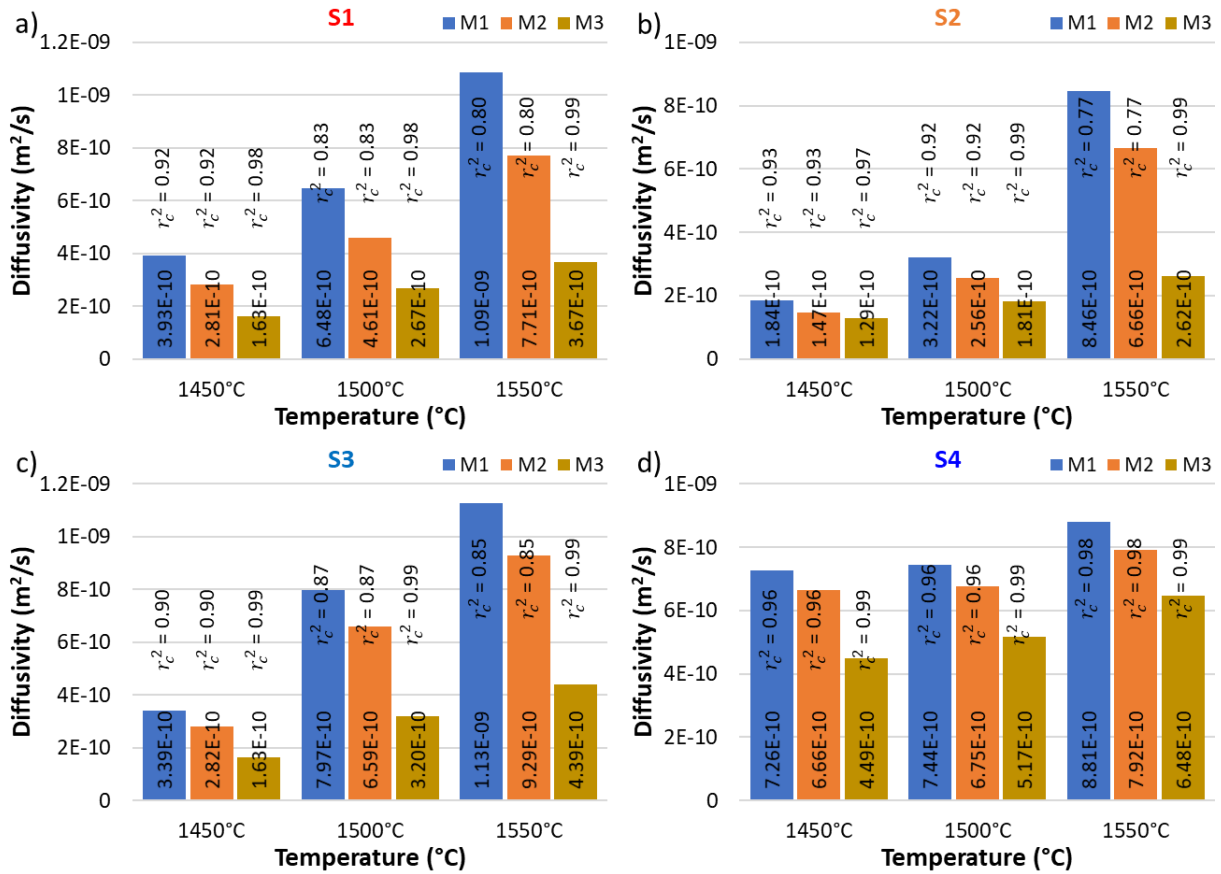


Figure 37: a), b), c) and d) diffusivities of magnesia at 1450, 1500 and 1550 °C in S1, S2, S3 and S4 respectively.

Figure 38 a)-d) represents the Arrhenius plot of diffusivities of magnesia in S1, S2, S3 and S4, respectively for all three models. The linear tendency of Arrhenius plot confirms the plausibility of diffusivities. Table 8 shows the activation energies of diffusion, calculated from the Arrhenius plots. For magnesia dissolution, activation energies are lowest for S4 slags.

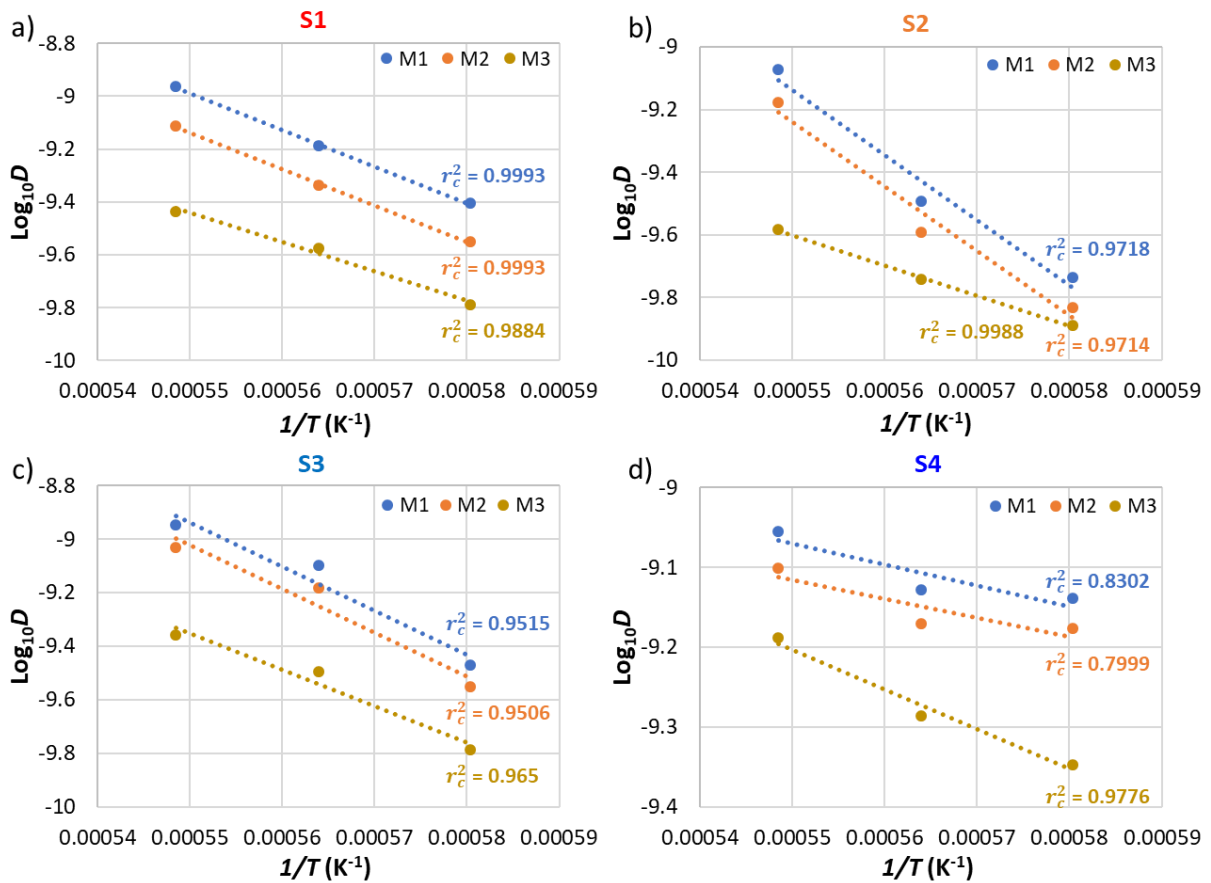


Figure 38: a), b), c) and d) Arrhenius plots of diffusivities of magnesia in S1, S2, S3 and S4 respectively.

Table 8: Activation energy of diffusion.

Model	Activation energy of diffusion (kJ/mol)			
	S1	S2	S3	S4
M1	266	397	315	50
M2	264	394	313	45
M3	213	185	259	95

### 5.3. Dissolution studies of alumina fine ceramics in CWTD

Dynamic and static dissolution experiments of alumina fine ceramics were carried out in S1 and S2 slags in ambient atmosphere. Dynamic experiments with 200 rpm were conducted at 1450, 1500 and 1550 °C to study the effect of temperature on dissolution. The effect of rotational speed on dissolution rate was examined by the experiments at 0 and 100 rpm additional to 200 rpm at 1550 °C. S3 and S4 slags were excluded from the CWTD experiments due to their crystallization tendency during cooling after the experiment and the harmful stresses on the Pt-Rh10 crucible caused by crystallization. **Table 9** and **Table 10** show the test conditions for CWTD experiments of alumina fine ceramics in S1 and S2 slags, respectively. Bottom clearance was measured at room temperature (RT) at the beginning of the experiments and increases with dissolution time. Dissolution results of alumina fine ceramics in S1 at 1450, 1500 and 1550 °C with 200 rpm is reported in [91].

**Table 9: Test conditions for CWTD experiments of alumina fine ceramics in S1.**

Target temperature (°C)	1450	1500	1550	1550	1550
Rotational speed (min <sup>-1</sup> )	200	200	200	100	0
Dropping time (min)	30	30	30	30	30
Corrosion time per step (min)	135	105	90	90	90
Number of corrosion steps targeted (1)	9	8	8	8	8
Bottom clearance at RT (mm)	23.8	23.8	23.3	23.8	20.8
Corrosion steps conducted (1)	9/9	8/8	6/8	7/8	6/8
Total corrosion time (min)	1215	840	540	630	540

**Table 10: Test conditions for CWTD experiments of alumina fine ceramics in S2.**

Target temperature (°C)	1450	1500	1550	1550	1550
Rotational speed (min <sup>-1</sup> )	200	200	200	100	0
Dropping time (min)	30	30	30	30	30
Corrosion time per step (min)	150	90	60	60	60
Number of corrosion steps targeted (1)	8	8	8	8	8
Bottom clearance at RT (mm)	23.8	21.4	21.4	22.8	22.8
Corrosion steps conducted (1)	8/8	8/8	8/8	8/8	8/8
Total corrosion time (min)	1200	720	480	480	480

### 5.3.1. CW curves for alumina dissolution

Figure 39 a)-c) show the CW curves for the alumina dissolution with 200 rpm in S1 slag at 1450, 1500 and 1550 °C, respectively [91]. CW curves for dynamic corrosion experiments with 200 rpm in S2 slag at 1450, 1500 and 1550 °C are depicted in Figure 41 a)-c), respectively. Figure 40 [91] and Figure 42 represent the virgin and corroded alumina samples in S1 and S2 slags, respectively, at all experimental temperatures with 200 rpm. The CW curves for the last corrosion steps show good agreement with corroded sample shape. The un-corroded parts of all the CW curves coincide with each other and also with the CW curve of the virgin sample [91]. The onset of the corroded part shifted upwards with time because of an increase in the slag quantity with dissolution. The corroded parts of all the CW curves can be well distinguished and do not coincide. The corroded sample radius and length decrease with the dissolution time, and for a particular dissolution time, the decrease was greater with increasing temperature [91]. At a particular temperature and dissolution time, the decreases of radius and length are higher in S1 slag, may be because of relatively lower viscosity. In all cases, there is no Marangoni groove at the triple points (refractory/slag/atmosphere). Reynolds numbers are sufficiently high for the dynamic experiments with 200 rpm to suppress the Marangoni convection. At 1500 and 1550 °C in S1 and 1550 °C in S2, the reductions of radius at the middle of the corroded part are less compared to other parts.

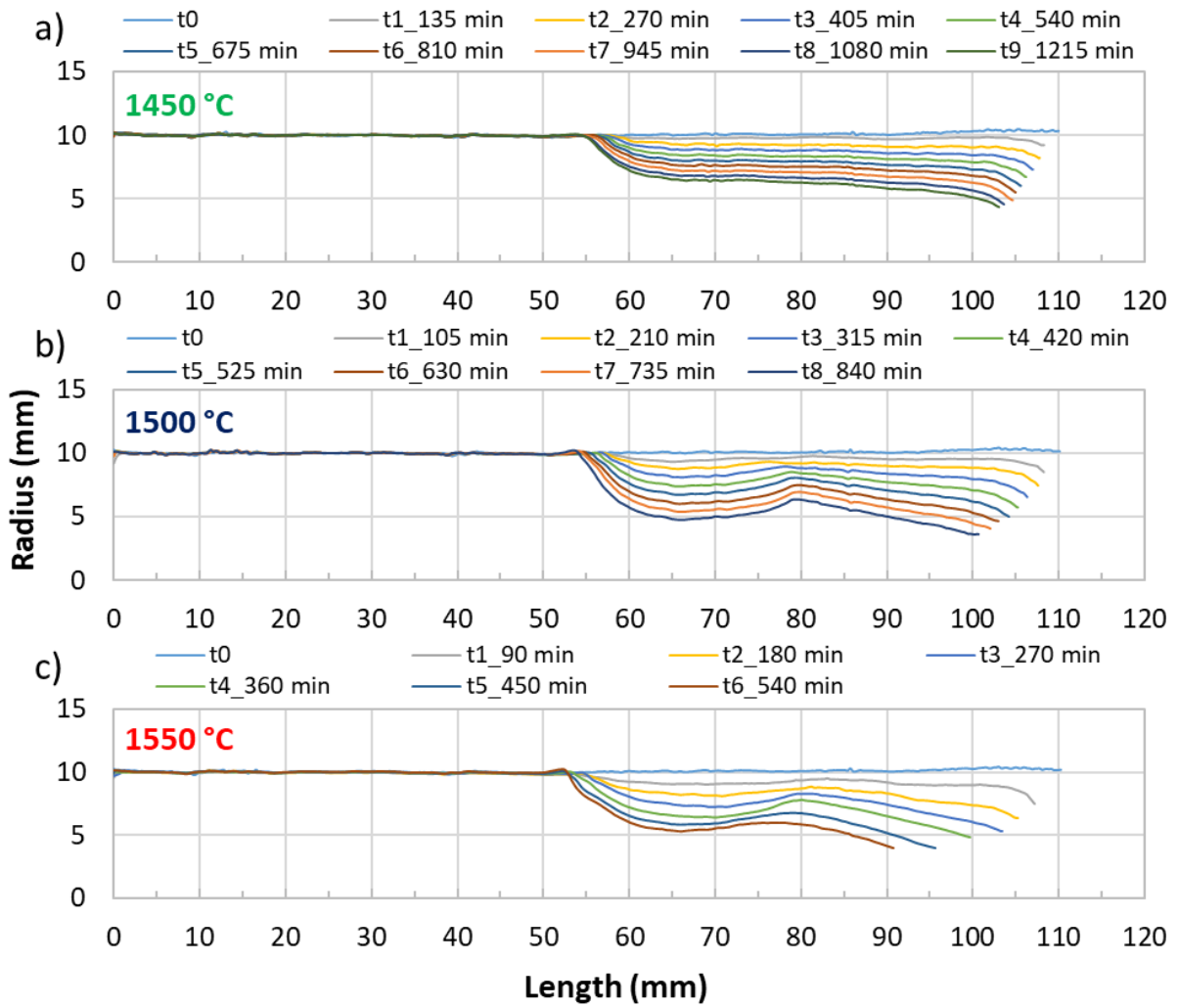


Figure 39: a), b) and c) CW curves for alumina dissolution with 200 rpm in S1 slag at 1450, 1500 and 1550 °C respectively [91].

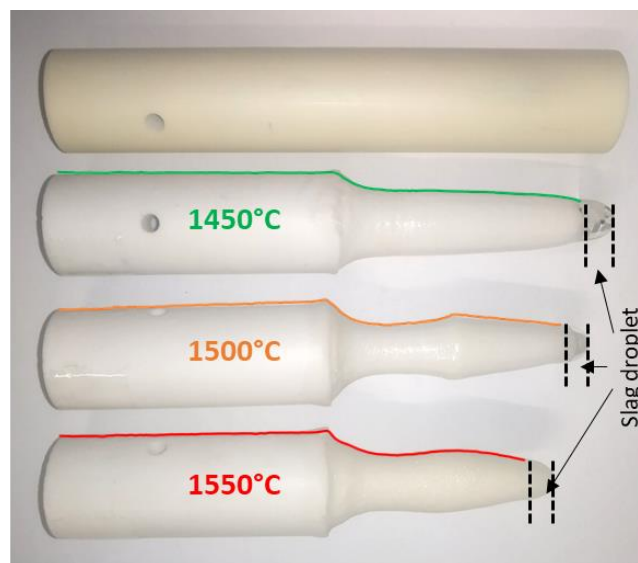


Figure 40: Virgin and corroded samples with inserted CW curves of last steps of alumina dissolution with 200 rpm in S1 slag [91].



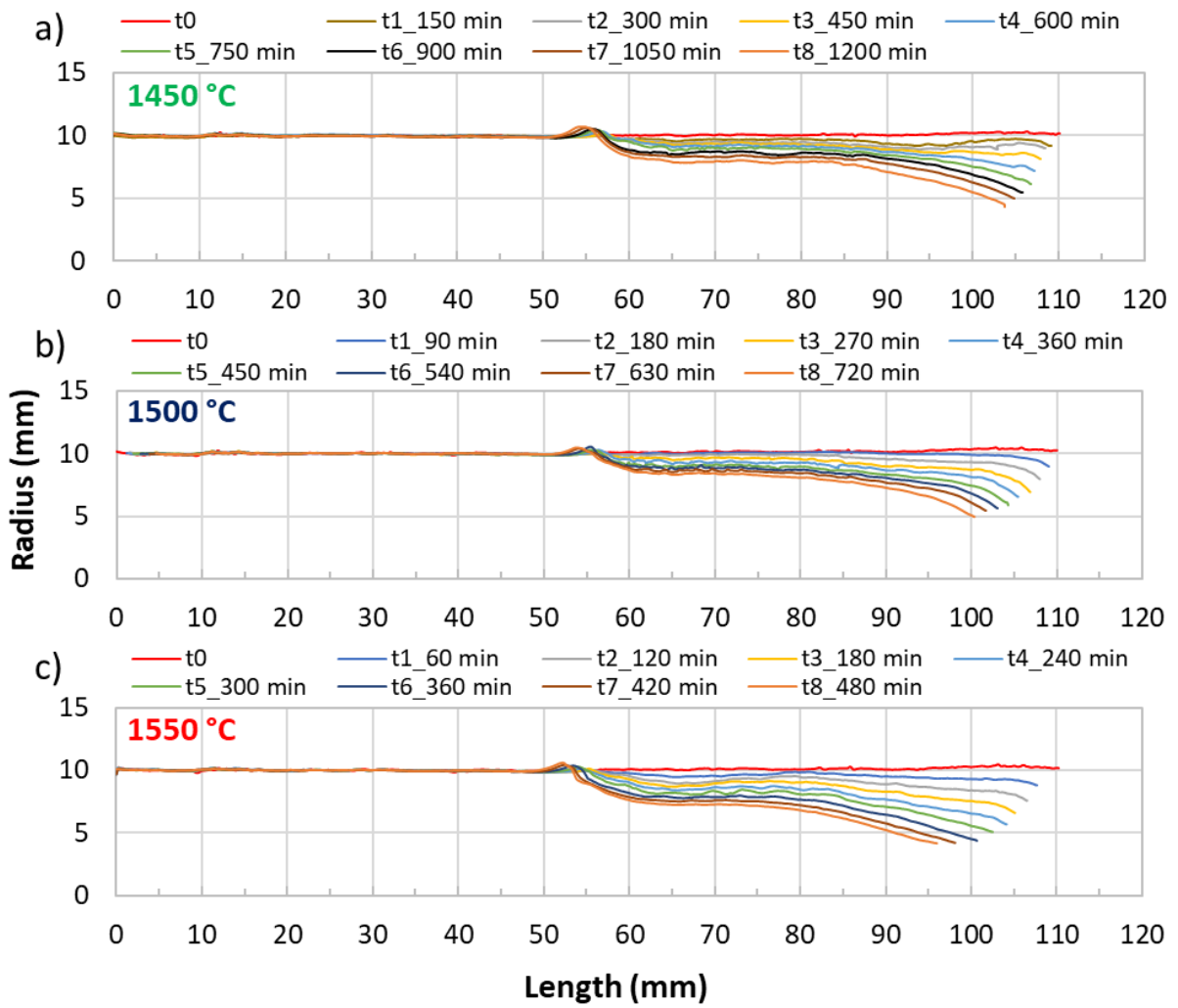


Figure 41: a), b) and c) CW curves for alumina dissolution with 200 rpm in S2 slag at 1450, 1500 and 1550 °C respectively.

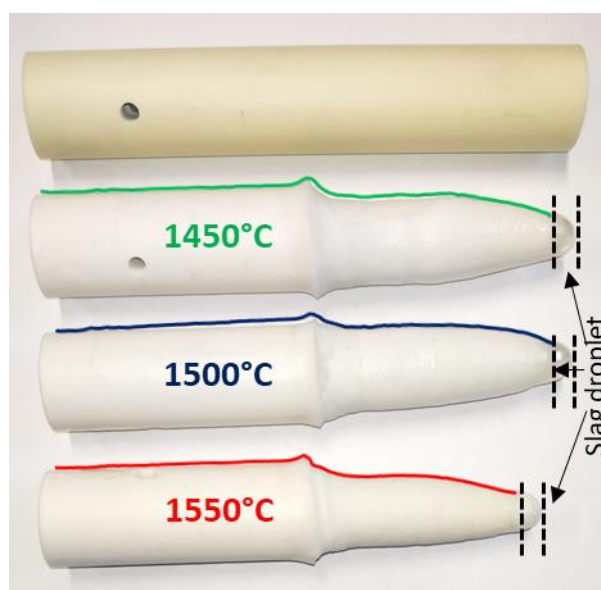
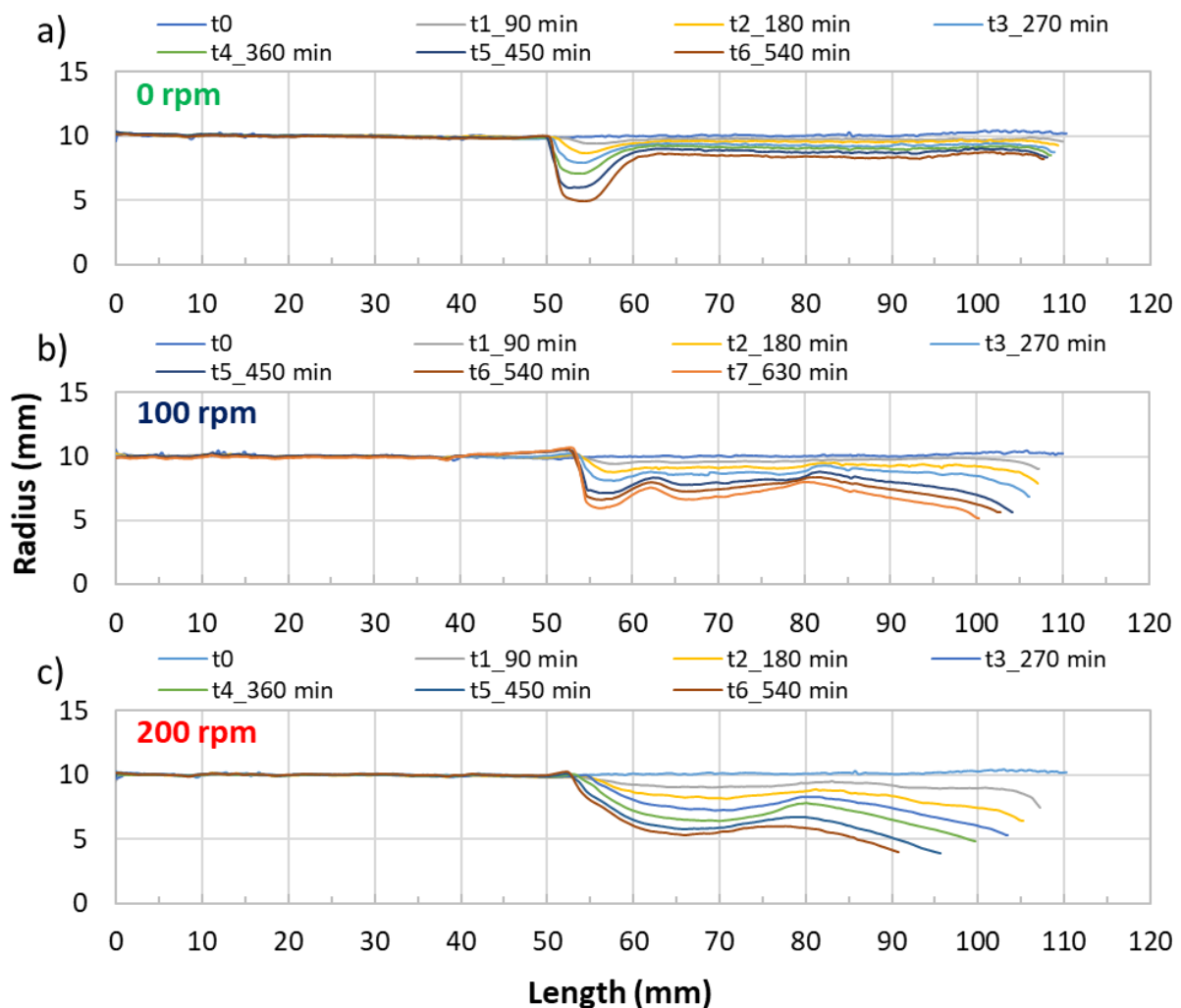


Figure 42: Virgin and corroded samples with inserted CW curves of last steps of alumina dissolution with 200 rpm in S2 slag.

Effect of rotational speed on the dissolution of alumina was studied at 1550 °C in both slags. **Figure 43** a)-c) show the CW curves in S1 with 0, 100 and 200 rpm, respectively. The CW curves in S2 with 0, 100 and 200 rpm are represented by **Figure 45** a)-c), respectively. Marangoni grooves are observed at the triple points for the experiments with 0 and 100 rpm. **Figure 44** and **Figure 46** show the virgin and corroded alumina samples in S1 and S2 slags, respectively, with different rpm at 1550 °C. The CW curves for the last corrosion steps show good agreement with corroded sample shape. Grooves are more pronounced in case of S1 slag, may be because of lower viscosity. Groove depth is the highest for the static experiment in S1 for a specified dissolution time. At a particular rotational speed and time, dissolution of alumina is higher in S1. At lower rotational speed the corroded sample surfaces are more uneven. Reduction of corroded sample radius and length increases with rising rotational speed.



**Figure 43:** a), b) and c) CW curves for alumina dissolution at 1550 °C in S1 slag with 0, 100 and 200 rpm respectively.

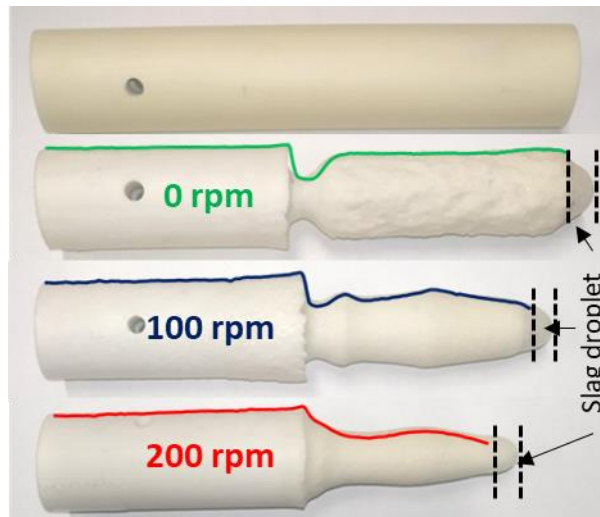


Figure 44: Virgin and corroded samples with inserted CW curves of last steps of alumina dissolution at 1550°C in S1 slag.

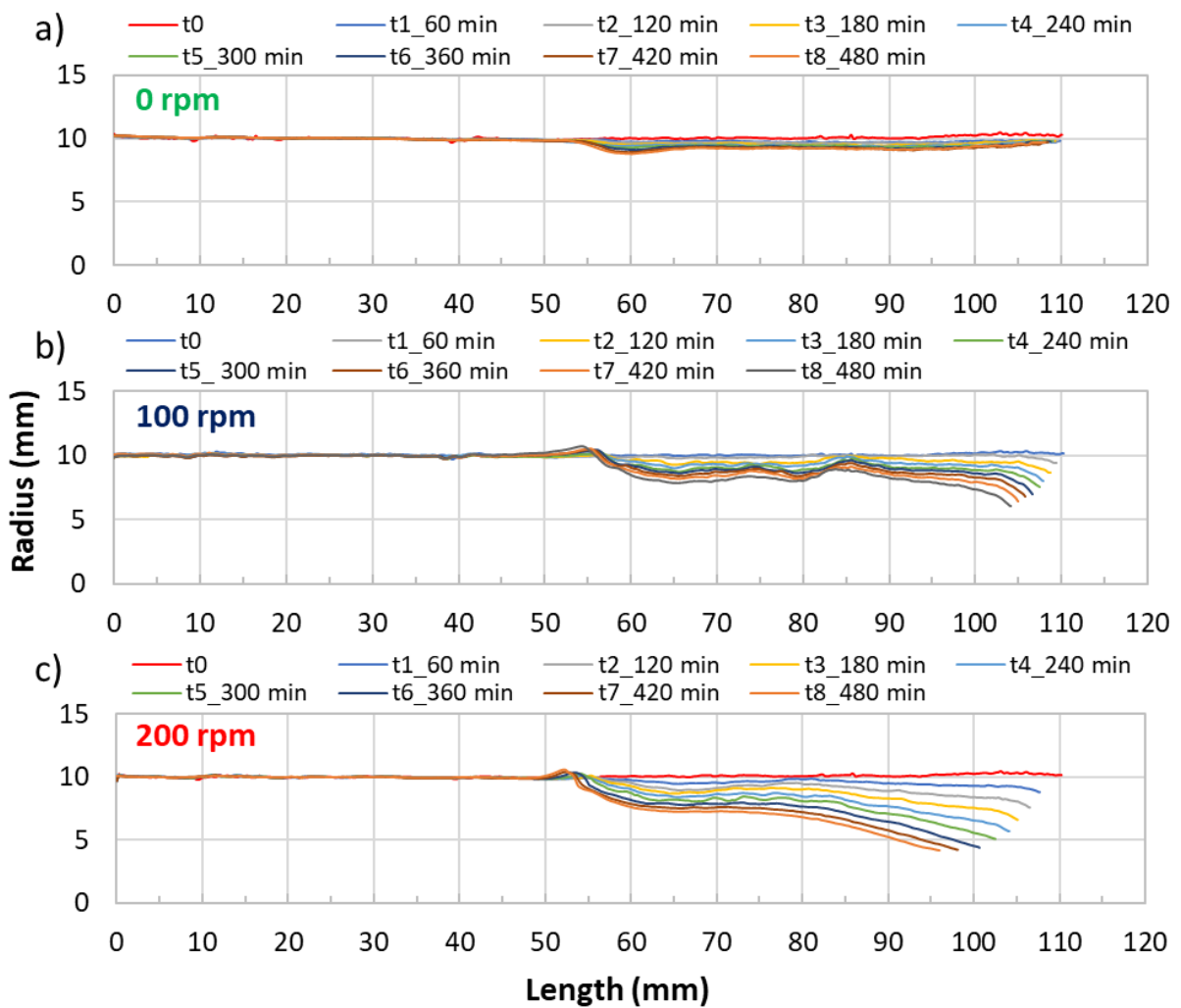
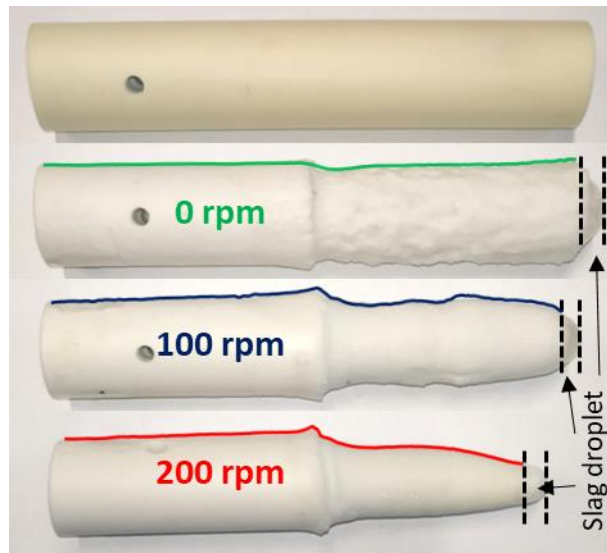


Figure 45: a), b) and c) CW curves for alumina dissolution at 1550 °C in S2 slag with 0, 100 and 200 rpm respectively.



**Figure 46: Virgin and corroded samples with inserted CW curves of last steps of alumina dissolution at 1550°C in S2 slag.**

### 5.3.2. Dissolution parameters

The dissolution parameters, namely corroded volume, surface area, mean radius, tip radius, and immersion length were extracted from the CW curves [91]. As these parameters were determined from the CW curves, they are expected to be more accurate than the manual measurements of the post-mortem analysis [91]. The intersection point of the initial curve of the un-corroded sample and the actual CW curve defines the onset for the corroded part. The immersion length is defined from the sample tip to the onset of the corroded part. The remaining volume and mantle surface area were determined by integration along the immersion length. The area of the disc shape tip was added to get the total surface area. The mean radius along the immersion length was used as the representative cylinder radius for the diffusivity determination and is larger than the tip radius [91].

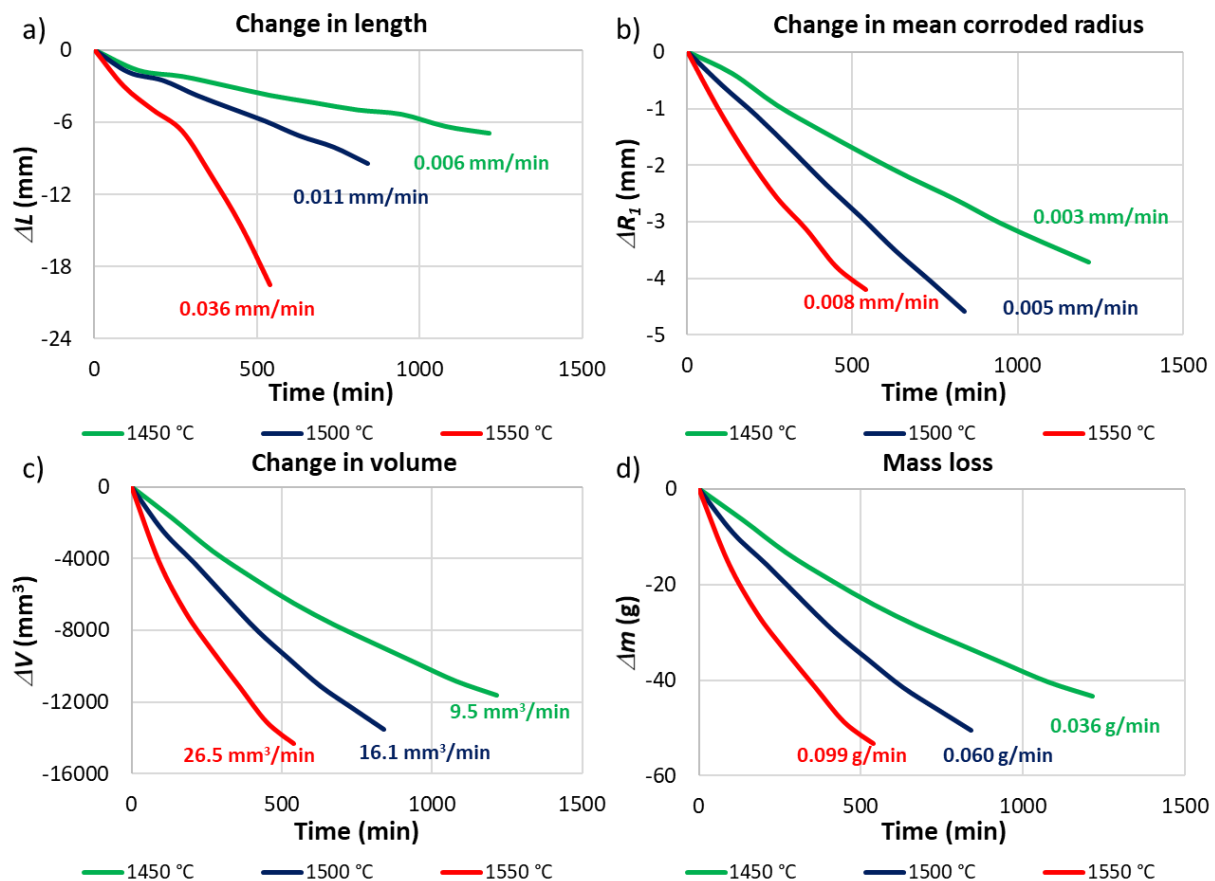


**Figure 47:** a), b), c) and d) change in length, mean corroded radius, volume and mass, respectively, for alumina dissolution in S1 slag with 200 rpm at 1450, 1500 and 1550 °C. The numbers inserted give the average rate of change over the total dissolution time [91].

The change in the sample length, mean corroded radius, volume, and mass over dissolution time are represented in **Figure 47** a)-d) [91], respectively, for alumina dissolution in S1 slag with 200 rpm at 1450, 1500 and 1550 °C. The effect of temperature on the dissolution is clearly visible in the diagrams. All these parameters increased in their absolute value with the rising experimental temperature, because of lower slag viscosity and larger solubility limit at higher temperature. The average rates of change in the mean corroded radius, volume, and mass increase 1.6–1.7 times with an increase in temperature from 1450 °C to 1500 °C and 1500 °C to 1550 °C. The average rate of change in the sample length increases 3.27 times with an increase in temperature from 1500 °C to 1550 °C, contrary to the 1.83 times increase for the temperature rise from 1450 °C to 1500 °C [91]. The higher average rate of change in length at 1550 °C may have occurred because of the faster dissolution of the relatively thinner sample (compared to sample thickness at lower temperatures), especially at the ending steps in the low viscosity slag [91]. A slightly decreasing slope or almost linear trend of the dissolution parameters indicates a quasi-steady dissolution [91].

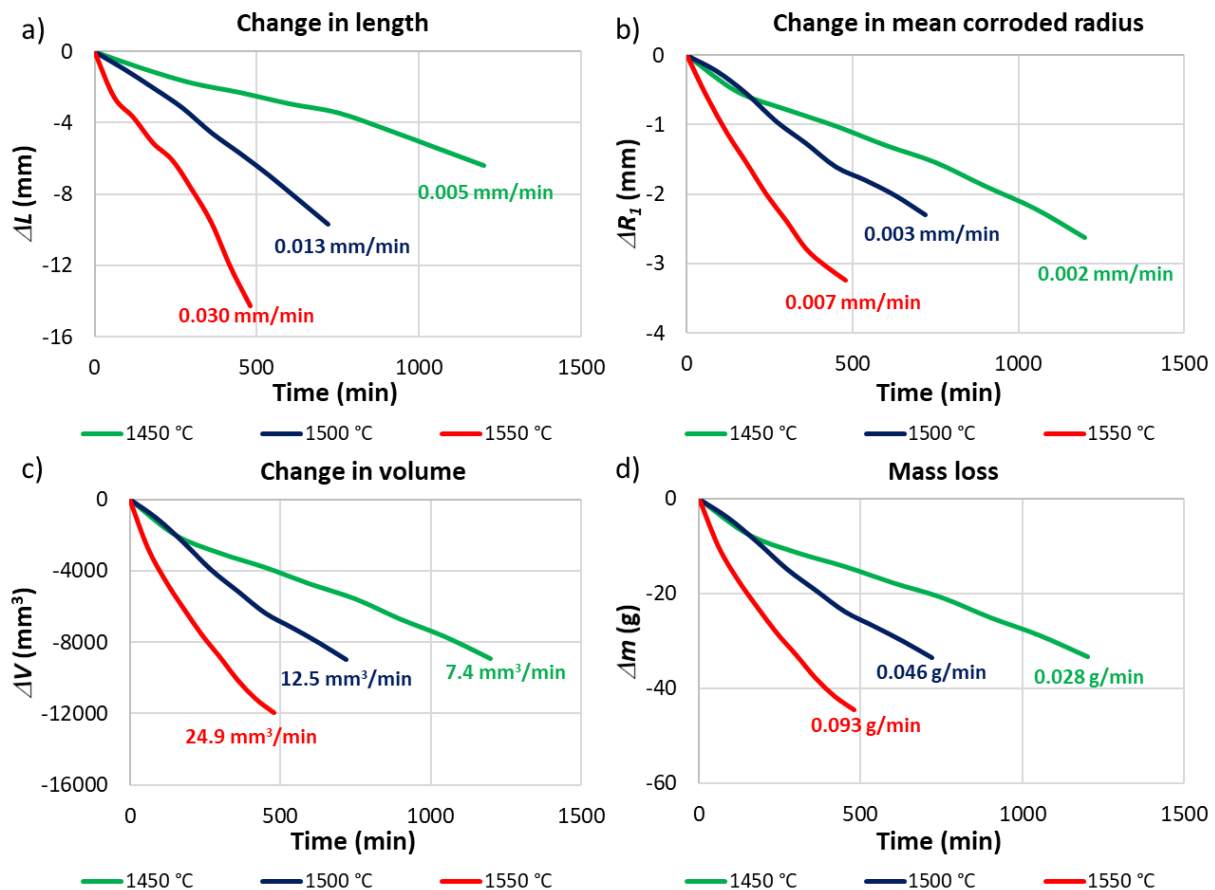


**Figure 48:** a), b), c) and d) change in length, mean corroded radius, volume and mass, respectively, for alumina dissolution in S2 slag with 200 rpm at 1450, 1500 and 1550 °C. The numbers inserted give the average rate of change over the total dissolution time.

The change in the sample length, mean corroded radius, volume, and mass over dissolution time are represented in **Figure 48** a)-d), respectively, for alumina dissolution in S2 slag with 200 rpm at 1450, 1500 and 1550 °C. In this case also, all these parameters increased in their absolute value with the rising experimental temperature, because of the same reasons mentioned for S1. The average rates of change in the mean corroded radius, volume, and mass increase 1.5–1.7 times and 2.0–2.3 times with an increase in temperature from 1450 °C to 1500 °C and 1500 °C to 1550 °C, respectively. The average rate of change in the sample length increases 2.6 times and 2.3 times with an increase in temperature from 1450 °C to 1500 °C and 1500 °C to 1550 °C, respectively. Here also, a slightly decreasing slope or almost linear trend of the dissolution parameters indicates a quasi-steady dissolution. Average rates of change of all of these dissolution parameters at a particular temperature are higher in S1.

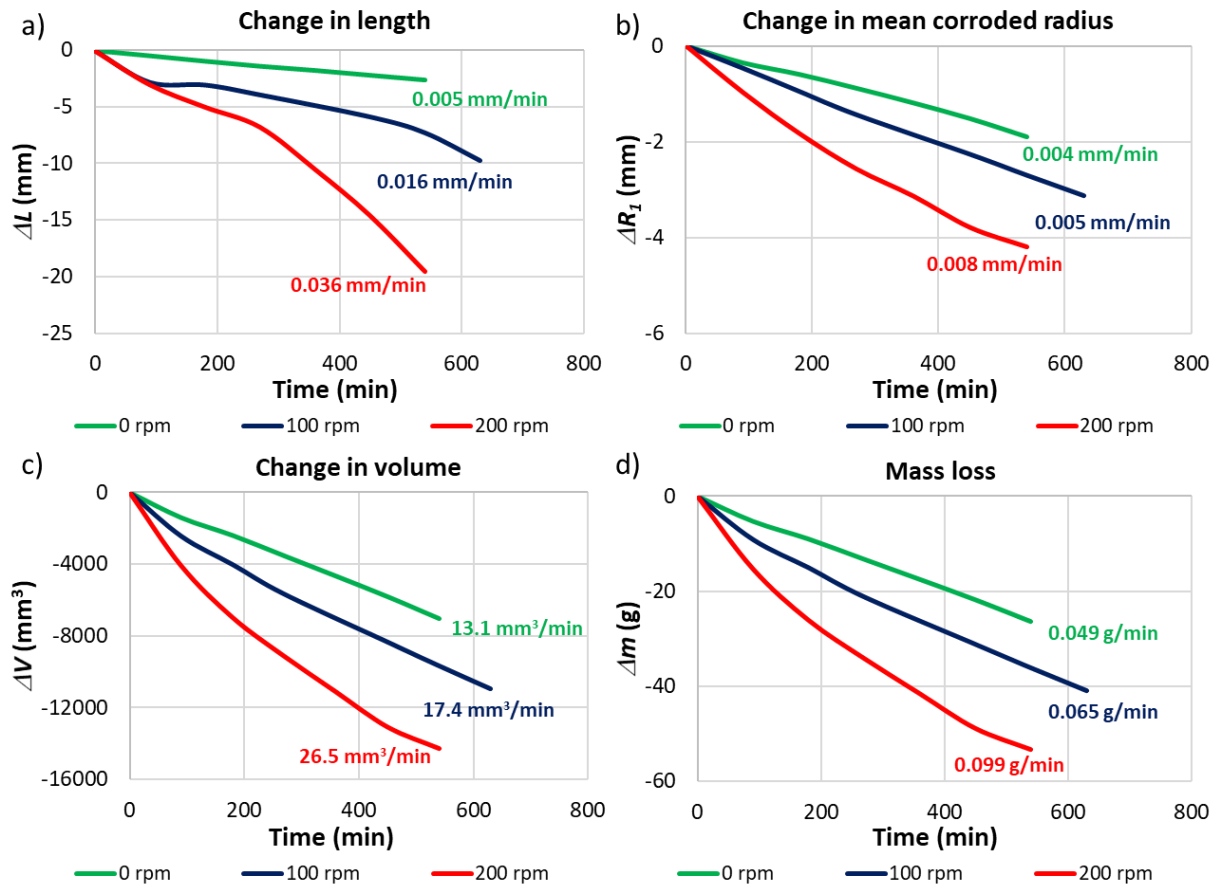


**Figure 49:** a), b), c) and d) change in length, mean corroded radius, volume and mass, respectively, for alumina dissolution in S1 slag at 1550 °C with 0, 100 and 200 rpm. The numbers inserted give the rate of change over the total dissolution time.

The effect of rotational speed on change in the sample length, mean corroded radius, volume, and mass over dissolution time were studied and are represented in **Figure 49** a)-d), respectively, for alumina dissolution in S1 slag at 1550 °C with 0, 100 and 200 rpm. All these parameters increased in their absolute value with the rising rotational speed, because of higher mass transfer through thinner effective boundary layer at higher speed and this confirms that the dissolution is a diffusion controlled process. The average rates of change in the mean corroded radius, volume, and mass increase 1.25–1.33 times and 1.52–1.60 times with an increase in rotational speed from 0 to 100 rpm and 100 to 200 rpm respectively. The average rate of change in the sample length increases 3.2 times and 2.25 times with an increase in rotational speed from 0 to 100 rpm and 100 to 200 rpm respectively.

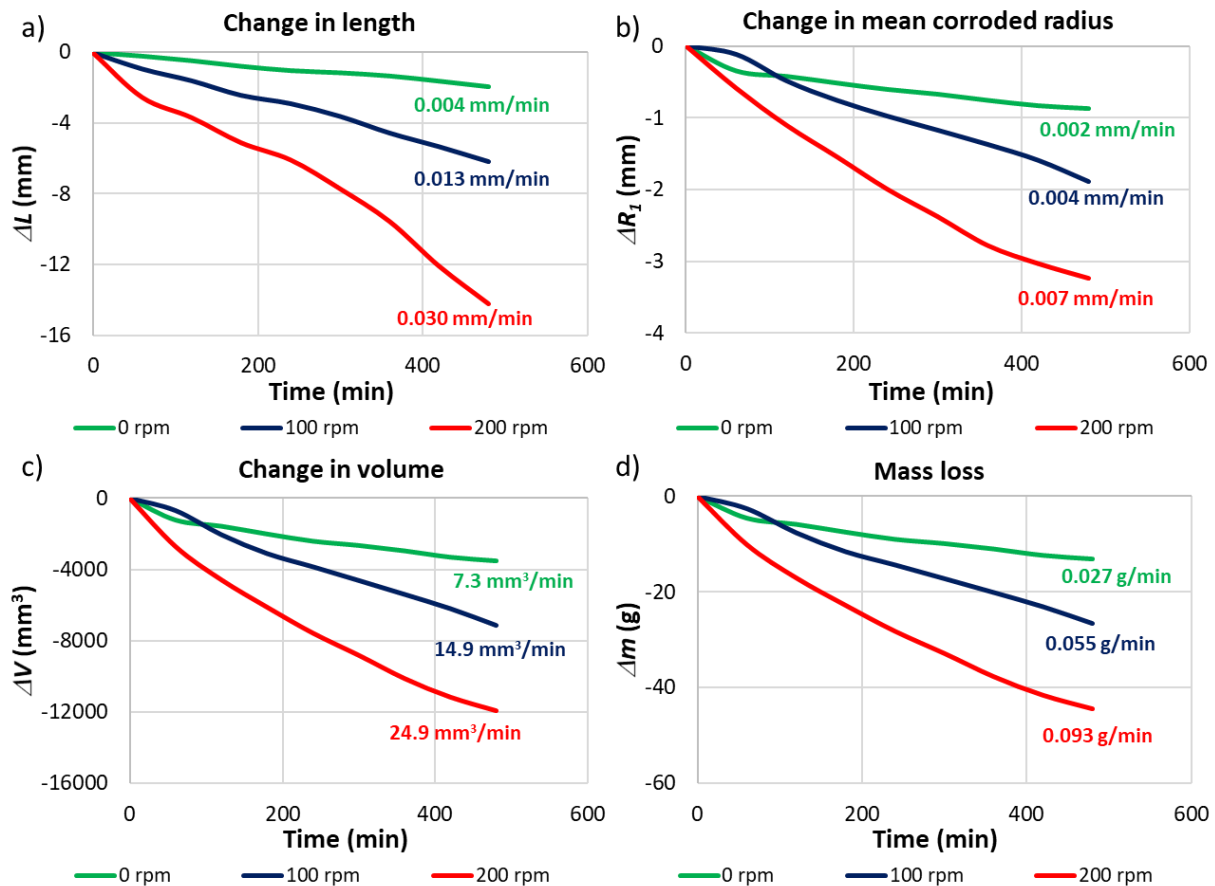


**Figure 50:** a), b), c) and d) change in length, mean corroded radius, volume and mass, respectively, for alumina dissolution in S2 slag at 1550 °C with 0, 100 and 200 rpm. The numbers inserted give the average rate of change over the total dissolution time.

The effect of rotational speed on change in the sample length, mean corroded radius, volume, and mass over dissolution time were studied also for alumina in S2 slag at 1550 °C with 0, 100 and 200 rpm and which are represented in **Figure 50** a)-d), respectively. Here also, all these parameters increased in their absolute value with the rising rotational speed, because of higher mass transfer through thinner effective diffusive boundary layer at higher speed. The average rates of change in the mean corroded radius, volume, and mass increase 2.0 times and 1.7 times with an increase in rotational speed from 0 to 100 rpm and 100 to 200 rpm, respectively. The average rate of change in the sample length increases 3.25 times and 2.3 times with an increase in rotational speed from 0 to 100 rpm and 100 to 200 rpm, respectively. The average rates of change of these parameters at a specified rotational speed are higher in S1.



### 5.3.3. Diffusivity

The diffusivities for all the steps of dynamic corrosion experiments with 200 rpm were calculated with equation (45) using the dissolution parameters extracted from the CW curves [91]. These parameters for individual corrosion step ( $c$ ) are listed in **Table 11** for alumina dissolution in S1 with 200 rpm at 1450, 1500 and 1550 °C [91]. The mean sample radius, tip radius, and immersion length continuously decrease with the dissolution time. Whereas the bulk concentration of alumina and slag viscosity increase with the alumina dissolution. **Figure 51 a)** represents the diffusivities ( $D_c$  and  $D_{0,c}$ ) of alumina for all the corrosion steps at three temperatures in S1 slag with 200 rpm. The diffusivity increases with rising temperature. The Arrhenius plot was produced with the diffusivities ( $D_{0,c}$ ) of those corresponding corrosion steps  $c_T$  (corrosion step  $c$  at temperature  $T$ ) which show a similar mass, relative to the initial mass, at different temperatures. The diffusivities received are functions of temperature and slag composition, which changes during dissolution [91]. For the Arrhenius plot, the diffusivities were converted to those of the virgin slag composition using the Stokes-Einstein relation that defines the product of diffusivity and viscosity to be constant [91]. This conversion eliminates the composition influence, else the alumina content of slag would have been another parameter. **Figure 51 b)** represents the Arrhenius plot which shows a linear tendency, thereby confirming the plausibility of diffusivities. The test intervals used for the Arrhenius plots together with the associated mass loss, bulk concentrations of alumina and the corresponding activation energies are tabulated in **Table 12**. The linear fit is better when the mass losses of the corrosion steps are comparable. The activation energy of diffusion decreases with increasing mass loss and bulk concentration.

**Table 11: Dissolution parameters used for diffusivity calculation of alumina in S1 slag at 1450, 1500 and 1550 °C with 200 rpm [91].**

Temperature	Corrosion step, $c$	Mean sample radius, $R_{1,c-1/2}$ (m)	Tip radius, $R_{t,c-1/2}$ (m)	Bulk concentration, $W_{0,c-1/2}$ (wt%/100)	Viscosity, $\eta_{c-1/2}$ (Pas)	Immersion length, $l_{c-1/2}$ (m)	Mass flux density, $j_{c-1/2}$ (kg/m <sup>2</sup> s)
1450 °C	1	0.00997	0.00979	0.11654	1.0448	0.05090	0.000229709
	2	0.00949	0.00873	0.12656	1.0949	0.05000	0.000263853
	3	0.00899	0.00777	0.13573	1.1422	0.04985	0.000232004
	4	0.00854	0.00702	0.14353	1.1863	0.04974	0.000228111
	5	0.00813	0.00638	0.15038	1.2263	0.04960	0.000208675
	6	0.00774	0.00578	0.15625	1.2603	0.04935	0.000195567
	7	0.00734	0.00521	0.16164	1.2958	0.04917	0.000206012
	8	0.00695	0.00473	0.16689	1.3302	0.04904	0.000215812
	9	0.00660	0.00447	0.17142	1.3585	0.04869	0.000175272
1500 °C	1	0.00984	0.00933	0.11859	0.7495	0.05186	0.000419619
	2	0.00927	0.00799	0.13043	0.7885	0.05074	0.000337636
	3	0.00871	0.00700	0.14048	0.8227	0.05001	0.000393276
	4	0.00810	0.00614	0.15046	0.8602	0.04927	0.000420668
	5	0.00751	0.00537	0.15934	0.8949	0.04886	0.000391632
	6	0.00692	0.00483	0.16719	0.9275	0.04832	0.000417434
	7	0.00636	0.00436	0.17400	0.9565	0.04771	0.000369672
	8	0.00582	0.00384	0.17990	0.9827	0.04701	0.000406564
1550 °C	1	0.00967	0.00883	0.12317	0.5533	0.05486	0.000791799
	2	0.00875	0.00693	0.14222	0.5969	0.05198	0.000666008
	3	0.00795	0.00587	0.15546	0.6297	0.04967	0.000578386
	4	0.00729	0.00509	0.16602	0.6576	0.04744	0.000613556
	5	0.00669	0.00438	0.17584	0.6850	0.04451	0.000709582
	6	0.00615	0.00395	0.18354	0.7081	0.04037	0.000523108

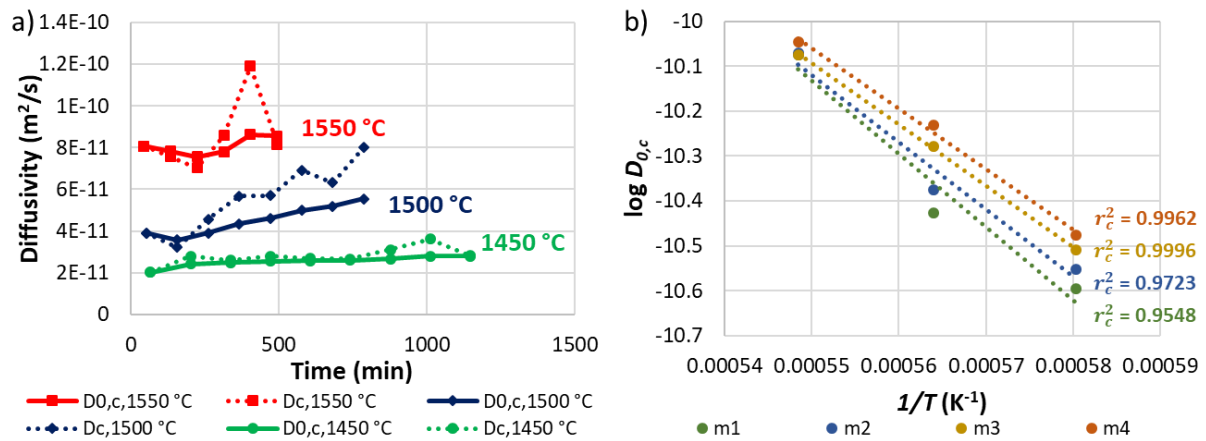


**Figure 51:** a) Diffusivity of alumina in S1 slag at 1450, 1500 and 1550 °C with 200 rpm b) Arrhenius plot of diffusivities of alumina in S1 slag with 200 rpm [91].

**Table 12:** Test intervals as applied for Arrhenius plot with associated mass loss, bulk concentrations of alumina and corresponding activation energies for alumina in S1 slag with 200 rpm.

Mass loss (g)	Bulk concentration (wt%/100)	Corresponding corrosion steps, $c_T$	Activation Energy (kJ/mol)
m1	14.9±1.33	2 <sub>1450 °C</sub> ; 2 <sub>1500 °C</sub> ; 1 <sub>1550 °C</sub>	313
m2	24.5±1.53	4 <sub>1450 °C</sub> ; 3 <sub>1500 °C</sub> ; 2 <sub>1550 °C</sub>	288
m3	35.5±1.25	7 <sub>1450 °C</sub> ; 5 <sub>1500 °C</sub> ; 3 <sub>1550 °C</sub>	262
m4	42.5±0.90	9 <sub>1450 °C</sub> ; 6 <sub>1500 °C</sub> ; 4 <sub>1550 °C</sub>	259

The dissolution parameters for alumina dissolution in S2 with 200 rpm at 1450, 1500 and 1550 °C are tabulated in **Table 13**. Here also, the mean sample radius, tip radius, and immersion length continuously decrease with the dissolution time. Whereas the bulk concentration of alumina and slag viscosity increase with the alumina dissolution. **Figure 52 a)** represents the diffusivities ( $D_c$  and  $D_{0,c}$ ) of alumina for all the corrosion steps at three experimental temperatures in S2 slag with 200 rpm. In this case also, the diffusivity increases with rising temperature. The very beginning step at 1500°C shows lower diffusivity, may be because of unsteady state when dissolution starts and reaction layer formation during slag dropping time after the corrosion step which leads to the measurement of lower corrosion depth. Afterwards, this reaction layer would have been dissolved at the beginning of next corrosion step and quasi-steady state was achieved. The Arrhenius plot was produced as discussed in case of alumina dissolution in S1 slag. **Figure 52 b)** represents the Arrhenius plot of alumina diffusivities in S2 slag with 200 rpm and the plausibility of diffusivities is confirmed by the linear tendency of the Arrhenius plot. The test intervals used for the Arrhenius plots together with the associated mass loss, bulk concentrations of alumina and the corresponding activation energies are tabulated in **Table 14**. The activation energy of diffusion decreases with increasing mass loss and bulk concentration. Diffusivities of alumina are higher for the dissolution in S1 compared to S2.

**Table 13: Dissolution parameters used for diffusivity calculation of alumina in S2 slag at 1450, 1500 and 1550 °C with 200 rpm.**

Temperature	Corrosion step, $c$	Mean sample radius, $R_{1,c-1/2}$ (m)	Tip radius, $R_{t,c-1/2}$ (m)	Bulk concentration, $W_{0,c-1/2}$ (wt%/100)	Viscosity, $\eta_{c-1/2}$ (Pas)	Immersion length, $l_{c-1/2}$ (m)	Mass flux density, $j_{c-1/2}$ (kg/m <sup>2</sup> s)
1450 °C	1	0.00987	0.00969	0.21500	1.3721	0.05238	0.000231587
	2	0.00947	0.00909	0.22248	1.4362	0.05165	0.000128688
	3	0.00922	0.00856	0.22697	1.4772	0.05069	0.000104679
	4	0.00897	0.00765	0.23116	1.5155	0.04978	0.000129327
	5	0.00870	0.00667	0.23538	1.5558	0.04953	0.000121398
	6	0.00841	0.00583	0.24004	1.6011	0.04913	0.000174978
	7	0.00808	0.00526	0.24502	1.6525	0.04838	0.000163322
	8	0.00771	0.00464	0.25013	1.7046	0.04771	0.000214699
1500 °C	1	0.01008	0.00962	0.21269	0.9271	0.05339	0.000200001
	2	0.00981	0.00847	0.21878	0.9592	0.05210	0.000274607
	3	0.00945	0.00745	0.22585	0.9974	0.05063	0.000327908
	4	0.00909	0.00675	0.23244	1.0354	0.04914	0.000285098
	5	0.00876	0.00622	0.23821	1.0700	0.04799	0.000303372
	6	0.00850	0.00577	0.24299	1.0993	0.04729	0.000217864
	7	0.00829	0.00555	0.24689	1.1242	0.04632	0.000235736
	8	0.00804	0.00521	0.25100	1.1505	0.04522	0.000275129
1550 °C	1	0.00986	0.00949	0.21683	0.6652	0.05301	0.000787979
	2	0.00930	0.00820	0.22810	0.7045	0.05120	0.000604934
	3	0.00882	0.00710	0.23629	0.7354	0.04999	0.000547042
	4	0.00837	0.00616	0.24333	0.7624	0.04921	0.000558788
	5	0.00796	0.00539	0.24957	0.7877	0.04828	0.000519282
	6	0.00756	0.00474	0.25538	0.8118	0.04677	0.000596967
	7	0.00724	0.00431	0.26066	0.8335	0.04523	0.000519916
	8	0.00701	0.00420	0.26466	0.8514	0.04350	0.000406874

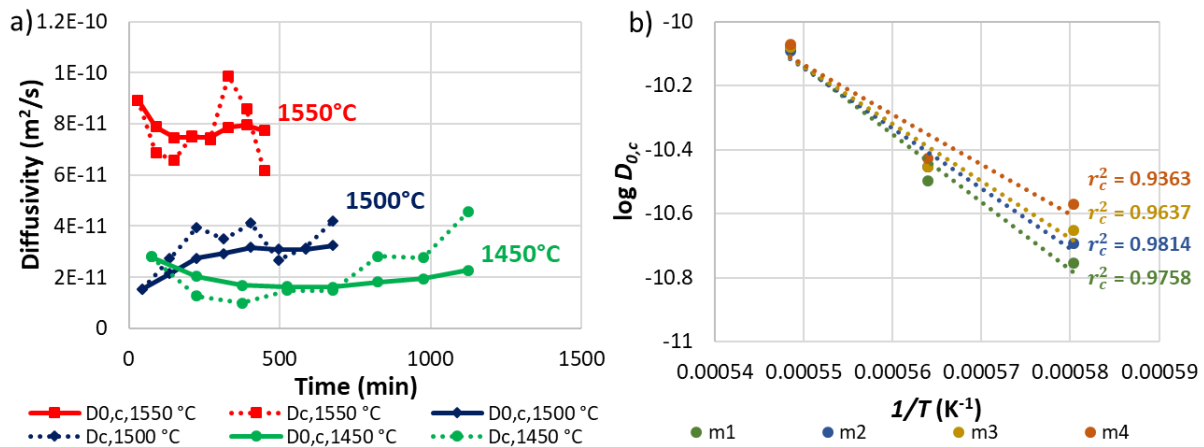


Figure 52: a) Alumina diffusivity in S2 slag at 1450, 1500 and 1550 °C with 200 rpm b) Arrhenius plot of alumina diffusivity in S2 slag with 200 rpm.

Table 14: Test intervals as applied for Arrhenius plot with associated mass loss, bulk concentrations of alumina and corresponding activation energies for alumina in S2 slag with 200 rpm.

Mass loss (g)		Bulk concentration (wt%/100)	Corresponding corrosion steps, $c_T$	Activation Energy (kJ/mol)
m1	18.0±1.10	0.231±0.0022	4 <sub>1450 °C</sub> ; 4 <sub>1500 °C</sub> ; 2 <sub>1550 °C</sub>	406
m2	23.9±1.11	0.238±0.0019	6 <sub>1450 °C</sub> ; 5 <sub>1500 °C</sub> ; 3 <sub>1550 °C</sub>	360
m3	29.0±0.89	0.245±0.0018	7 <sub>1450 °C</sub> ; 7 <sub>1500 °C</sub> ; 4 <sub>1550 °C</sub>	342
m4	33.2±0.30	0.250±0.0007	8 <sub>1450 °C</sub> ; 8 <sub>1500 °C</sub> ; 5 <sub>1550 °C</sub>	299

#### 5.4. Dissolution studies of magnesia fine ceramics in CWTD

Dynamic corrosion experiments of magnesia fine ceramics were carried out in S1 and S2 slags in ambient atmosphere. Dynamic experiments with 200 rpm were conducted at 1450, 1500 and 1550 °C to study the effect of temperature on dissolution. **Table 15** and **Table 16** show the test conditions for CWTD experiments of magnesia fine ceramics in S1 and S2 slags, respectively. Bottom clearance was measured at room temperature (RT) at the beginning of the experiments, and this will increase with dissolution time. Marangoni grooves were observed at even 200 rpm experiments, therefore rotational speed was not decreased. It was not possible to complete the targeted number of corrosion steps except at 1450 °C in S1 slag, because of higher groove depth which may lead to sample fracture during experiment.

**Table 15: Test conditions for CWTD experiments of magnesia fine ceramics in S1.**

Target temperature (°C)	1450	1500	1550
Rotational speed (min <sup>-1</sup> )	200	200	200
Dropping time (min)	30	30	30
Corrosion time per step (min)	30	25	20
Number of corrosion steps targeted (1)	8	8	8
Bottom clearance at RT (mm)	23.0	23.0	23.0
Corrosion steps conducted (1)	8/8	7/8	4/8
Total corrosion time (min)	240	175	80

**Table 16: Test conditions for CWTD experiments of magnesia fine ceramics in S2.**

Target temperature (°C)	1450	1500	1550
Rotational speed (min <sup>-1</sup> )	200	200	200
Dropping time (min)	30	30	30
Corrosion time per step (min)	60	60	20
Number of corrosion steps targeted (1)	8	8	8
Bottom clearance at RT (mm)	22.5	22.5	22.5
Corrosion steps conducted (1)	7/8	4/8	6/8
Total corrosion time (min)	420	240	120

#### 5.4.1. CW curves for magnesia dissolution

Figure 53 a)-c) show the CW curves for the magnesia dissolution with 200 rpm in S1 slag at 1450, 1500 and 1550 °C respectively. CW curves for dynamic corrosion experiments with 200 rpm in S2 slag at 1450, 1500 and 1550 °C are shown in Figure 55 a)-c) respectively. Figure 54 and Figure 56 show the virgin and corroded magnesia samples in S1 and S2 slags, respectively, at all experimental temperatures with 200 rpm. Similar to the experiments with alumina, the CW curves for the last corrosion steps show good agreement with corroded sample shape. Here also, the un-corroded parts of all the CW curves coincide with each other and also with the CW curve of the virgin sample. The onset of the corroded part shifted towards the un-corroded part with time because of an increase in the slag quantity with dissolution [91]. The corroded parts of all the CW curves can be distinguished and do not coincide. The corroded sample radius and length decreased with the dissolution time, and for a particular dissolution time, the decrease was greater with increasing temperature. In all cases, there is a Marangoni groove at the triple points. The groove depth and width increase with rising temperature and dissolution time. Corrosion at the groove and sample tip is higher than at other locations. Dissolution rate in dependence of slag is related to experimental temperature. At 1450 °C dissolution is faster in S2, whereas it is reverse at 1550 °C and it is marginal at 1500 °C.

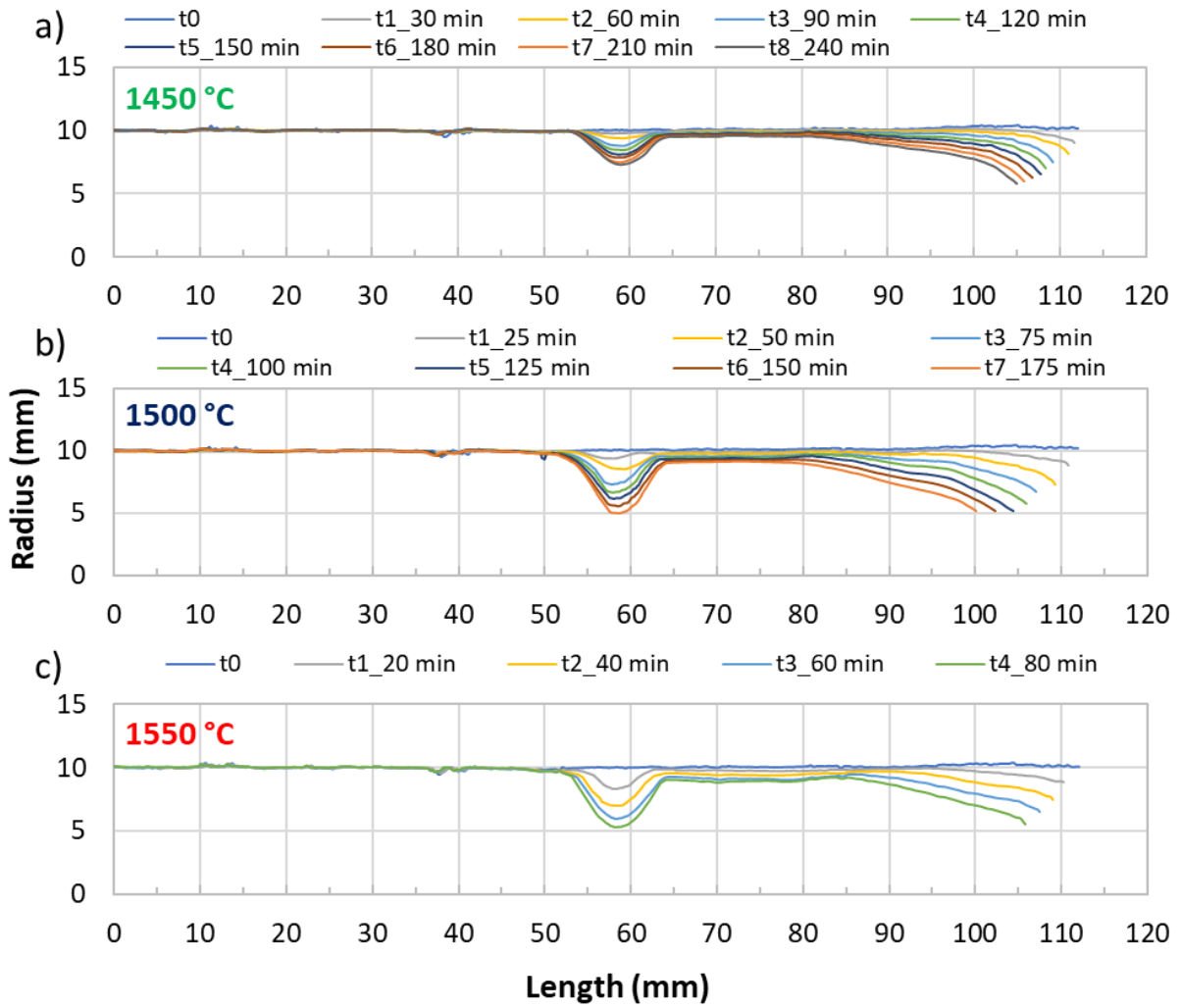


Figure 53: a), b) and c) CW curves for magnesia dissolution with 200 rpm in S1 slag at 1450, 1500 and 1550 °C respectively.

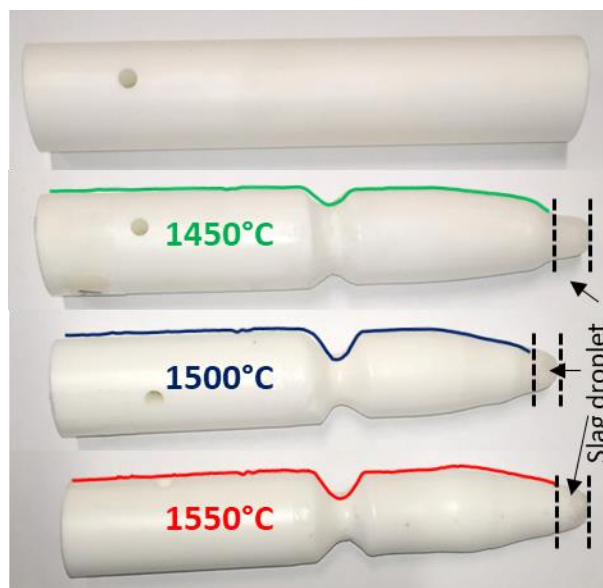


Figure 54: Virgin and corroded samples with inserted CW curves of last steps of magnesia dissolution with 200 rpm in S1 slag.

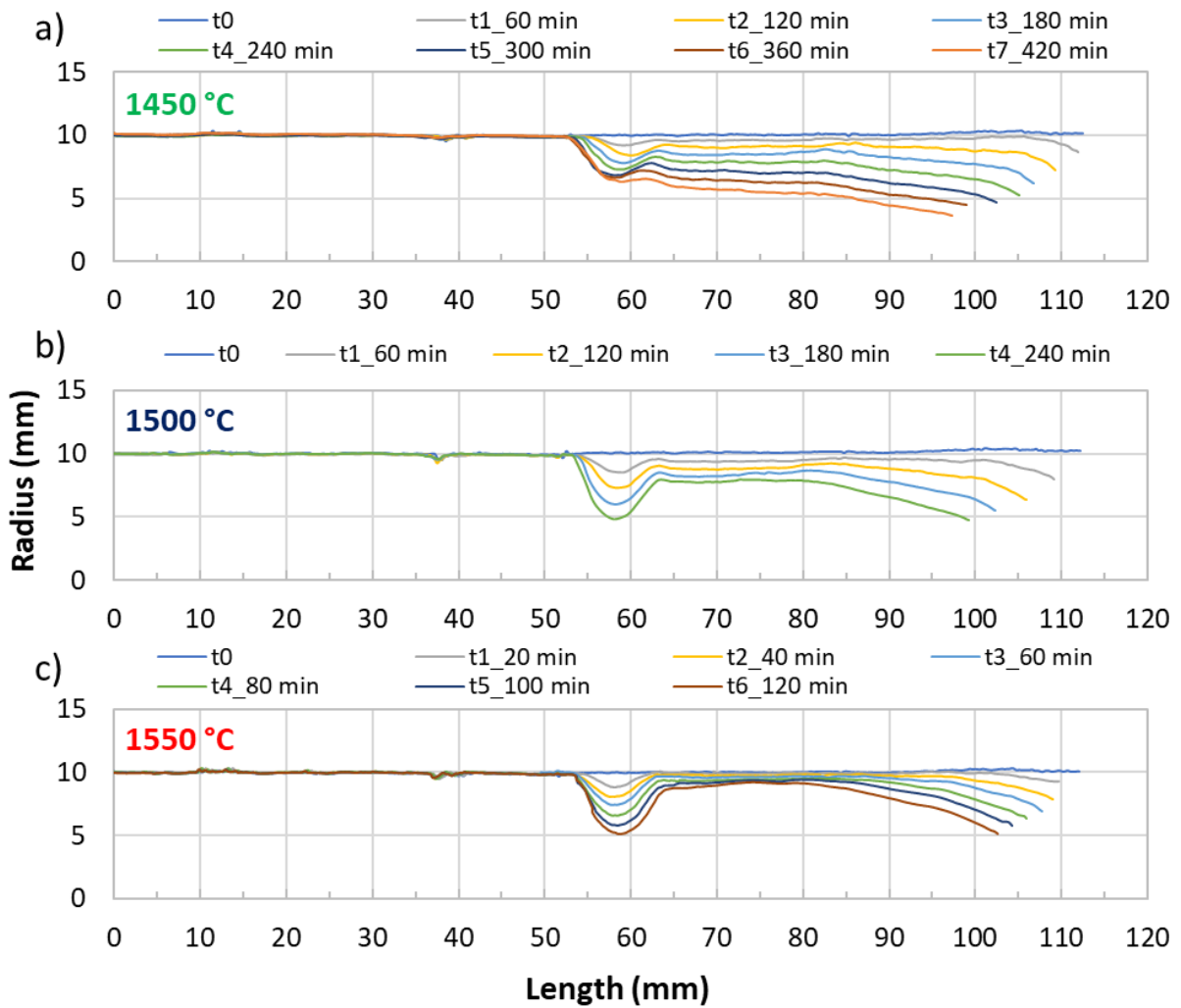


Figure 55: a), b) and c) CW curves for magnesia dissolution with 200 rpm in S2 slag at 1450, 1500 and 1550 °C respectively.

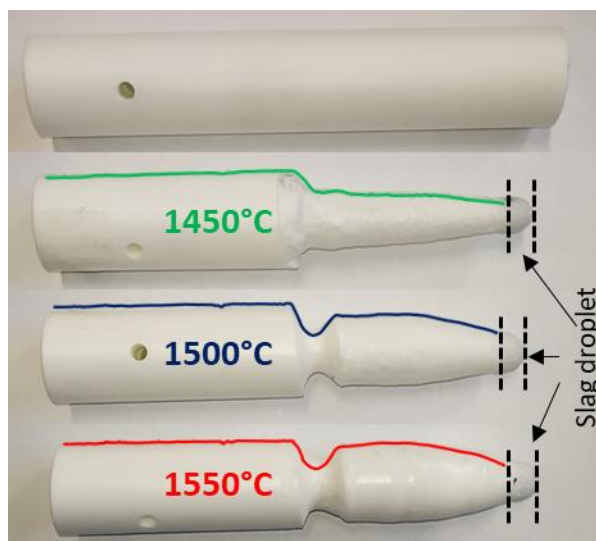
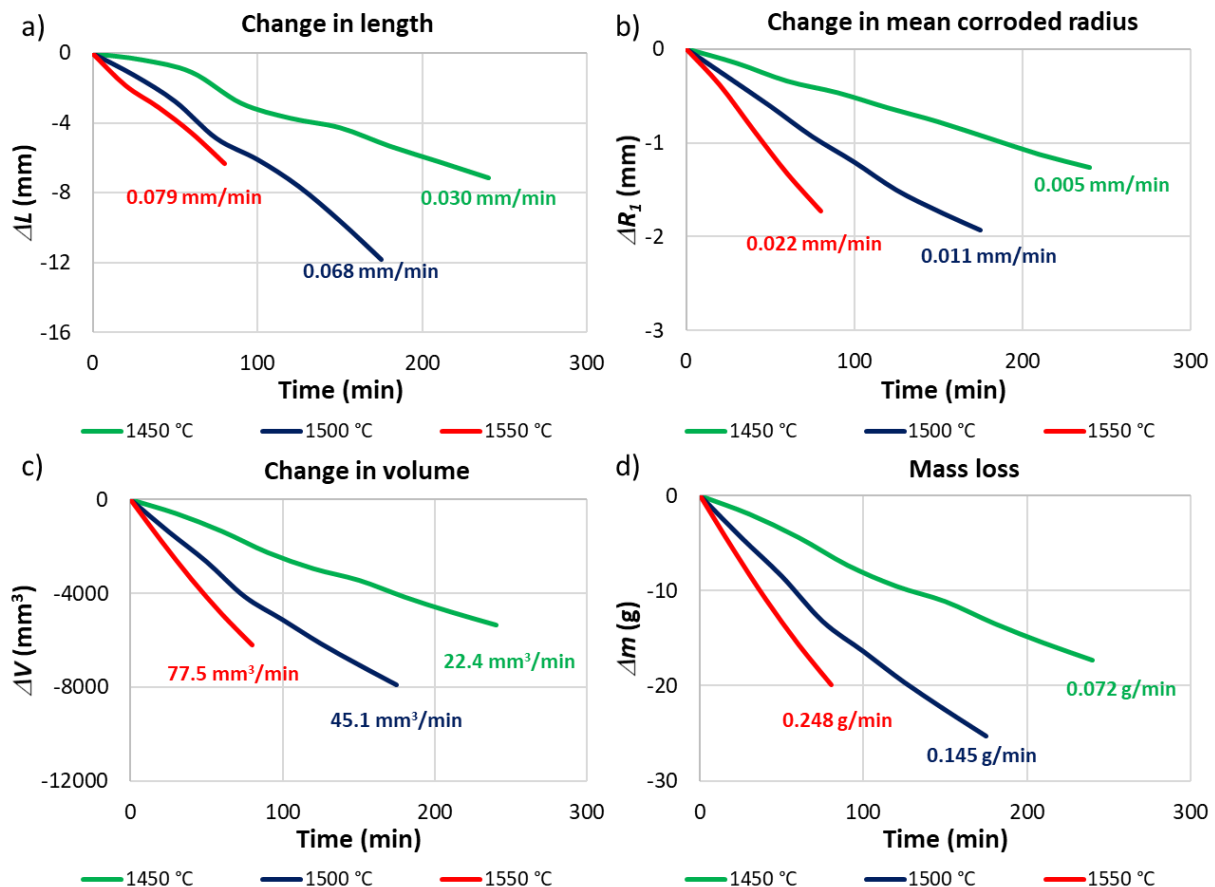


Figure 56: Virgin and corroded samples with inserted CW curves of last steps of magnesia dissolution with 200 rpm in S2 slag.



### 5.4.2. Dissolution parameters

The dissolution parameters were extracted from the CW curves also for magnesia dissolution. Determination methods and applications are similar to alumina dissolution. Only difference is Marangoni groove. As the mass flux due to Marangoni convection is not included in Sherwood relations for diffusivity determination, mean corroded radius, immersion length, and mass flux density were determined excluding the groove. Nevertheless mass flux from the groove was included to calculate bulk concentration of magnesia and slag viscosity as they are dependent on total dissolved amount.



**Figure 57:** a), b), c) and d) change in length, mean corroded radius, volume and mass respectively for magnesia dissolution in S1 slag with 200 rpm at 1450, 1500 and 1550 °C. The numbers inserted give the average rate over the total dissolution time.

The change in the sample length, mean corroded radius, volume, and mass over dissolution time are represented in **Figure 57** a)-d) respectively for magnesia dissolution in S1 slag with 200 rpm at 1450, 1500 and 1550 °C. The diagrams reflect the effect of temperature on the dissolution. All these parameters increased in absolute value with the rising experimental temperature, because of lower slag viscosity and larger solubility limit at higher temperature. The average rates of change in the mean corroded radius, volume, and mass increase 2.0–2.2 and 1.7–2.0 times with an increase in temperature from 1450 °C to 1500 °C and 1500 °C to 1550 °C, respectively. The average rate of change in the sample length increases 2.27 times and 1.16 times with an increase in temperature from 1450 °C to 1500 °C and 1500 °C to 1550

°C, respectively. A slightly decreasing slope or almost linear trend of the dissolution parameters indicates a quasi-steady dissolution [91].

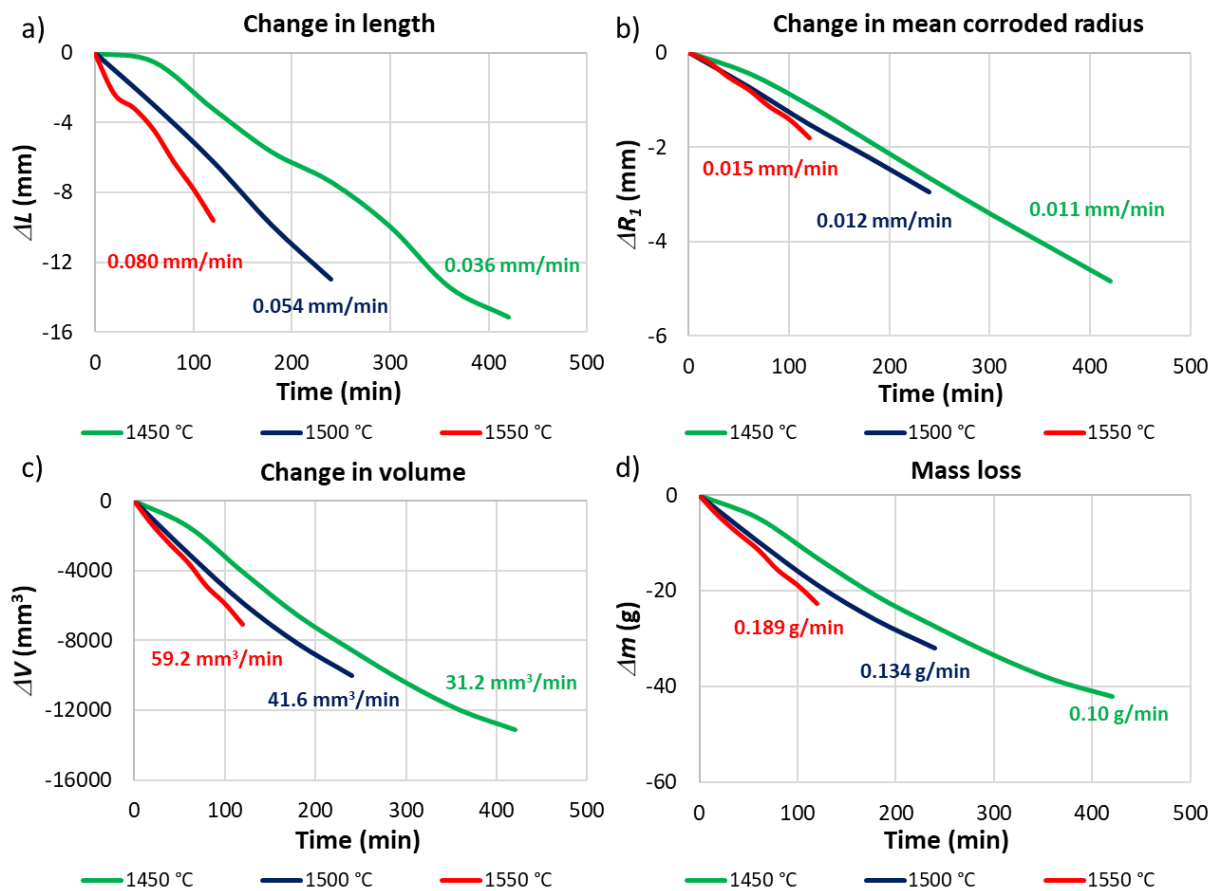


**Figure 58:** a), b), c) and d) change in length, mean corroded radius, volume and mass, respectively, for magnesia dissolution in S2 slag with 200 rpm at 1450, 1500 and 1550 °C. The numbers inserted give the average rate over the total dissolution time.

The change in the sample length, mean corroded radius, volume, and mass over dissolution time are represented in Figure 58 a)-d), respectively, for magnesia dissolution in S2 slag with 200 rpm at 1450, 1500 and 1550 °C. The diagrams reflect the effect of temperature on the dissolution, but the effect is less compared to other slag-refractory combinations examined here. All these parameters increased in absolute value with the rising experimental temperature. The average rates of volume and mass increase 1.33–1.42 times with an increase in temperature from 1450 °C to 1500 °C and 1500 °C to 1550 °C. The average rate of change in the mean corroded radius increases 1.1 times and 1.25 times with an increase in temperature from 1450 °C to 1500 °C and 1500 °C to 1550 °C, respectively. The average rate of change in the sample length increases 1.5 times with an increase in temperature from 1450 °C to 1500 °C and 1500 °C to 1550 °C. A slightly decreasing slope or almost linear trend of the dissolution parameters indicates a quasi-steady dissolution [91]. The average rates of these parameters are higher in S2 than in S1 at 1450 °C but the trend is reverse at 1550 °C and they are quite similar at 1500 °C.

### 5.4.3. Diffusivity

The diffusivities for all the corrosion steps were calculated with equation (45) using the dissolution parameters extracted from the CW curves and the parameters are tabulated in **Table 17** for magnesia dissolution in S1 with 200 rpm at 1450, 1500 and 1550 °C. The mean sample radius, tip radius, immersion length and slag viscosity continuously decrease with the dissolution time. Whereas the bulk concentration of magnesia increases with the dissolution. **Figure 59 a)** represents the diffusivities ( $D_c$  and  $D_{0,c}$ ) of magnesia for all the corrosion steps at three temperatures in S1 slag with 200 rpm. The diffusivity increases with rising temperature. At a particular temperature, the diffusivity increases with dissolution time, probably because of decrease in viscosity with magnesia dissolution. This increase of diffusivity is more pronounced at higher temperature. The Arrhenius plot was produced similar to alumina dissolution (section 5.3.3). **Figure 59 b)** represents the Arrhenius plot which shows the linear tendency, thereby confirming the plausibility of diffusivities. The test intervals used for the Arrhenius plots together with the associated mass loss, bulk concentrations of magnesia and the corresponding activation energies are tabulated in **Table 18**. The activation energy of diffusion decreases with increasing mass loss and bulk concentration except for the very last.

**Table 17: Dissolution parameters used for diffusivity calculation of magnesia in S1 slag at 1450, 1500 and 1550 °C.**

Temperature	Corrosion step, $c$	Mean sample radius, $R_{1,c-1/2}$ (m)	Tip radius, $R_{t,c-1/2}$ (m)	Bulk concentration, $W_{0,c-1/2}$ (wt%/100)	Viscosity, $\eta_{c-1/2}$ (Pas)	Immersion length, $l_{c-1/2}$ (m)	Mass flux density, $j_{c-1/2}$ (kg/m <sup>2</sup> s)
1450 °C	1	0.01008	0.00959	0.07042	1.0032	0.04758	0.000320497
	2	0.00991	0.00858	0.07459	0.9624	0.04716	0.000428470
	3	0.00975	0.00783	0.07952	0.9173	0.04662	0.000533042
	4	0.00961	0.00726	0.08412	0.8775	0.04570	0.000421395
	5	0.00946	0.00679	0.08783	0.8477	0.04433	0.000321630
	6	0.00929	0.00642	0.09158	0.8186	0.04297	0.000487186
	7	0.00912	0.00610	0.09549	0.7907	0.04184	0.000450847
	8	0.00896	0.00590	0.09889	0.7675	0.04075	0.000422825
1500 °C	1	0.01003	0.00950	0.07252	0.7014	0.05022	0.000844155
	2	0.00973	0.00802	0.08059	0.6505	0.04776	0.000878329
	3	0.00942	0.00699	0.08925	0.6023	0.04501	0.001127460
	4	0.00912	0.00625	0.09669	0.5648	0.04347	0.000811192
	5	0.00884	0.00549	0.10269	0.5375	0.04188	0.000902163
	6	0.00857	0.00517	0.10848	0.5130	0.03960	0.000878389
	7	0.00836	0.00518	0.11371	0.4929	0.03710	0.000915946
1550 °C	1	0.00992	0.00944	0.07435	0.5026	0.04845	0.001412109
	2	0.00949	0.00813	0.08548	0.4560	0.04646	0.001476643
	3	0.00902	0.00697	0.09562	0.4194	0.04434	0.001491665
	4	0.00858	0.00599	0.10419	0.3920	0.04237	0.001480528

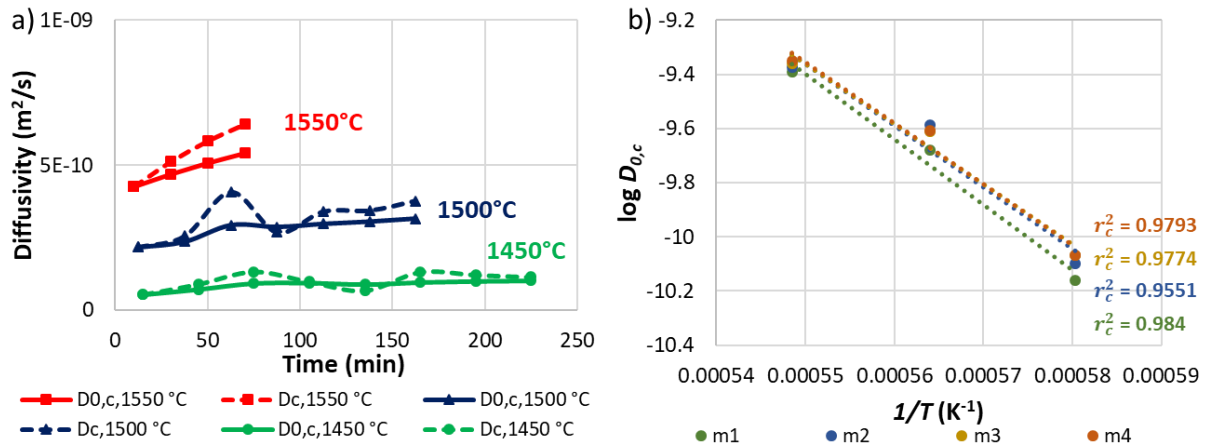


Figure 59: a) Magnesia diffusivity in S1 slag at 1450, 1500 and 1550 °C with 200 rpm b) Arrhenius plot of magnesia diffusivity in S1 slag with 200 rpm.

Table 18: Test intervals as applied for Arrhenius plot with associated mass loss, bulk concentrations of magnesia and corresponding activation energies for magnesia in S1 slag with 200 rpm.

Mass loss (g)	Bulk concentration (wt%/100)	Corresponding corrosion steps, $c_T$	Activation Energy (kJ/mol)
m1	4.8±0.71	2 <sub>1450 °C</sub> ; 1 <sub>1500 °C</sub> ; 1 <sub>1550 °C</sub>	462
m2	11.7±1.31	5 <sub>1450 °C</sub> ; 3 <sub>1500 °C</sub> ; 2 <sub>1550 °C</sub>	437
m3	15.8±0.51	7 <sub>1450 °C</sub> ; 4 <sub>1500 °C</sub> ; 3 <sub>1550 °C</sub>	426
m4	18.9±1.45	8 <sub>1450 °C</sub> ; 5 <sub>1500 °C</sub> ; 4 <sub>1550 °C</sub>	431

The dissolution parameters for magnesia dissolution in S2 with 200 rpm at 1450, 1500 and 1550 °C are tabulated in **Table 19**. Here also, the mean sample radius, tip radius, immersion length and slag viscosity continuously decrease with the dissolution time. Whereas the bulk concentration of magnesia increases with the dissolution. **Figure 60 a)** represents the diffusivities ( $D_c$  and  $D_{0,c}$ ) of magnesia for all the corrosion steps at three experimental temperatures in S2 slag with 200 rpm. In this case also, the diffusivity increases with rising temperature. At a particular temperature, the diffusivity increases with dissolution time, probably because of decrease in viscosity with magnesia dissolution. Arrhenius plot was produced similar to alumina dissolution (5.3.3). **Figure 60 b)** represents the Arrhenius plot of diffusivities of magnesia dissolution in S2 slag with 200 rpm and the plausibility of diffusivities is confirmed by the linear tendency of the Arrhenius plot. The test intervals used for the Arrhenius plots together with the associated mass loss, bulk concentrations of magnesia and the corresponding activation energies are tabulated in **Table 20**. Diffusivities of magnesia are higher for the dissolution in S2 than in S1 at 1450 and 1500 °C, but the trend is opposite at 1550 °C.

**Table 19: Dissolution parameters used for diffusivity calculation of magnesia in S2 slag at 1450, 1500 and 1550 °C.**

Temperature	Corrosion step, $c$	Mean sample radius, $R_{1,c-1/2}$ (m)	Tip radius, $R_{t,c-1/2}$ (m)	Bulk concentration, $W_{0,c-1/2}$ (wt%/100)	Viscosity, $\eta_{c-1/2}$ (Pas)	Immersion length, $l_{c-1/2}$ (m)	Mass flux density, $j_{c-1/2}$ (kg/m <sup>2</sup> s)
1450 °C	1	0.00988	0.00942	0.00482	1.2567	0.04928	0.000395804
	2	0.00934	0.00798	0.01726	1.0909	0.04735	0.000781864
	3	0.00862	0.00670	0.03186	0.9347	0.04463	0.000860989
	4	0.00785	0.00570	0.04436	0.8274	0.04290	0.000810446
	5	0.00709	0.00499	0.05488	0.7515	0.04124	0.000879050
	6	0.00636	0.00461	0.06400	0.6950	0.03863	0.000883468
	7	0.00564	0.00408	0.07084	0.6573	0.03618	0.000745986
1500 °C	1	0.00981	0.00910	0.00963	0.8216	0.04768	0.000840630
	2	0.00906	0.00719	0.02761	0.6835	0.04453	0.000933155
	3	0.00832	0.00597	0.04297	0.5921	0.04099	0.000916475
	4	0.00760	0.00514	0.05551	0.5322	0.03754	0.000883250
1550 °C	1	0.01000	0.00969	0.00462	0.6121	0.04806	0.001105520
	2	0.00974	0.00859	0.01307	0.5614	0.04643	0.000987176
	3	0.00945	0.00742	0.02036	0.5231	0.04540	0.000979316
	4	0.00914	0.00665	0.02810	0.4871	0.04371	0.001356068
	5	0.00883	0.00606	0.03568	0.4551	0.04157	0.001084805
	6	0.00850	0.00546	0.04272	0.4288	0.03950	0.001483303

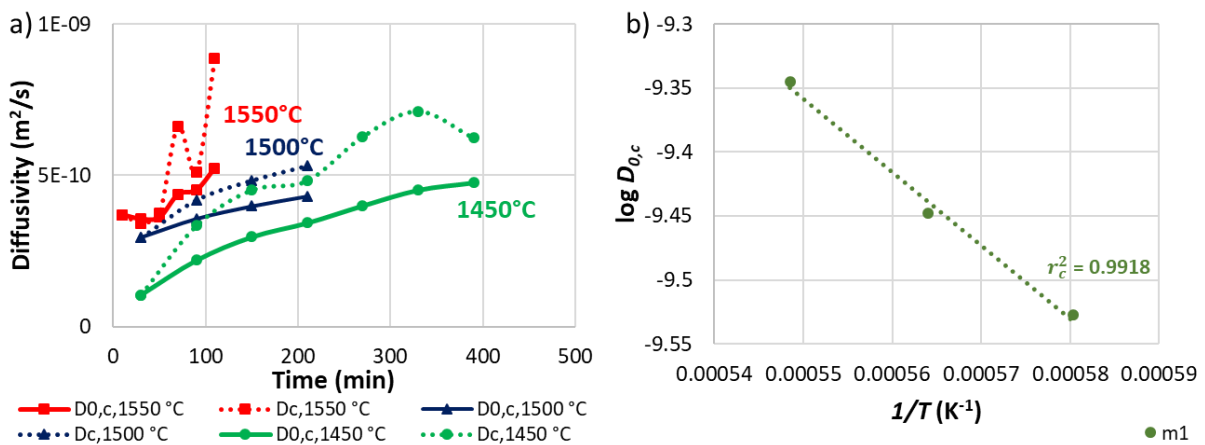


**Figure 60: a) Magnesia diffusivity in S2 slag at 1450, 1500 and 1550 °C with 200 rpm b) Arrhenius plot of magnesia diffusivity in S2 slag with 200 rpm.**

**Table 20: Test intervals as applied for Arrhenius plot with associated mass loss, bulk concentrations of magnesia and corresponding activation energies for magnesia in S2 slag with 200 rpm.**

Mass loss (g)		Bulk concentration (wt%/100)	Corresponding corrosion steps, $c_T$	Activation Energy (kJ/mol)
m1	19.5±1.31	0.032±0.0040	3 <sub>1450 °C</sub> ; 2 <sub>1500 °C</sub> ; 5 <sub>1550 °C</sub>	109

## 5.5. Comparison of diffusivities

In the present study, diffusivities of alumina and magnesia were determined using two experimental setups and several determination methods. Three different models were used to determine diffusivities from CLSM experiments. Sherwood relations were used to calculate diffusivities of each corrosion steps of all dynamic corrosion experiments. In addition to this, a simulation method according to Guarco et al. [28] was applied to determine diffusivities for one step at each temperature in both slags for alumina dissolution and the results have been compared with diffusivities obtained from Sherwood relations and CLSM results. **Table 21** shows the diffusivities of alumina obtained from CLSM and CWTD experiments using different determination methods. As the simulation was conducted for one step at each temperature, steps with similar mass loss relative to initial mass were chosen. Both results of simulations and Sherwood relation show good agreement for alumina diffusivities and these results are also in good agreement with M3 model for CLSM studies. M1 and M2 models of CLSM overestimate the diffusivities in all cases for the alumina dissolution. The better fitting quality of M3 could also be a consequence of one further parameters. The agreement with CWTD where the boundary layer thickness is very well defined gives an additional verification of the suitability of the M3 model.

**Table 21: Diffusivities of alumina obtained from different experimental setups and determination methods.**

Slag	Experimental temperature (°C)	Diffusivities from CWTD		Diffusivity from CLSM		
		Sherwood relations ( $D_c$ ), equation (45)	Simulation ( $D_c$ )	M1	M2	M3
S1	1450	2.80E-11 ( $D_2$ )	2.09E-11 ( $D_2$ )	1.34E-10	8.33E-11	2.71E-11
	1500	4.56E-11 ( $D_3$ )	4.74E-11 ( $D_3$ )	2.26E-10	1.33E-10	4.25E-11
	1550	7.56E-11 ( $D_2$ )	7.31E-11 ( $D_2$ )	4.49E-10	2.49E-10	7.44E-11
S2	1450	2.82E-11 ( $D_6$ )	3.04E-11 ( $D_6$ )	1.64E-10	8.51E-11	3.60E-11
	1500	4.12E-11 ( $D_5$ )	3.88E-11 ( $D_5$ )	1.61E-10	8.84E-11	4.07E-11
	1550	6.59E-11 ( $D_3$ )	4.80E-11 ( $D_3$ )	2.52E-10	1.29E-10	5.07E-11

In this work, diffusivities of magnesia from CWTD experiments were determined only with Sherwood relation, but all three model were applied for CLSM studies. It was observed that, at particular temperature, the diffusivity of magnesia reasonably increased with time in CWTD experiments. Because of this, diffusivities of first corrosion steps have been compared with the CLSM results and tabulated in **Table 22**. Here also, results obtained from M3 model of CLSM studies show better match with the diffusivities from CWTD experiments. The agreement between M3 of CLSM and CWTD results in all cases is not as good as the case of alumina,

maybe because of interference of Marangoni convection in CWTD experiments of magnesia and use of fused magnesia real particles of irregular shape in CLSM experiments.

**Table 22: Diffusivities of magnesia obtained from different experimental setups and determination methods.**

Slag	Experimental temperature (°C)	Diffusivities from CWTD using Sherwood relations ( $D_1$ ), equation (45)	Diffusivity from CLSM		
			M1	M2	M3
S1	1450	5.45E-11	3.93E-10	2.81E-10	1.63E-10
	1500	2.17E-10	6.48E-10	4.61E-10	2.67E-10
	1550	4.27E-10	1.09E-09	7.71E-10	3.67E-10
S2	1450	1.05E-10	1.84E-10	1.47E-10	1.29E-10
	1500	2.94E-10	3.22E-10	2.56E-10	1.81E-10
	1550	3.70E-10	8.46E-10	6.66E-10	2.62E-10

## 6. Conclusion

Dissolution experiments for alumina and magnesia specimens were successfully carried out with CLSM and CWTD at three temperatures. The accuracy of the laser measurement of CWTD supports satisfying results. The CW curves represent the wear of the whole sample surface with high resolution, and as a result, the dissolution parameters calculated from the CW curve are expected to be more accurate than the manual measurements of the post-mortem analysis. In addition to this, another advantage of CWTD is the possibility of several corrosion steps in a single experiment.

Among three models for diffusivity determination from CLSM studies, M3 is more scientifically sound for quasi-steady state dissolution which incorporate the Stefan condition correctly, moving boundary condition and effect of bath movement. It is found that models M1 and M2 suffer from the fact they cannot represent the dissolution curve shape well, as their assumption regarding the effective diffusive boundary layer thickness proofs to be not accurate enough. Fitting quality of measured and model radius of M3 is far better than other two in all experiments. The diffusivity results from CWTD also show good agreement with results of M3 from CLSM, which further validates the model.

In CLSM studies, time for total dissolution rises with decreasing temperature in all cases. Dissolution time of alumina in S3 at 1450 °C is highest among all slags, whereas for magnesia dissolution, it is highest in S4 at 1450 °C. There is no clear correlation between dissolution rate and slag basicity for alumina dissolution, but dissolution rate of magnesia decreases with rising basicity. Dissolution rates of alumina and magnesia are highest in S4 and S1, respectively.

In CWTD studies, there was no Marangoni groove at the triple points (refractory/slag/atmosphere) in case of alumina dissolution with 200 rpm. Reynolds numbers were sufficiently high for the dynamic experiments with 200 rpm to suppress the Marangoni convection. But groove was observed with lower rotational speed. Contrary to the case of alumina 200 rpm was not sufficiently high to suppress the Marangoni convection during magnesia dissolution. Average rates of change of relevant dissolution parameters length, radius, volume and mass for alumina at a particular temperature are higher in S1. In case of

magnesia dissolution, the average rates of these parameters are higher in S2 than in S1 at 1450 °C but the trend is reverse at 1550 °C and they are quite similar at 1500 °C. A slightly decreasing slope or almost linear trend of the dissolution parameters indicates a quasi-steady dissolution [91]. The diffusivities for all the steps of dynamic corrosion experiments were calculated with Sherwood relations using the dissolution parameters extracted from the CW curves. A Simulation method which considers the actual sample shape and flow field around it was also applied to determine diffusivity of alumina for one corrosion step at each experimental temperature. Results obtained from both methods show good agreement. The linear tendency of Arrhenius plot confirms the plausibility of diffusivities.



## 7. References

- [1] H. Harmuth and S. Vollmann, "Refractory Corrosion by Dissolution in Slags - Challenges and Trends of Present Fundamental Research," *Iron Steel Rev.*, vol. 58, no. 4, pp. 157–170, 2014.
- [2] V. Kircher, "Kristallisationsverhaltens oxidisch-silikatischer Systeme mittels HT-LSCM," Montan University Leoben, 2017.
- [3] H. Harmuth, *Continuous refractory wear*. Montanuniversitaet, Leoben.
- [4] H. Harmuth and Burhanuddin, "Evaluation of CLSM measurements for dissolution studies – a case study investigating alumina dissolution in a silicate slag," *Ceram. Int.*, vol. Submitted, 2022.
- [5] D. W. Readey and A. R. Copper, "Molecular diffusion with a moving boundary and spherical symmetry," *Chem. Eng. Sci.*, vol. 21, no. 10, pp. 917–922, Oct. 1966, doi: 10.1016/0009-2509(66)85085-6.
- [6] J. Liu, M. Guo, P. T. Jones, F. Verhaeghe, B. Blanpain, and P. Wollants, "In situ observation of the direct and indirect dissolution of MgO particles in CaO-Al<sub>2</sub>O<sub>3</sub>-SiO<sub>2</sub>-based slags," *J. Eur. Ceram. Soc.*, vol. 27, no. 4, pp. 1961–1972, 2007, doi: 10.1016/j.jeurceramsoc.2006.05.107.
- [7] B. J. Monaghan, S. A. Nightingale, L. Chen, and G. A. Brooks, "The dissolution behaviour of selected oxides in CaO-SiO<sub>2</sub>-Al<sub>2</sub>O<sub>3</sub> slags," *Int. Conf. Molten Slags Fluxes Salts*, pp. 585–594, 2004.
- [8] B. J. Monaghan, L. Chen, and J. Sorbe, "Comparative study of oxide inclusion dissolution in CaO-SiO<sub>2</sub>-Al<sub>2</sub>O<sub>3</sub> slag," *Ironmak. Steelmak.*, vol. 32, no. 3, pp. 258–264, Jun. 2005, doi: 10.1179/174328105X28793.
- [9] B. J. Monaghan and L. Chen, "Dissolution behavior of alumina micro-particles in CaO-SiO<sub>2</sub>-Al<sub>2</sub>O<sub>3</sub> liquid oxide," *J. Non. Cryst. Solids*, vol. 347, no. 1–3, pp. 254–261, Nov. 2004, doi: 10.1016/j.jnoncrysol.2004.09.011.
- [10] S. Sridhar and A. W. Cramb, "Kinetics of Al<sub>2</sub>O<sub>3</sub> dissolution in CaO-MgO-SiO<sub>2</sub>-Al<sub>2</sub>O<sub>3</sub> slags: In Situ observations and analysis," *Metall. Mater. Trans. B*, vol. 31B, no. 2, pp. 406–410, Apr. 2000, doi: 10.1007/s11663-000-0059-2.
- [11] M. Valdez, K. Prapakorn, A. W. Cramb, and S. Sridhar, "Dissolution of alumina particles in CaO-Al<sub>2</sub>O<sub>3</sub>-SiO<sub>2</sub>-MgO slags," *Ironmak. Steelmak.*, vol. 29, no. 1, pp. 47–52, 2002, doi: 10.1179/030192302225001965.
- [12] M. Valdez, K. Prapakorn, A. W. Cramb, and S. Seetharaman, "A study of the dissolution of Al<sub>2</sub>O<sub>3</sub>, MgO and MgAl<sub>2</sub>O<sub>4</sub> particles in a CaO-Al<sub>2</sub>O<sub>3</sub>-SiO<sub>2</sub> slag," *Steel Res.*, vol. 72, no. 8, pp. 291–297, 2001, doi: 10.1002/srin.200100120.
- [13] J. Liu, F. Verhaeghe, M. Guo, B. Blanpain, and P. Wollants, "In situ observation of the dissolution of spherical alumina particles in CaO-Al<sub>2</sub>O<sub>3</sub>-SiO<sub>2</sub> melts," *J. Am. Ceram. Soc.*, vol. 90, no. 12, pp. 3818–3824, 2007, doi: 10.1111/j.1551-2916.2007.02062.x.
- [14] J. Liu, L. Zhu, M. Guo, F. Verhaeghe, B. Blanpain, and P. Wollants, "In-situ observation of the dissolution of ZrO<sub>2</sub> oxide particles in mould fluxes," *Rev. Métallurgie*, vol. 105, no. 5, pp. 255–262, May 2008, doi: 10.1051/metal:2008039.
- [15] F. Verhaeghe, J. Liu, M. Guo, S. Arnout, B. Blanpain, and P. Wollants, "Determination of the dissolution mechanism of Al<sub>2</sub>O<sub>3</sub> in CaO-Al<sub>2</sub>O<sub>3</sub>-SiO<sub>2</sub> liquids using a combined

- experimental-numerical approach," *J. Appl. Phys.*, vol. 103, no. 2, pp. 023506-1–8, 2008, doi: 10.1063/1.2830852.
- [16] F. Verhaeghe, J. Liu, M. Guo, S. Arnout, B. Blanpain, and P. Wollants, "Dissolution and diffusion behavior of Al<sub>2</sub>O<sub>3</sub> in a CaO–Al<sub>2</sub>O<sub>3</sub>–SiO<sub>2</sub> liquid: An experimental-numerical approach," *Appl. Phys. Lett.*, vol. 91, no. 12, pp. 124104-1–3, Sep. 2007, doi: 10.1063/1.2786854.
- [17] K. W. Yi, C. Tse, J. H. Park, M. Valdez, A. W. Cramb, and S. Sridhar, "Determination of dissolution time of Al<sub>2</sub>O<sub>3</sub> and MgO inclusions in synthetic Al<sub>2</sub>O<sub>3</sub>–CaO–MgO slags," *Scand. J. Metall.*, vol. 32, no. 4, pp. 177–184, 2003, doi: 10.1034/j.1600-0692.2003.20631.x.
- [18] M. J. Whelan, "On the kinetics of precipitate dissolution," *Met. Sci. J.*, vol. 3, no. 1, pp. 95–97, Jan. 1969, doi: 10.1179/msc.1969.3.1.95.
- [19] S. Feichtinger, S. K. Michelic, Y. B. Kang, and C. Bernhard, "In situ observation of the dissolution of SiO<sub>2</sub> particles in CaO–Al<sub>2</sub>O<sub>3</sub>–SiO<sub>2</sub> slags and mathematical analysis of its dissolution pattern," *J. Am. Ceram. Soc.*, vol. 97, no. 1, pp. 316–325, 2014, doi: 10.1111/jace.12665.
- [20] N. Froessling, "Ueber die Verdunstung fallender Tropfen," *Gerlands Beitrage zur Geophys.*, vol. 52, pp. 170–215, 1938.
- [21] W. G. Cochran, "The flow due to a rotating disc," *Math. Proc. Cambridge Philos. Soc.*, vol. 30, no. 3, pp. 365–375, Jul. 1934, doi: 10.1017/S0305004100012561.
- [22] V. G. Levich, *Physicochemical hydrodynamics*. Englewood Cliffs, N. J., Prentice-Hall, 1962.
- [23] A. R. Cooper and W. D. Kingery, "Dissolution in ceramic systems: I, Molecular diffusion, natural convection, and forced convection studies of sapphire dissolution in calcium aluminum silicate," *J. Am. Ceram. Soc.*, vol. 47, no. 1, pp. 37–43, Jan. 1964, doi: 10.1111/j.1151-2916.1964.tb14638.x.
- [24] M. Kosaka and S. Minowa, "Mass-transfer from solid metal cylinder into liquid metal," *Tetsu-to-Hagane*, vol. 52, no. 12, pp. 1748–1762, 1966, doi: 10.2355/tetsutohagane1955.52.12\_1748.
- [25] S. Amini, M. Brungs, S. Jahanshahi, and O. Ostrovski, "Effects of additives and temperature on the dissolution rate and diffusivity of lime in Al<sub>2</sub>O<sub>3</sub>–CaO–SiO<sub>2</sub> based slags," *Metall. Mater. Trans. B*, vol. 37B, pp. 773–780, 2006.
- [26] M. Eisenberg, C. W. Tobias, and C. R. Wilke, "Ionic Mass Transfer and Concentration Polarization at Rotating Electrodes," *J. Electrochem. Soc.*, vol. 101, no. 6, p. 306, 1954, doi: 10.1149/1.2781252.
- [27] F. Tachibana and S. Fukui, "Convective heat transfer of the rotational and axial flow between two concentric cylinders," *Bull. JSME*, vol. 7, no. 26, pp. 385–391, 1964, doi: 10.1299/jsme1958.7.385.
- [28] J. Guarco, Burhanuddin, S. Vollmann, and H. Harmuth, "Method for determination of effective binary diffusivities in dissolution of dense ceramic materials," *Ceram. Int.*, no. September, 2021, doi: 10.1016/j.ceramint.2021.11.264.
- [29] W. E. Lee and S. Zhang, "Melt corrosion of oxide and oxide–carbon refractories," *Int. Mater. Rev.*, vol. 44, no. 3, pp. 77–104, Mar. 1999, doi: 10.1179/095066099101528234.

- [30] J. Goriupp, A. Rief, and J. Schenk, "Quantifying of a dynamic refractory wear test setup for MgO-C products," *BHM Berg- und Hüttenmännische Monatshefte*, vol. 157, no. 8–9, pp. 340–344, Sep. 2012, doi: 10.1007/s00501-012-0028-5.
- [31] C. Reynaert, E. Śniezek, and J. Szczerba, "Corrosion tests for refractory materials intended for the steel industry - A review," *Ceram. - Silikaty*, vol. 64, no. 3, pp. 278–288, 2020, doi: 10.13168/cs.2020.0017.
- [32] E. Y. Sako, M. A. L. Braulio, and V. C. Pandolfelli, "The corrosion resistance of microsilica-containing  $\text{Al}_2\text{O}_3$ -MgO and  $\text{Al}_2\text{O}_3$ -spinel castables," *Ceram. Int.*, vol. 38, no. 6, pp. 4783–4789, Aug. 2012, doi: 10.1016/j.ceramint.2012.02.066.
- [33] B. Ma *et al.*, "Slag corrosion and penetration behaviors of  $\text{MgAl}_2\text{O}_4$  and  $\text{Al}_2\text{O}_3$  based refractories," *Refract. Ind. Ceram.*, vol. 56, no. 5, pp. 494–501, Jan. 2016, doi: 10.1007/s11148-016-9876-y.
- [34] A. G. Tomba Martinez, A. P. Luz, M. A. L. Braulio, and V. C. Pandolfelli, " $\text{Al}_2\text{O}_3$ -based binders for corrosion resistance optimization of  $\text{Al}_2\text{O}_3$ - $\text{MgAl}_2\text{O}_4$  and  $\text{Al}_2\text{O}_3$ -MgO refractory castables," *Ceram. Int.*, vol. 41, no. 8, pp. 9947–9956, 2015, doi: 10.1016/j.ceramint.2015.04.074.
- [35] V. Muñoz, S. Camelli, and A. G. Tomba Martinez, "Slag corrosion of alumina-magnesia-carbon refractory bricks: Experimental data and thermodynamic simulation," *Ceram. Int.*, vol. 43, no. 5, pp. 4562–4569, 2017, doi: 10.1016/j.ceramint.2016.12.114.
- [36] J. H. Park, M. O. Suk, I.-H. Jung, M. Guo, and B. Blanpain, "Interfacial reaction between refractory materials and metallurgical slags containing fluoride," *steel Res. Int.*, vol. 81, no. 10, pp. 860–868, Oct. 2010, doi: 10.1002/srin.201000157.
- [37] M. K. Cho, M. A. Van Ende, T. H. Eun, and I. H. Jung, "Investigation of slag-refractory interactions for the Ruhrstahl Heraeus (RH) vacuum degassing process in steelmaking," *J. Eur. Ceram. Soc.*, vol. 32, no. 8, pp. 1503–1517, 2012, doi: 10.1016/j.jeurceramsoc.2012.01.005.
- [38] M.-A. Van Ende, M. Guo, P. T. Jones, B. Blanpain, and P. Wollants, "Degradation of MgO-C refractories by MnO-rich stainless steel slags," *Ceram. Int.*, vol. 35, no. 6, pp. 2203–2212, Aug. 2009, doi: 10.1016/j.ceramint.2008.12.007.
- [39] S. Vollmann and H. Harmuth, "Marangoni convection as a contribution to refractory corrosion - CFD simulation and analytical approaches," in *UNITECR 2013*, 2013, no. 1, pp. 781–786.
- [40] Y. Chen, G. Brooks, S. Nightingale, K. Coley, and M. Hamed, "Marangoni effect in refractory slag line dissolution," in *Advances in refractories for the metallurgical industries IV*, 2004, pp. 513–526.
- [41] Z. Wang, T. Maotsela, P. M. Toperesu, G. M. Kale, J. Daji, and D. Parkinson, "Dynamic and static corrosion of alpha-alumina bonded refractory in contact with molten soda-lime-silica (SLS) glass," *Ceram. Int.*, vol. 45, no. 1, pp. 725–732, Jan. 2019, doi: 10.1016/j.ceramint.2018.09.235.
- [42] C. Baudín, E. Criado, J. J. Bakali, and P. Pena, "Dynamic corrosion of  $\text{Al}_2\text{O}_3$ - $\text{ZrO}_2$ - $\text{SiO}_2$  and  $\text{Cr}_2\text{O}_3$ -containing refractories by molten frits. Part I: Macroscopic analysis," *J. Eur. Ceram. Soc.*, vol. 31, no. 5, pp. 697–703, May 2011, doi: 10.1016/j.jeurceramsoc.2010.11.023.
- [43] Y. Liang, A. Huang, X. Zhu, H. Gu, and L. Fu, "Dynamic slag/refractory interaction of lightweight  $\text{Al}_2\text{O}_3$ -MgO castable for refining ladle," *Ceram. Int.*, vol. 41, no. 6, pp.

- 8149–8154, Jul. 2015, doi: 10.1016/j.ceramint.2015.03.026.
- [44] J. Park, I. Jung, and H. Lee, "Dissolution behavior of  $\text{Al}_2\text{O}_3$  and MgO inclusions in the CaO– $\text{Al}_2\text{O}_3$ – $\text{SiO}_2$  slags: Formation of ring-like structure of  $\text{MgAl}_2\text{O}_4$  and  $\text{Ca}_2\text{SiO}_4$  around MgO inclusions," *ISIJ Int.*, vol. 46, no. 11, pp. 1626–1634, 2006, doi: 10.2355/isijinternational.46.1626.
- [45] P. Korgul, D. R. Wilson, and W. E. Lee, "Microstructural Analysis of Corroded Alumina-Spinel Castable Refractories," *J. Eur. Ceram. Soc.*, vol. 17, no. 1, pp. 77–84, 1997, doi: 10.1016/S0955-2219(96)00073-8.
- [46] S. Zhang and W. E. Lee, "Influence of additives on corrosion resistance and corroded microstructures of MgO-C refractories," *J. Eur. Ceram. Soc.*, vol. 21, no. 13, pp. 2393–2405, 2001, doi: 10.1016/S0955-2219(01)00208-4.
- [47] M. Bavand-Vandchali, F. Golestani-Fard, H. Sarpoolaky, H. R. Rezaie, and C. G. Aneziris, "The influence of in situ spinel formation on microstructure and phase evolution of MgO-C refractories," *J. Eur. Ceram. Soc.*, vol. 28, no. 3, pp. 563–569, 2008, doi: 10.1016/j.jeurceramsoc.2007.07.009.
- [48] O. R. Mattione A., Smith J., "Review of slag line corrosion testing methods," 2016.
- [49] M. Guo *et al.*, "Degradation mechanisms of magnesia-carbon refractories by high-alumina stainless steel slags under vacuum," *Ceram. Int.*, vol. 33, no. 6, pp. 1007–1018, Aug. 2007, doi: 10.1016/j.ceramint.2006.03.009.
- [50] H. Um, K. Lee, K.-Y. Kim, G. Shin, and Y. Chung, "Effect of carbon content of ferromanganese alloy on corrosion behaviour of MgO–C refractory," *Ironmak. Steelmak.*, vol. 41, no. 1, pp. 31–37, Jan. 2014, doi: 10.1179/1743281212Y.0000000098.
- [51] A. H. Bui, S. C. Park, I. S. Chung, and H. G. Lee, "Dissolution behavior of zirconia-refractories during continuous casting of steel," *Met. Mater. Int.*, vol. 12, no. 5, pp. 435–440, 2006, doi: 10.1007/BF03027711.
- [52] H. Um, K. Lee, J. Choi, and Y. Chung, "Corrosion behavior of MgO–C refractory in ferromanganese slags," *ISIJ Int.*, vol. 52, no. 1, pp. 62–67, 2012, doi: 10.2355/isijinternational.52.62.
- [53] S. Jansson, V. Brabie, and L. Bohlin, "Corrosion mechanism and kinetic behaviour of refractory materials in contact with CaO– $\text{Al}_2\text{O}_3$ –MgO– $\text{SiO}_2$  slags," in *VII Int. Conf. on Molten Slags Fluxes and Salts*, 2004, pp. 341–348.
- [54] J. Jeon, Y. Kang, J. H. Park, and Y. Chung, "Corrosion-erosion behavior of  $\text{MgAl}_2\text{O}_4$  spinel refractory in contact with high MnO slag," *Ceram. Int.*, vol. 43, no. 17, pp. 15074–15079, Dec. 2017, doi: 10.1016/j.ceramint.2017.08.034.
- [55] H. Zuo, C. Wang, and Y. Liu, "Dissolution behavior of a novel  $\text{Al}_2\text{O}_3$ –SiC– $\text{SiO}_2$ –C composite refractory in blast furnace slag," *Ceram. Int.*, vol. 43, no. 9, pp. 7080–7087, Jun. 2017, doi: 10.1016/j.ceramint.2017.02.138.
- [56] K. Jiao, X. Fan, J. Zhang, K. Wang, and Y. Zhao, "Corrosion behavior of alumina-carbon composite brick in typical blast furnace slag and iron," *Ceram. Int.*, vol. 44, no. 16, pp. 19981–19988, Nov. 2018, doi: 10.1016/j.ceramint.2018.07.265.
- [57] T. Hirata, T. Morimoto, S. Ohta, and N. Uchida, "Improvement of the corrosion resistance of alumina-chromia ceramic materials in molten slag," *J. Eur. Ceram. Soc.*, vol. 23, no. 12, pp. 2089–2096, 2003, doi: 10.1016/S0955-2219(03)00023-2.

- [58] X. Yu, R. J. Pomfret, and K. S. Coley, "Dissolution of alumina in mold fluxes," *Metall. Mater. Trans. B*, vol. 28, no. 2, pp. 275–279, Apr. 1997, doi: 10.1007/s11663-997-0094-3.
- [59] S. A. Nightingale, B. J. Monaghan, and G. A. Brooks, "Degradation of MgO refractory in CaO-SiO<sub>2</sub>-MgO-FeO<sub>x</sub> and CaO-SiO<sub>2</sub>-Al<sub>2</sub>O<sub>3</sub>-MgO-FeO<sub>x</sub> slags under forced convection," *Metall. Mater. Trans. B*, vol. 36, no. 4, pp. 453–461, Aug. 2005, doi: 10.1007/s11663-005-0036-x.
- [60] C. . Aneziris, E. . Pfaff, and H. . Maier, "Corrosion mechanisms of low porosity ZrO<sub>2</sub> based materials during near net shape steel casting," *J. Eur. Ceram. Soc.*, vol. 20, no. 2, pp. 159–168, Feb. 2000, doi: 10.1016/S0955-2219(99)00149-1.
- [61] H. Wang, R. Caballero, and D. Sichen, "Dissolution of MgO based refractories in CaO-Al<sub>2</sub>O<sub>3</sub>-MgO-SiO<sub>2</sub> slag," *J. Eur. Ceram. Soc.*, vol. 38, no. 2, pp. 789–797, 2018, doi: 10.1016/j.jeurceramsoc.2017.09.030.
- [62] T. Deng, B. Glaser, and D. Sichen, "Experimental design for the mechanism study of lime dissolution in liquid slag," *Steel Res. Int.*, vol. 83, no. 3, pp. 259–268, 2012, doi: 10.1002/srin.201100258.
- [63] C. Bernhard, S. Schider, A. Sormann, G. Xia, and S. Ilie, "Erste ergebnisse des neuen hochtemperatur-konfokalmikroskops am Lehrstuhl für Metallurgie," *BHM Berg- und Hüttenmännische Monatshefte*, vol. 156, no. 5, pp. 161–167, May 2011, doi: 10.1007/s00501-011-0645-4.
- [64] S. Michelic, J. Goriupp, S. Feichtinger, Y.-B. Kang, C. Bernhard, and J. Schenk, "Study on Oxide Inclusion Dissolution in Secondary Steelmaking Slags using High Temperature Confocal Scanning Laser Microscopy," *Steel Res. Int.*, vol. 87, no. 1, pp. 57–67, Jan. 2016, doi: 10.1002/srin.201500102.
- [65] O. Loebich, "The optical properties of gold," *Gold Bull.*, vol. 5, no. 1, pp. 2–10, Mar. 1972, doi: 10.1007/BF03215148.
- [66] F. van de Velde, F. Weinbreck, M. W. Edelman, E. van der Linden, and R. H. Tromp, "Visualisation of biopolymer mixtures using confocal scanning laser microscopy (CSLM) and covalent labelling techniques," *Colloids Surfaces B Biointerfaces*, vol. 31, no. 1–4, pp. 159–168, Sep. 2003, doi: 10.1016/S0927-7765(03)00135-8.
- [67] P. T. Jones *et al.*, "Using confocal scanning laser microscopy for the in situ study of high-temperature behaviour of complex ceramic materials," *J. Eur. Ceram. Soc.*, vol. 27, no. 12, pp. 3497–3507, 2007, doi: 10.1016/j.jeurceramsoc.2007.01.022.
- [68] H. Chikama, H. Shibata, T. Emi, and M. Suzuki, "In-situ real time observation of planar to cellular and cellular to dendritic transition of crystals growing in Fe–C alloy melts," *Mater. Trans. JIM*, vol. 37, no. 4, pp. 620–626, 1996, doi: 10.2320/matertrans1989.37.620.
- [69] H. Yin, T. Emi, and H. Shibata, "Determination of free energy of δ-ferrite/γ-austenite interphase boundary of low carbon steels by in-situ observation," *ISIJ Int.*, vol. 38, no. 8, pp. 794–801, 1998, doi: 10.2355/isijinternational.38.794.
- [70] R. Hans Tromp, F. van de Velde, J. van Riel, and M. Paques, "Confocal scanning light microscopy (CSLM) on mixtures of gelatine and polysaccharides," *Food Res. Int.*, vol. 34, no. 10, pp. 931–938, Jan. 2001, doi: 10.1016/S0963-9969(01)00117-X.
- [71] J. C. G. Blonk, J. van Eendenburg, M. M. G. Koning, P. C. M. Weisenborn, and C. Winkel, "A new CSLM-based method for determination of the phase behaviour of

- aqueous mixtures of biopolymers," *Carbohydr. Polym.*, vol. 28, no. 4, pp. 287–295, Dec. 1995, doi: 10.1016/0144-8617(95)00151-4.
- [72] S. Sridhar, "Application of confocal scanning laser microscopy to steel research," in *3rd International Conference on the Science and Technology of Steelmaking*, 2005, pp. 797–810.
- [73] H. Shibata, Y. Arai, M. Suzuki, and T. Emi, "Kinetics of peritectic reaction and transformation in Fe-C alloys," *Metall. Mater. Trans. B*, vol. 31B, no. 5, pp. 981–991, Oct. 2000, doi: 10.1007/s11663-000-0074-3.
- [74] H. Shibata, H. Yin, S. Yoshinaga, T. Emi, and M. Suzuki, "In-situ observation of engulfment and pushing of nonmetallic inclusions in steel melt by advancing melt/solid interface.," *ISIJ Int.*, vol. 38, no. 2, pp. 149–156, 1998, doi: 10.2355/isijinternational.38.149.
- [75] N. Fuchs, C. Bernhard, S. Michelic, and R. Dippenaar, "HT-LSCM as a tool for indirect determination of precipitates by real-time grain growth observations," in *149th Annual Meeting and Exhibition Supplemental Proceedings*, 2020, pp. 47–55.
- [76] N. Fuchs and C. Bernhard, "Potential and limitations of direct austenite grain growth measurement by means of HT-LSCM," *Mater. Today Commun.*, vol. 28, no. January, p. 102468, Sep. 2021, doi: 10.1016/j.mtcomm.2021.102468.
- [77] M. Bernhard, P. Presoly, N. Fuchs, C. Bernhard, and Y.-B. Kang, "Experimental study of high temperature phase equilibria in the iron-rich part of the Fe-P and Fe-C-P systems," *Metall. Mater. Trans. A*, vol. 51, no. 10, pp. 5351–5364, Oct. 2020, doi: 10.1007/s11661-020-05912-z.
- [78] N. Fuchs and C. Bernhard, "In-situ-untersuchung von austenitkornwachstumsprozessen in stählen mittels hochtemperatur-laser-scanning-konfokal-mikroskop," *BHM Berg- und Hüttenmännische Monatshefte*, vol. 164, no. 5, pp. 200–204, May 2019, doi: 10.1007/s00501-019-0850-0.
- [79] I. Sohn and R. Dippenaar, "In-situ observation of crystallization and growth in high-temperature melts using the confocal laser microscope," *Metall. Mater. Trans. B*, vol. 47, no. 4, pp. 2083–2094, Aug. 2016, doi: 10.1007/s11663-016-0675-0.
- [80] K. Prapakorn, S. Seetharaman, and A. W. Cramb, "A comparison of different techniques for determining the crystallization temperature of slags," in *Steelmaking Conference Proceedings*, 2001, pp. 357–368.
- [81] H. G. Ryu, Z. T. Zhang, J. W. Cho, G. H. Wen, and S. Sridhar, "Crystallization behaviors of slags through a heat flux simulator," *ISIJ Int.*, vol. 50, no. 8, pp. 1142–1150, 2010, doi: 10.2355/isijinternational.50.1142.
- [82] Z. Zhang, G. Wen, and Y. Zhang, "Crystallization behavior of F-free mold fluxes," *Int. J. Miner. Metall. Mater.*, vol. 18, no. 2, pp. 150–158, Apr. 2011, doi: 10.1007/s12613-011-0415-z.
- [83] A. B. Fox, M. E. Valdez, J. Gisby, R. C. Atwood, P. D. Lee, and S. Sridhar, "Dissolution of  $ZrO_2$ ,  $Al_2O_3$ ,  $MgO$  and  $MgAl_2O_4$  particles in a  $B_2O_3$  containing commercial fluoride-free mould slag," *ISIJ Int.*, vol. 44, no. 5, pp. 836–845, 2004, doi: 10.2355/isijinternational.44.836.
- [84] J. H. Park, J. G. Park, D. J. Min, Y. E. Lee, and Y.-B. Kang, "In situ observation of the dissolution phenomena of SiC particle in CaO–SiO<sub>2</sub>–MnO slag," *J. Eur. Ceram. Soc.*, vol. 30, no. 15, pp. 3181–3186, Nov. 2010, doi: 10.1016/j.jeurceramsoc.2010.07.020.

- [85] V. Kircher, Burhanuddin, and H. Harmuth, "Design, operation and evaluation of an improved refractory wear testing technique," *Meas. J. Int. Meas. Confed.*, vol. 178, no. April, p. 109429, 2021, doi: 10.1016/j.measurement.2021.109429.
- [86] N.-A. GmbH, "Betriebsanleitung Continuous Wear Testing Device (CWTD)." Zeltweg, Austria, pp. 1–58, 2019.
- [87] M.-E. M. G. & C. KG, "Data sheet scanCONTROL 29x0,." [https://www.micro-epsilon.co.uk/2D\\_3D/laser-scanner/scanCONTROL-2900/](https://www.micro-epsilon.co.uk/2D_3D/laser-scanner/scanCONTROL-2900/).
- [88] Z. F. Yuan, W. L. Huang, and K. Mukai, "Local corrosion of magnesia-chrome refractories driven by Marangoni convection at the slag-metal interface," *J. Colloid Interface Sci.*, vol. 253, no. 1, pp. 211–216, 2002, doi: 10.1006/jcis.2002.8504.
- [89] H. Wang, J. F. White, and D. Sichen, "A new experimental design to study the kinetics of solid dissolution into liquids at elevated temperature," *Metall. Mater. Trans. B*, vol. 49B, no. 2, pp. 688–698, Apr. 2018, doi: 10.1007/s11663-018-1196-9.
- [90] R. B. M. Dunkl, "Corrosion of refractory material under the action of forced convection flow by means of the rotating cylinder face area at 1500°C," *Glas. Berichte*, vol. 60, no. 8, pp. 261–267, 1987.
- [91] Burhanuddin, J. Guarco, H. Harmuth, and S. Vollmann, "Application of an improved testing device for the study of alumina dissolution in silicate slag," *J. Eur. Ceram. Soc.*, vol. 42, pp. 3652–3659, 2022, doi: 10.1016/j.jeurceramsoc.2022.02.056.
- [92] A. H. Bui, H. M. Ha, I. S. Chung, and H. G. Lee, "Dissolution kinetics of alumina into mold fluxes for continuous steel casting," *ISIJ Int.*, vol. 45, no. 12, pp. 1856–1863, 2005, doi: 10.2355/isijinternational.45.1856.
- [93] W. A. Calvo, P. Pena, and A. G. Tomba Martinez, "Post-mortem analysis of alumina-magnesia-carbon refractory bricks used in steelmaking ladles," *Ceram. Int.*, vol. 45, no. 1, pp. 185–196, Jan. 2019, doi: 10.1016/j.ceramint.2018.09.150.
- [94] G. I. Taylor, "VIII. Stability of a viscous liquid contained between two rotating cylinders," *Philos. Trans. R. Soc. London. Ser. A, Contain. Pap. a Math. or Phys. Character*, vol. 223, no. 605–615, pp. 289–343, Jan. 1923, doi: 10.1098/rsta.1923.0008.
- [95] J. Xin, L. Gan, L. Jiao, and C. Lai, "Accurate density calculation for molten slags in SiO<sub>2</sub>-Al<sub>2</sub>O<sub>3</sub>-CaO-MgO systems," *ISIJ Int.*, vol. 57, no. 8, pp. 1340–1349, 2017, doi: 10.2355/isijinternational.ISIJINT-2017-070.